# ABSTRACT


Title of dissertation: MICROSYSTEMS INTEGRATION TOWARDS POINT-OF-CARE MONITORING OF CLOZAPINE TREATMENT FOR ADHERENCE, EFFICACY, AND SAFETY

Thomas E. Winkler,
Doctor of Philosophy, 2017

Dissertation directed by: Professor Reza Ghodssi,
Institute for Systems Research



Schizophrenia is a challenging and complex disorder with 30–50% of patients not responding to first line antipsychotic treatment. Clozapine is the only antipsychotic approved by the FDA for treatment-resistant schizophrenia and is the most effective antipsychotic medication currently available. Yet, clozapine remains underutilized because of the requirements for frequent invasive and burdensome monitoring to 1) titrate doses to achieve effective blood levels, as well as 2) monitor white blood cells on a weekly basis for the first six months due to risk of agranulocytosis, a rare but potentially fatal side effect of clozapine. These blood draws, and the time lag in receiving reports from central labs, can add several more visits to the caregivers' treatment plan, which may not be feasible for the patient nor the treatment team. This contributes to a very low prescription rate for clozapine, making it one of the most underutilized evidence-based treatments in the field of mental health.

The objective of this work is to progress toward a point-of-care approach to monitor both white blood cells and clozapine within a clinical setting. This would significantly lower the burden associated with clozapine treatment by allowing both tests to be

performed rapidly during a single doctor's office visit or at the pharmacy. Specifically, I have developed and studied novel clozapine detection schemes based on electrochemical signal amplification in chitosan-based films. Moreover, I have investigated impedance cytometry coupled with hydrodynamic focusing and osmotic lysis to provide label- and reagent-free differential white blood cell counting capabilities. Finally, I have integrated the components in a microsystem capable of concurrent sensing of both biomarkers in whole blood samples. This proof-of-concept device lays the foundation for a fully integrated and automated lab-on-a-chip for point-of-care or even at-home testing to ensure treatment adherence, efficacy, and safety. This will allow for broader use of clozapine by increasing convenience to patients as well as medical professionals, thus improving the lives of people affected by schizophrenia through personalized medicine.

# MICROSYSTEMS INTEGRATION TOWARDS POINT-OF-CARE MONITORING OF CLOZAPINE TREATMENT FOR ADHERENCE, EFFICACY, AND SAFETY

by

Thomas E. Winkler

Dissertation submitted to the Faculty of the Graduate School of the
University of Maryland, College Park in partial fulfillment
of the requirements for the degree of
Doctor of Philosophy
2017

Advisory Committee:
Professor Reza Ghodssi, Chair/Advisor
Professor William E. Bentley
Professor Deanna L. Kelly
Professor Gregory F. Payne
Professor Ian M. White

"Engineers
turn dreams
into reality."

*—Hayao Miyazaki*

# Acknowledgments

My dissertation project, and my time as a graduate student more broadly, would have been impossible without the help of many others. The following is a brief word of gratitude, although the written word is insufficient to express my true appreciation.

First and foremost, I want to thank my advisor Prof. Reza Ghodssi. You supported me on my endeavor in every way possible, from start to finish and beyond, and without your guidance I would not be the researcher I am today. Special thanks are further due to my committee members Profs. William Bentley, Deanna Kelly, Gregory Payne, and Ian White, for the many fruitful discussions and the encouragement over the years. To Prof. Ian White: thank you for also serving as my teaching mentor, both by collaboration as well as by excellent example.

I am immensely grateful to Dr. Hadar Ben-Yoav, alongside whom I started the MiND project and worked on the clozapine sensor. Your experience – which you shared so freely – was an invaluable resource. I am deeply indebted moreover to the other researchers that the MiND project brought together and who made it possible: Sheryl Chocron, who worked on selectivity, interference, and chemometrics for the clozapine sensor; George Banis, who continued her work on protein binding of clozapine; Dr. Eunkyoung Kim, whose chitosan-catechol system provided the basis for a large part of my work on clozapine sensing, and whose chitosan-carbon nanotube sensor overcame many of its limitations; Dr. Mijeong Kang, who further built on that work by developing the chitosan-graphene sensor; Stephanie Feldman, Christopher Kitchen, and the rest of the team at the Maryland Psychiatric Research Center, who led the clinical aspects of the project.

To the whole MEMS Sensors and Actuators group present and past: thank you for all your help and discussions along the way, I have learned from each of you and enjoyed our time together. Special mentions are due for my mentors Dr. Mariana Meyer, who helped me get settled in MSAL, and Dr. Konstantinos Gerasopoulos, who helped me on

the home stretch toward graduation. I was fortunate to mentor and work with a number of talented undergraduate students myself: Robert Dietrich, Sarah Brady, Delaney Jordan, Ashlyn Lee, Sukriti Ghosh, Stephen Semick, Florence Stevenson, and Eugene Froimchuk. You made it possible to explore side projects such as 3D microfluidic molds and studying the molecular processes in the chitosan-catechol sensor, and though not all of those worked out, they were all valuable contributions.

One of the things I appreciated most during my time at UMD was the openness and collaboration across multiple laboratories and research groups. This spirit is exemplified by the BioChip Collaborative (both in its original form and current incarnation) and all its members, thank you for so readily sharing expertise and equipment (Bentley group, Rubloff group, Raghavan group, *etc.*). I also appreciate the equipment support I received from the laboratories of Profs. DeVoe, Jewell, Murphy, and especially Profs. Bruce Kaine and Kevin Osborn at the Laboratory for Physical Sciences, who lent me the critical instrumentation for differential impedance cytometry.

Moreover, I want to thank the technical staff at the FabLab, AIMLab, and TerrapinWorks for keeping fabrication and characterization equipment working smoothly and helping me out with issues big and small in using the facilities. To the administrative staff in ISR and BioE, especially Regina King, Pamela White, Vicci Barrett, and Dr. Tracy Chung: thank you for your willingness and responsiveness in your assistance with my varied administrative concerns, questions, and near-deadline requests over the years.

Further thanks go to *Fulbright Austria* and the *Institute for International Education* for their financial support, but even more so for the opportunity of going to the US for my graduate studies.

And last but surely not least, I would like to thank my parents, Anna and Alfred, my brothers, Stefan and Martin, my friends, and especially my partner Brianna, for being there for me in so many ways throughout my (grad student) life.

# Contents

# List of Figures

# List of Tables

## List of Common Abbreviations

| | |
|---|---|
| AC | alternating current |
| ACD | acid-citrate-dextrose |
| CNT | carbon nanotube |
| DC | direct current |
| DI | deionized |
| EDTA | ethylenediaminetetraacetic acid |
| ELISA | enzyme-linked immunosorbent assay |
| Fc | 1,1'-ferrocenedimethanol |
| IDE | interdigitated electrode |
| PB | phosphate buffer |
| PBS | phosphate buffered saline |
| PDMS | polydimethylsiloxane |
| Ru | hexaammineruthenium |
| TBS | tris buffered saline |
| TMVLP | tobacco mosaic virus-like particle |

# Chapter 1

# Introduction

## 1.1 Motivation & Background

Lab-on-a-chip devices have rapidly proliferated in the past decade, resulting not only in the creation of the eponymous journal but also in a significant number of commercialized applications [1]. These research efforts, however, have by comparison only marginally extended into the field of mental health. Examples include the detection of neurotransmitters, analysis of stress levels from saliva, and monitoring of lithium treatment for bipolar disorder [2–4]. To the best of my knowledge, there exist no specific applications towards schizophrenia as yet.

Schizophrenia is one of the most challenging and complex neuropsychiatric disorders afflicting humanity. The lifelong devastating illness is characterized by an abnormal interpretation of reality. The burden of the disorder is high, accounting for 0.5% of the global disability-adjusted life years lost – more than all STDs (except HIV) combined [5]. Its direct and indirect costs are estimated to exceed $150 billion annually in the US alone [6]. The recommended treatment, for lack of a cure, is lifelong antipsychotic medication [7]. However, 30–50% of patients do not respond to first line psychiatric drug treatment [8]. Clozapine is the most effective drug available, providing symptom relief even to patients unresponsive to other second-line medication [9]. It is also the only FDA-approved antipsychotic for treatment-resistant schizophrenia.

In spite of the overwhelming evidence of the superior efficacy of clozapine compared to other drugs, it is prescribed infrequently in the United States – to less than 10% of all patients with schizophrenia, a disproportionately lower rate than the estimated prevalence of treatment-resistant schizophrenia [10]. A major factor in this underutilization is the

required invasive monitoring at regular intervals for agranulocytosis (a severe loss of granulocytes, a type of white blood cell) [11]. To avoid this rare but potentially fatal side effect, the FDA stipulates weekly blood draws for at least the first six months of treatment, with decreasing intervals thereafter [12]. The current FDA classification of an abnormal event – requiring interruption of clozapine treatment – involves a granulocyte count of less than 1,000/µl, or 500/µl for people with naturally low granulocyte counts. These tests imply a significant burden for both the patient and treatment team in terms of unpleasant venous blood sampling, wait times for results from centralized labs, logistics of organization and transportation for these office visits, *etc.*

Supplementary tests for accurate clozapine dosage control have been shown to improve outcomes and decrease the risk of toxicity [7,13]. Clozapine is one of the few antipsychotics with a well-established effective range of blood plasma levels, namely 1–3 µM [14]. Below this range the drug is unlikely to provide relief, while above toxicity side effects such as seizures become much more likely. However, the blood draws for clozapine monitoring are rarely implemented, especially beyond the initial titration phase, *i.e.* where the dose is gradually increased. These supplementary blood draws, again requiring testing at centralized labs, further compound the aforementioned burden to patients and clinicians in terms of cost and time. Thus, real-time monitoring of both clozapine and granulocytes at the point of care would have significant positive impact by allowing physicians to rapidly adjust dosages to reach safe and effective levels as well as check for onset of agranulocytosis [8].

Furthermore, nonadherence to medication regimens is a widespread challenge in medical treatment [14]. This applies even more so to people with neuropsychiatric disorders such as schizophrenia, where patients may be more prone to actively stop medicating (in addition to the generally prevalent passive forgetfulness). Indeed, nonadherence is found to be one of the more frequent reasons for relapse, rehospitalization, and higher treatment costs [15]. Currently there is no good way to measure adherence; testing for


Figure 1.1: Schematic showing the current burdensome monitoring associated with clozapine treatment, and the envisioned point-of-care monitoring solution.

presence of antipsychotics in the blood solely for this purpose is burdensome and not cost effective. However, monitoring blood levels to optimize clozapine efficacy and reduce the risk of side effects will also allow physicians to know if patients are adherent to their treatment or need interventions to support adherence. Thus, non-cumbersome blood level monitoring is critical to maximizing success and safety for each patient.

It is essential that physicians who prescribe clozapine or would consider prescribing clozapine find this type of device equally important. Pilot data from my collaborator Dr. Deanna Kelly demonstrates that point-of-care monitoring of clozapine, as illustrated in Figure 1.1, would indeed represent a major advance in the treatment of schizophrenia. In an IRB-approved anonymous survey of physicians, this is the number one ranked solution to improving barriers of prescribing [11]. The survey consisted of a series of questions ranking barriers to the use of clozapine and possible ways to improve clozapine utilization from 1 (strongly disagree) to 5 (strongly agree). It further included a series

of questions asking specifically whether point-of-care devices would improve current care and increase their willingness to prescribe clozapine. Among 28 listed barriers (clinical, nonclinical, and side effects) to more frequent use of clozapine, the two highest ranked choices were 1) patients will likely be nonadherent to blood work (score 3.7/5) and 2) the burden of blood work on the patient (3.6/5). Also, among nine potential solutions for increased clozapine use, clozapine levels and white blood cell measurement in the physician's office or pharmacy was top-ranked (4.0/5). Overall, physicians agreed that such a point-of-care device would improve care and increase their prescription of clozapine.

## 1.2 Summary of Accomplishments

No studies, to date, have developed microsystems designed for mental health therapeutic drug monitoring. With no superior treatment on the horizon for schizophrenia, research that allows using clozapine more frequently could improve the lives of potentially millions of patients affected by this devastating illness. My research in this dissertation aims at developing a proof-of-concept device for concurrent monitoring of clozapine and granulocytes, schematically illustrated in Figure 1.2, that is suitable for translation to the point of care such as the physician's office or pharmacy. This will enable physicians to easily obtain clozapine levels for early detection of nonadherence and optimization of plasma levels for clinical response while avoiding side effects and toxicity. A major aspect of this thesis is the integration of the critical components on a single lab-on-a-chip. As discussed herein, work has been done on differential blood cell counting and clozapine sensing, but my research demonstrates the first integrated device approach to monitor both cellular and acellular components of blood. By incorporating a unique and extensive plan for sub-system evaluation and integration, a crucial aspect that has often been overlooked, I overcome previous barriers of detection. These concepts also extend beyond the original application, and can be adapted for many other areas of mental and

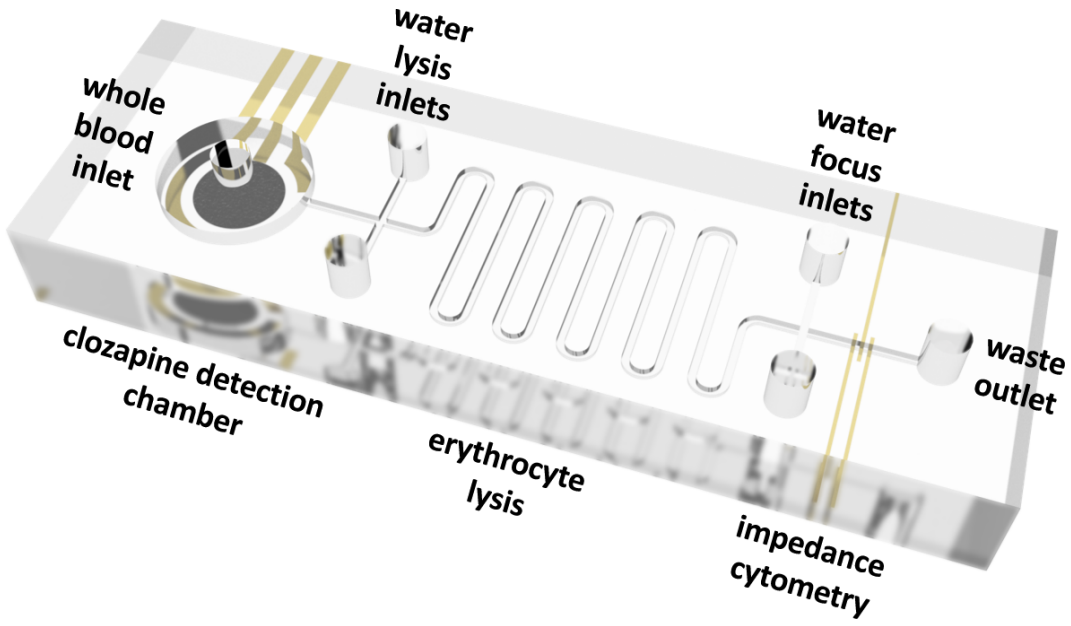


Figure 1.2: Schematic rendering of the integrated microsystem developed in this thesis.

general health care and treatment that require simultaneous monitoring of both blood cells and plasma biomarkers.

### 1.2.1 Miniaturizable Electrochemical Clozapine Detection Mechanisms

In this thesis, I present three related but distinct approaches to detecting clozapine in complex biological samples based on its electrochemical activity. Previously published techniques have shown good sensitivity but fallen short on selectivity, often resorting to extensive pre-treatment procedures. Here, I rely on a matrix of the biomaterial chitosan, further modified with the small redox-active molecule catechol, or combined with carbon nanotubes and/or graphene. First, I characterize sensing figures of merit for the chitosan-catechol redox cycling system, determining a detection limit of less than 1 μM, and demonstrating selectivity over other redox species such as clozapine's highly analogous metabolite norclozapine. I further assess film stability and the impact of the electrode material on clozapine sensing. My work not only demonstrates a novel sensing approach, but also yields a deeper understanding of the interplay between

biomolecules, biomaterials, and electrochemistry in this realm. Finally, the chitosan-carbon nanotube/graphene redox catalysis system is shown to offer distinct sensing capabilities, with high sensitivity to clozapine and selectivity over endogenous species in serum.

### 1.2.2 Reagent- and Label-free White Blood Cell Counting

In this thesis, I develop an easy-to-fabricate, microfluidic, impedance-based white blood cell counter. Existing approaches suffer from limited sensitivity or employ reagents or labels to enable differential cell counts. Here, I investigate two specific sub-system integration approaches for impedance cytometry – capable of label-free cell counts – intended to overcome these limitations. First, I conduct an in-depth study of its systems interplay with hydrodynamic focusing, whereby the sample is confined using non-conducting laminar sheath flows to increase performance. I demonstrate an up to 5-fold increase in sensitivity, and more importantly, shed light on the typically neglected importance of diffusion effects in such a system. Second, I consider the systems interplay between impedance cytometry and osmotic lysis. Therein, pure water instead of chemical agents is utilized to lyse the 1,000-fold more prevalent erythrocytes to enable leukocyte counts. I find that osmotic lysis is over 99.9% effective and does not interfere with cytometry performance.

### 1.2.3 Microsystem Integration for Dual Plasma/Cellular Sensing

In this thesis, I ultimately integrate the aforementioned subsystems into a holistic microsystem for concurrent cellular and acellular (small-molecule) whole blood analysis. To the best of my knowledge, no such device exists as yet. I evaluate plasma skimming, a passive hydrodynamic approach for separating blood plasma and cells, for its suitability in such a device. I utilize a proof-of-concept, label-free, impedimetric immunoassay approach for this purpose. With this, I demonstrate the detection of antibodies in whole

blood without the need for pumps or bulky readout equipment, but discover limited continuous-flow capabilities. For the integrated clozapine treatment monitoring device, I therefore integrate the redox catalysis system in-line and upstream from the white blood cell counting sub-systems. I showcase whole-blood clozapine detection and blood cell differentiation capabilities with my final microsystem, highlighting the feasibility of concurrent clozapine and granulocyte monitoring.

## 1.3 Literature Review

### 1.3.1 Clozapine Pharmacology

Typically, clozapine is administered orally in divided doses totaling 300 to 800 mg per day [7,12]. This dosage is gradually reached over an initial titration period of $\sim$ 2 weeks under close monitoring by the treatment team. To enter systemic circulation, clozapine has to pass through the liver where it undergoes extensive first-pass metabolism. It acts as a substrate for cytochrome P450 enzymes, particularly the 1A2 variety, with the two major stable products being *N*-desmethylclozapine (norclozapine; shown alongside clozapine itself in Figure 1.3) and clozapine *N*-oxide [16]. This limits bioavailability of the drug, necessitates the typically divided dosing mentioned earlier, and links bioavailability closely to factors interacting with these hepatic pathways such as other drugs, smoking, or inflammation [17]. Once in circulation, therapeutic availability of clozapine is limited by its strong affinity to serum proteins. Up to 97% of clozapine is present in a bound state, mostly with serum albumin and alpha-1 acid glycoprotein (AAG) [18,19].

While the therapeutic mechanism of action of clozapine is poorly understood, it shows a wealth of interactions with nervous system receptors [20]. Antagonism to dopamine type 2 and serotonin type 2A receptors is likely central [21]. The metabolite norclozapine is thought to have weak therapeutic activity as well, though possibly only in combination with clozapine itself. The lowest effective plasma level of clozapine is

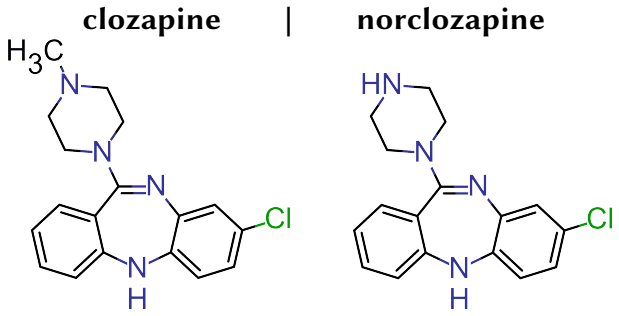


Figure 1.3: Chemical structures of the antipsychotic clozapine (left) and its metabolite norclozapine (right).

commonly reported as $\gtrsim$ 1 µM (350 ng/ml) [14]. Like many antipsychotic drugs, clozapine can also cause a range of adverse side effects [12]. Central and autonomous nervous system effects like drowsiness and hypersalivation are among the most common; many of these side effects can be effectively managed, for instance with co-prescribed medications. Some serious neural and cardiac adverse reactions such as seizures and cardiac arrest are linked to clozapine toxicity, *i.e.* excessively high levels of the drug $\gtrsim$ 3 µM (1000 ng/ml) [13]. The gradual and controlled upward titration at the start of treatment has proven to both help efficacy and decrease toxicity.

Other adverse effects appear to be independent of dosage [13]. The most severe and least uncommon in this category is agranulocytosis, afflicting up to 1% of patients. The condition can be fatal if granulocyte levels drop to less than 500/µl, severely compromising the immune system and leaving the patient vulnerable to infection. The mechanism behind clozapine-induced agranulocytosis is still unclear [22]. It has been established that both myeloid precurser cells as well as adult neutrophils are affected, decreasing the existing white blood cell population and compromising regeneration. However, neither clozapine nor its stable metabolites have shown toxicity to these cells. Metabolism of clozapine into a reactive intermediate inside the affected cells themselves could be responsible. The low patient incidence appears to be the result of a complex, multi-factorial set of parameters determining predisposition for clozapine-induced agranulocytosis.

### 1.3.2 Clozapine Detection Approaches

In current procedure, the preferred method for measuring clozapine plasma levels is a combination of high-performance liquid chromatography and tandem mass spectrometry (HPLC/MS/MS), the method of choice for therapeutic drug monitoring in general [14]. First, patient samples undergo sample preparation that may include dilution, centrifugation, and the addition of reagents. Then, a small (microliter-scale) volume is injected into the mobile phase passing through the chromatography column, where the sample is fractionated based on physical interactions with the stationary phase. At the outlet, an ionized gas is created from the liquid and two-stage mass spectrometry is applied to the various sample fractions to identify constituents based on their mass-to-charge ratios. This approach allows for sensitive simultaneous detection of many different analytes with a limit of detection (LOD) as low as 5 nM for clozapine [23]. However, the sample preparation is clearly time-consuming and requires a trained technician or costly automation, which also applies to the the bulky and expensive requisite equipment itself. Moreover, due to the reagents employed in the process, protein-bound clozapine is freed prior to measurement. Thus, laboratories report the total (protein-bound and -unbound) clozapine and norclozapine concentrations. To determine bound and -unbound fractions, equilibrium dialysis has to be applied prior to HPLC/MS/MS [24].

It is immediately apparent that the HPLC/MS/MS approach is not very amenable to translation to the point of care. Research has been done on miniaturizing such systems, especially in terms of the HPLC column and sample ionization [25,26]. However, the nature of mass spectrometry – based on ionized compounds being subjected to high external fields in a near vacuum – renders it impractical for lab-on-a-chip systems for the foreseeable future. Toward clozapine detection, other researchers have thus investigated replacing the signal transduction mechanism. Two of the earliest reports in this regard show detection based on ultraviolet absorbance (LOD 15 nM) [27] and amperometric detection (LOD 60 nM) [28], with a later report also demonstrating fluorimetric detection

(LOD < 150 nM) [29]. It becomes apparent that the detection limit – in all cases for clinical samples, though calculated using slightly different methodologies – is compatible with the clinical range independent of the transduction, demonstrating the advantages of HPLC. Both optical approaches rely on the highly aromatic nature of clozapine seen in Figure 1.3, yielding the necessary delocalization of pi electrons. The amperometric detection relies on clozapine's inherent redox activity.

Initially reported by Kauffmann *et al.*, clozapine has a standard reduction potential of $E^{o} \sim +0.95$ V (*vs.* standard hydrogen electrode), undergoing a partially reversible two-electron, one-proton reaction as shown in Figure 1.4 [30]. The overall reaction scheme is quite complex, with a number of products of varying stability and redox activity formed, as demonstrated by Leeuwen *et al.* utilizing electrochemistry followed by on-line LC/MS for analysis [31]. However, for most electroanalytical purposes, the aforementioned primary reaction dominates. Due to the involvement of a proton in the reaction, the reaction potential of course depends on the pH of the solution – at physiological pH and with respect to a common Ag/AgCl reference (henceforth the default in this thesis unless noted otherwise), it is observed around $E^{o\prime} = +0.37$ V.

Utilizing chromatography in the analysis methods retains the advantage of at least partially decoupling selectivity (from chromatography) and sensitivity (from transduction). However, this also retains HPLC's aforementioned limitations in terms of sample preparation and reagent requirements. Capillary zone electrophoresis offers a way to reduce those limitations with lower requirements in equipment bulk, reagent volume, and sample preparation, while preserving sample fractionation capabilities. Instead of physical interactions within the HPLC column, the electrophoretic mobility (broadly, size-to-charge ratio) of molecules determines their transition time through a glass capillary under a strong applied potential (kV range). For non-clinical samples, a simple phosphate buffer (PB) can serve as a running buffer. However, even in this case, molarity and pH (typically < 4) are critical to ensure selectivity, as both these parameters strongly affect the

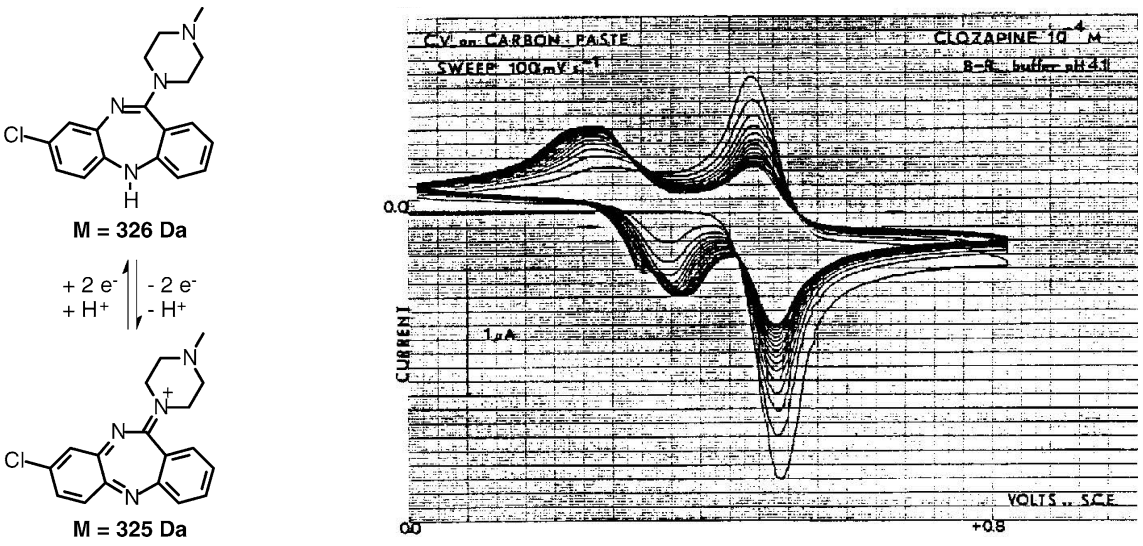


Figure 1.4: (left) Dominant electrochemical reaction scheme of clozapine. Adapted with permission from [31]. (right) Cyclic voltammogram of clozapine in buffer measured using a carbon paste working electrode and saturated calomel reference electrode. Note that oxidative current is shown negative in this plot, opposite the convention used otherwise throughout this work. The dominant reaction appears at 0.5 V here (due to the pH 4 buffer and the reference electrode utilized), with a secondary reaction appearing at a lower potential over time. Reproduced with permission from [30].

electrophoretic mobility of the analytical species [32,33]. With UV absorbance detection, Hillaert *et al.* achieve a detection limit below 75 nM. For handling biological samples, more sample preparation becomes necessary, particularly to avoid contamination of the capillary with proteins. Jin *et al.*, for instance, employ a two-step process utilizing ether to extract clozapine from whole blood samples into their electrophoresis buffer [34]. They couple this to the first demonstration of an electrochemical detection approach, utilizing a custom-made carbon fiber disk electrode and amperometric readout for a detection limit of 420 nM. Raggi *et al.* also demonstrate detection from clinical serum samples, employing a different yet similarly involved sample preparation involving solid phase extraction [35]. Relying on UV absorbance detection, they show a clinical detection limit of 60 nM, comparable to that in buffer solutions by Hillaert *et al.* Finally, while not utilizing clinical samples, Sekula *et al.* demonstrate the importance of the employed working electrode for electrochemical readout [36]. With an ionically conductive rubber

phase coating applied to a metal substrate, they achieve a limit of detection of 146 nM.

Researchers have also studied approaches independent of chromatography or electrophoresis, potentially simplifying measurements further. A major hurdle in this regard is the lack of a selective biorecognition element – enzyme, antibody, aptamer – such as employed by glucose sensors, or indeed most biosensors. Although, as mentioned before, clozapine binds to dopamine type 2 and serotonin type 2A receptors, and is metabolized by cytochrome P450 1A2, none of these interactions are exclusive. The liver enzyme, for instance, also metabolizes a host of other antipsychotics and small molecules such as caffeine [37]. Thus, a biosensor concept designed around such recognition elements, like that by Paternolli *et al.*, offers only very poor selectivity in spite of a limit of detection below 150 nM in buffer solution [38]. Most researchers therefore attempt to leverage clozapine's redox activity – providing selectivity from the fact that only a small subset of species in serum are redox-active, and even fewer will be oxidized near the same +0.37 V – coupled with additional semi-specific physicochemical interactions provided by some form of electrode modification. This presents numerous advantages also down the line for miniaturization, as electrochemical sensors are relatively simple to implement (requiring only electrodes) and extremely sensitive instruments are available for readout [39]. Since the 1979 study by Kauffmann *et al.* [30], many examples using various electrochemical measurement techniques to quantify clozapine have been presented. For brevity, I will focus on works explicitly considering selectivity. Hernández *et al.* utilize a carbon paste electrode modified with sepiolite to initially absorb and pre-concentrate clozapine from a potassium nitrate-based buffer solution at pH 4.2 [40]. The electrode is then washed and transferred into fresh solution for measurement by differential pulse voltammetry. They are able to show detection of 200 nM clozapine in a serum sample by diluting it 12-fold into their pre-concentration solution. Hammam *et al.* utilize a hanging drop mercury electrode in neutral, de-oxygenated Britton–Robinson buffer to quantify clozapine by square-wave adsorptive cathodic stripping voltammetry [41]. By applying

a negative −0.7 V potential over 30 s, clozapine is adsorbed and pre-concentrated onto the mercury drop, and subsequently scanning the potential toward even more negative values reveals a clozapine reduction peak around −1.5 V. The utilized potential range explains the need for an oxygen-free solution, which would otherwise dominate the reduction signal. It should also be noted that the monitored reduction peak here is distinctly different from that of the typically monitored redox reaction at +0.37 V. For measurements in serum, they first precipitate proteins out of serum (using methanol and centrifugation) before spiking clozapine into the samples, diluting the serum 100-fold in the process, ultimately showing a detection limit of 100 nM. Farhadi *et al.* employ a glassy carbon electrode that they subject to anodic oxidation prior to use [42]. They argue that this enhances clozapine absorption onto the electrode in a pre-concentration step at open circuit potential for subsequent cyclic voltammetry measurements, all performed in a pH 6 phosphate buffer. For serum, they achieve a 25 µM detection limit by spiking clozapine into the samples before precipitating proteins out of solution, and diluting them 300-fold before measurements. Finally, Shahrokhian *et al.* coat glassy carbon electrodes with thin films of multi-walled carbon nanotubes and conductive polymer, polypyrrole doped with new coccine [43]. Experiments are carried out in de-oxygenated pH 5.4 Britton–Robinson buffer using linear scan voltammetry after an accumulation step. Serum samples spiked with 10 µM clozapine or less are successfully analyzed after precipitating proteins and diluting the samples 10-fold.

It becomes clear that, though about half of these studies have shown detection in the clinically relevant range, they all fall short on one count or another. None of them demonstrate detection directly in complex biological samples (blood, plasma or serum), which present challenges in terms of interference from other compounds, potential cross-reactivity between those and the analyte, or non-specific adsorption leading to fouling. Instead, all studies to date require relatively extensive sample pre-treatment in terms of dilution and protein precipitation, which is difficult to translate into a point-of-care device

from both technical and regulatory points of view. Some, moreover, require specialized and/or de-oxygenated buffer solutions for the measurements, where especially the latter is prohibitive for microsystems integration. Finally, none of these studies have attempted or investigated translation of their approaches into lab-on-a-chip-type systems.

### 1.3.3 White Blood Cell Enumeration

Blood cell counts are not only critical in clozapine treatment monitoring, but are in general the most commonly prescribed medical test, accounting for around 15% of all medical tests performed by volume [44]. The test plays a central role in diagnosing disorders ranging from anemia or leukemia to infection, based on the abundance of red and white blood cell, and platelets, illustrated in Figure 1.5 [45]. Traditionally conducted by manually counting cells in a stained blood smear on a glass slide under a microscope, automated techniques are now more common. These approaches have in turn driven the wide adoption of full differential counts, wherein leukocytes are quantified in terms of sub-populations – 30% lymphocytes, 5% monocytes, and granulocytes (themselves further split up into 62% neutrophils, 2% eosinophils, and 1% basophils). The gold standard is flow cytometry, where thousands of cells can be analyzed within less than a minute. As shown in Figure 1.6a, the sample is hydrodynamically focused to force single-file passage of cells past an array of detectors. These detectors typically consist of forward and side laser scattering, supplemented with fluorescent labels for population-specific surface antigens such as CD4, and impedance measurements. Information is thus collected on multiple dimensions on a cell-by-cell basis, and can subsequently be analyzed in terms of populations as well as in terms of rare events (*e.g.* for very rare and highly specific cell types such as circulating tumor cells).

Due to their ubiquity in medical diagnostics – combined with the fact that although flow cytometry equipment tends to be bulky, it already relies on microfluidics – blood cell counters have a long history of miniaturization [45,47–49]. Especially impedance

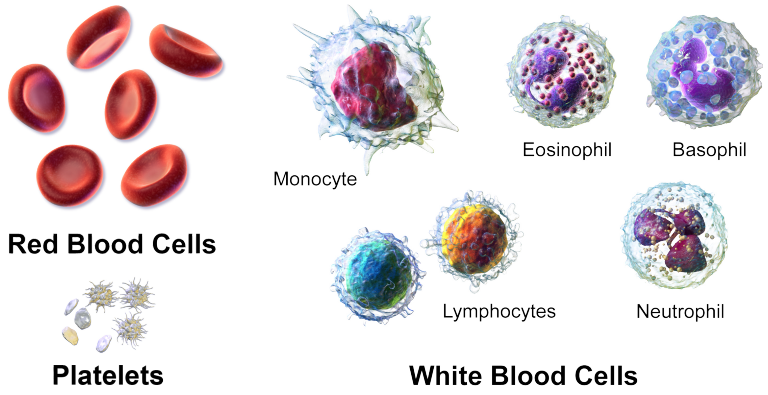


Figure 1.5: Schematic drawings of erythrocytes (top left), platelets (bottom left), and the major leukocyte subtypes (right). Reproduced with permission from [46].

cytometry is well suited towards integration in microsystems, as it does not rely on labels or complex optics [39,50]. The approach in its most basic form applies the Coulter principle illustrated in Figure 1.6b. In an electrolyte-filled channel with two chambers separated by an aperture of diameter $DA$, an impedance $Z_{\text{empty}}$ can be measured between two electrodes on either side of the aperture. As a particle (or cell) of diameter $\phi$ passes through the aperture, it displaces electrolyte, and thus – relative to the empty-channel impedance – causes an increase in absolute impedance [51]:

$$|\Delta Z| = \frac{\big||Z| - |Z_{\text{empty}}|\big|}{|Z_{\text{empty}}|} \propto \phi^3 / DA^2 \tag{1.1}$$

Consequently, the impedance signal $|\Delta Z|$ can be used to differentiate particles based on their size. This is useful for blood cell differentials, as there are significant differences in geometry: Discoid red blood cells with 6–8 µm diameters, compared to spherical white blood cells with diameters ranging from 6–20 µm for the various sub-populations.

The first lab-on-a-chip Coulter counter was presented by Larsen *et al.* in 1997 and is depicted in Figure 1.7 [53]. They utilize silicon micromachining to define 50 µm deep microfluidics, bonded to a glass wafer patterned with gold electrodes. Due to the lack of a follow-up journal manuscript, details on this device and its characterization are unfortunately limited – many device and design parameters are unspecified, and the

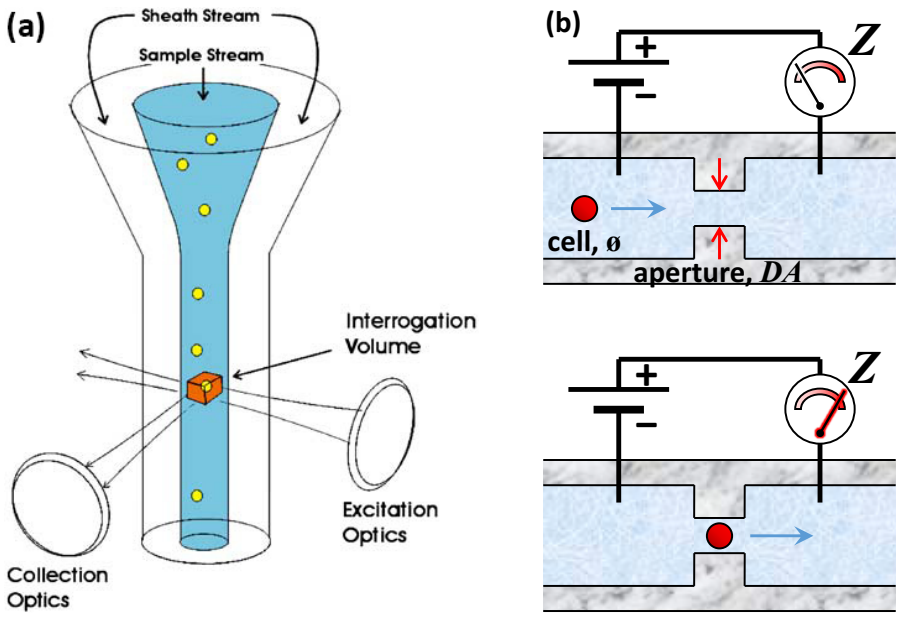


Figure 1.6: Schematics showing the working principles of (a) an optical flow cytometer; reproduced with permission from [52]; and (b) a Coulter counter with the particle in red passing through the aperture in the lower image.

authors are unable to obtain reproducible results even with only polystyrene beads. Critically, however, this work identifies the advantages of hydrodynamic focusing. Specifically, it employs two layers of sheath flows around the sample (an electrolyte, as well as a non-conducting sheath flow) and includes the option for an additional out-of-plane sheath flow to assist in vertical particle positioning. The authors note that hydrodynamic focusing greatly reduces the risk of device clogging in general, and that a non-conductive sheath flow allows for dynamic adjustment of the sensitivity.

The first work to actually present cell counting results from a lab-on-a-chip was that by Gawad *et al.* in 2001 [54]. Their device consists of platinum electrodes (20 µm length, width, and spacing) on glass and microfluidics (20 µm width and depth) defined in photosensitive polyimide, covered with planar polydimethylsiloxane (PDMS). Two pairs of electrodes and two external resistors each serve as one leg in a Wheatstone bridge circuit, allowing for sensitive differential readout of the signal (assuming only one electrode pair is occupied by a cell at any given time). Specifically, they show

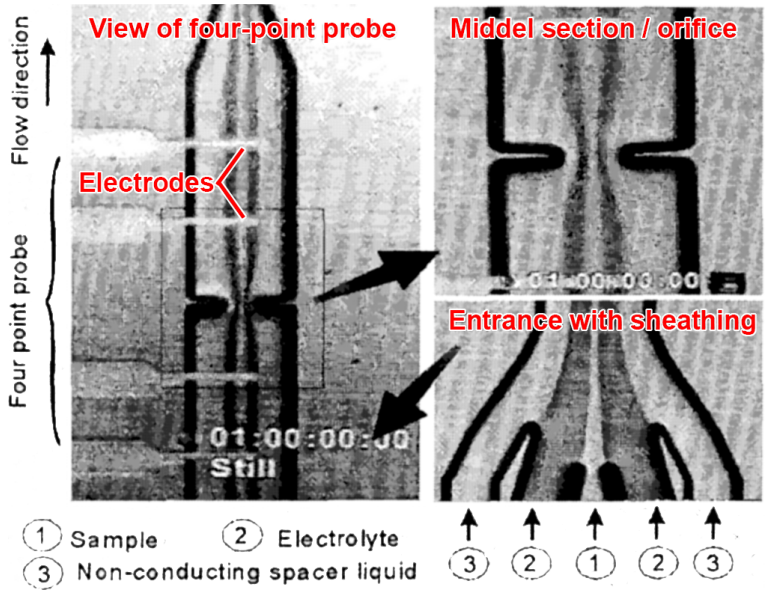


Figure 1.7: Micrograph showing the first microfabricated Coulter counter. As particles in the central sample stream ① pass the electrodes, the measured impedance changes. The sample flow is sheathed by electrolyte ② and deionized water ③. Reproduced with permission from [53].

being able to differentiate polystyrene particles, erythrocytes, and ghosts (red blood cells emptied of their contents). While the first two populations can be separated simply based on geometry as explained above, the latter two are virtually identical in that regard. The breakthrough in population separation capabilities here relies on the realization that the impedance at different signal frequencies reveals different information about the particle in question. While direct current (DC) or low-frequency alternating current (AC) impedance is sensitive to cell size, higher-frequency AC probes the internal structure of the cell as illustrated in Figure 1.8. The authors develop the relevant theoretical background for this conclusion based on an equivalent circuit model of the cell as a spherical shelled particle (which I explore in more depth and build upon in Subsection 3.1.2). Furthermore, they analytically and numerically consider advantages of a parallel facing electrode layout compared to the co-planar electrode layout used both in their own experiments and in Larsen *et al.*'s device.

The final study of note was presented by Holmes *et al.* in 2009 [55]. Utilizing

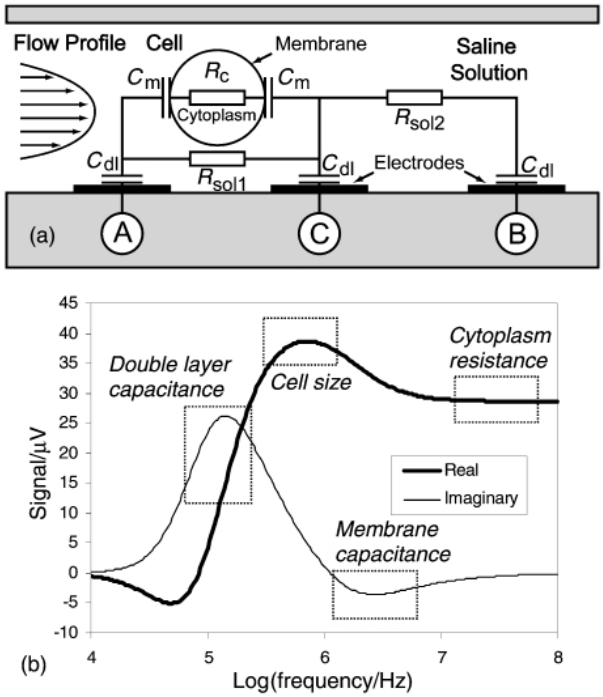


Figure 1.8: (a) Simple equivalent circuit model of a cell as a spherical shelled particle between an electrode pair. (b) Signal response as a function of AC signal frequency showing that different frequencies are sensitive to different cellular properties. Reproduced with permission from [54].

fabrication process and dimensions practically identical with those by Gawad *et al.*, they realize the parallel facing electrode layout by aligning and pressure-bonding two identical chips, pictured in Figure 1.9a–b. Their readout circuitry employs transimpedance amplifiers for each of two electrode pairs feeding into a lock-in amplifier (more specifically one for each measurement frequency) for differential readout. By pre-treating whole blood samples with saponin and formic acid (which also serve as a lysis agent) off-chip, the authors are able to differentiate leukocytes, monocytes, and granulocytes from their dual-frequency impedance measurements as shown in Figure 1.9c. They corroborate these results with analysis of purified sub-populations and on-line microscopy. A follow-up paper by the same research group further expands on this by integrating the aforementioned pre-treatment on-chip in a device with a somewhat larger (40 μm width and depth) cross-section, and by validating results against clinical laboratory analysis

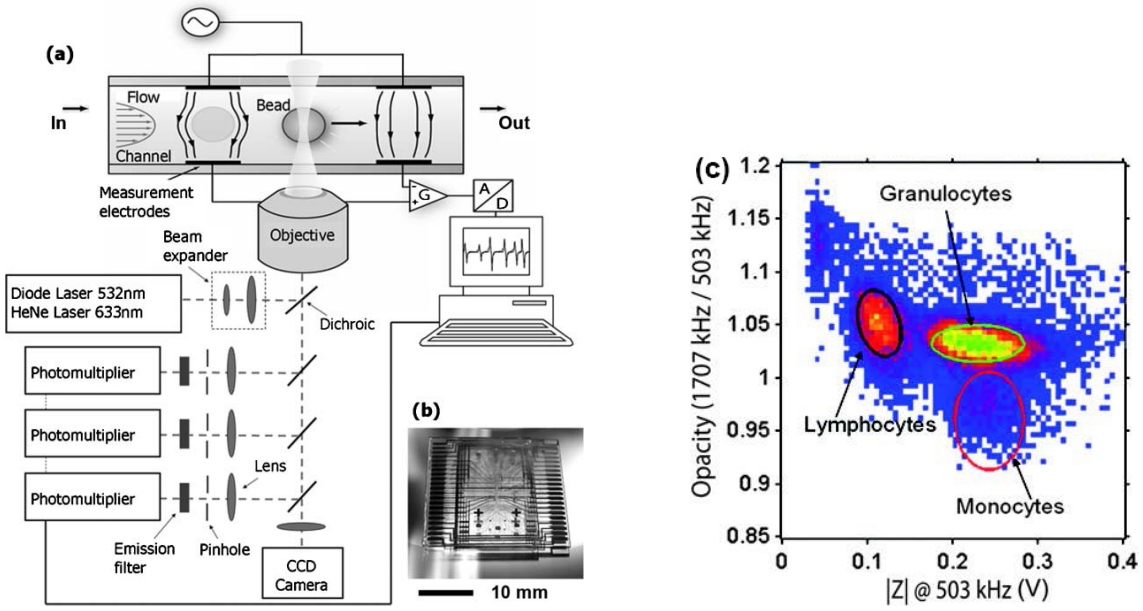


Figure 1.9: (a) Schematic of the parallel-electrode impedance cytometer combined with an external optical system for validation purposes. (b) Picture of the microfluidic impedance cytometry chip. (c) Impedance scatter plot of low- and high-frequency signals from a whole blood sample, pre-treated off-chip with saponin/formic acid, with the three major white blood cell populations highlighted. Reproduced with permission from [55,57].

[56].

The three seminal studies described above were followed by numerous advances in theory and refinements in experiments (*e.g.* in terms of cell positioning, or in post-detection sorting), discussed in depth in the excellent review papers on the subject [49,52,58–64]. These also lay out alternative transduction approaches, in part enabled by progress in miniaturization of optical components and broader trends in novel microfluidic concepts. This includes exploratory research such as lens-free optical cytometry [65], magnetic levitation of blood cells with smartphone-based readout [66], paper-based devices [67], and *in-vivo* optical flow cytometry [68]. Some of these developments, however, have also contributed in bringing commercial devices to market, with two in particular standing out: The Chempaq XBC, and the HemoCue WBC Diff. Both rely on a piece of equipment integrating necessary and reusable electronic and mechanical components for automated analysis and readout (~$5,000 in the case of the HemoCue;

no figures available for the Chempaq), as well as disposable and comparatively cheap cartridges (~$5 in the case of the HemoCue) for sample handling. The Chempaq XBC, shown in Figure 1.10, distinguishes itself as being possibly the earliest example of such a device and weighing less than 2 kg [69]. It combines an optical readout of hemoglobin with impedance analysis for white blood cells. The cartridge accepts a whole blood sample as small as 10 µl *via* capillary action, of which a metered 3 µl is mixed with pre-packaged liquid reagents upon insertion into the device. These reagents lyse erythrocytes, enable optical hemoglobin measurements, and affect leukocytes such that they can be distinguished based on size alone. Liquid flow inside the cartridge is then actively pressure-actuated, with flow sensors providing feedback. The cells pass through an aperture – laser-machined separately from the rest of the cartridge in a polymer membrane – that divides two compartments housing a bulk electrode each interfaced to external contacts. With the reagent-exposed blood samples, this allows for a three-part differential white blood cell count. The HemoCue WBC Diff, shown in Figure 1.11, smaller and lighter by about 30%, distinguishes itself as the only commercial product capable of a five-part white blood cell differential [70,71]. Although the use concept is similar to that of the Chempaq, the technology is quite different: It relies on optical image analysis of stained blood cells. The cartridge again utilizes capillary action for sampling of blood, whereafter the (in this case, dry) reagents for red blood cell lysis and white blood cell staining mix with the sample. Unlike with the Chempaq, however, the cartridge does not include any other components or functions, leading to a much simpler (and thus likely cheaper and more robust) design. The cartridge is then inserted into the reader, where an image is taken and the full five-part differential result displayed on algorithmic analysis of an optical image corresponding to $\sim 0.2$ µl of sample.

Interestingly, studies have been carried out with both systems geared specifically toward point-of-care monitoring of granulocytes in clozapine patient populations [72,73]. Nielsen *et al.* utilize the Chempaq XBC and focus mostly on the patient burden. With a

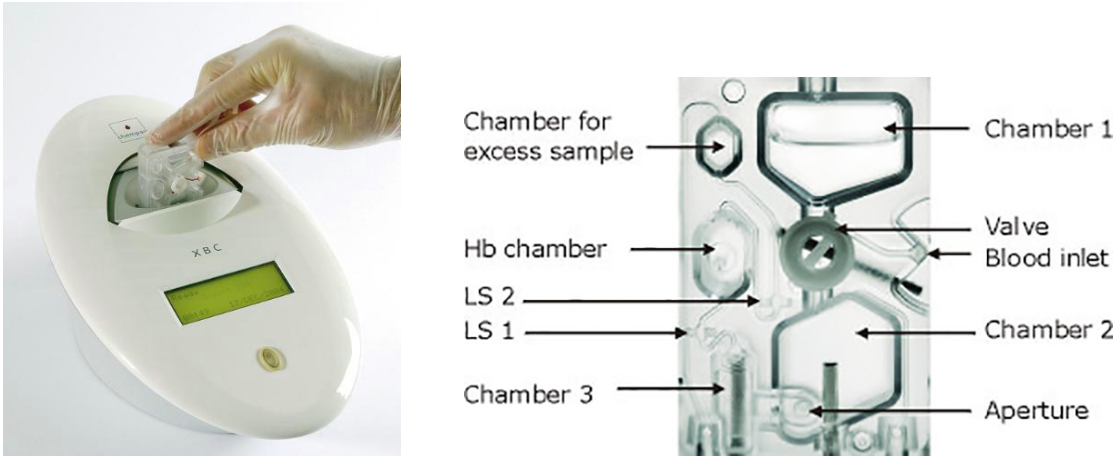


Figure 1.10: The Chempaq XBC device and corresponding cartridge [69,71].

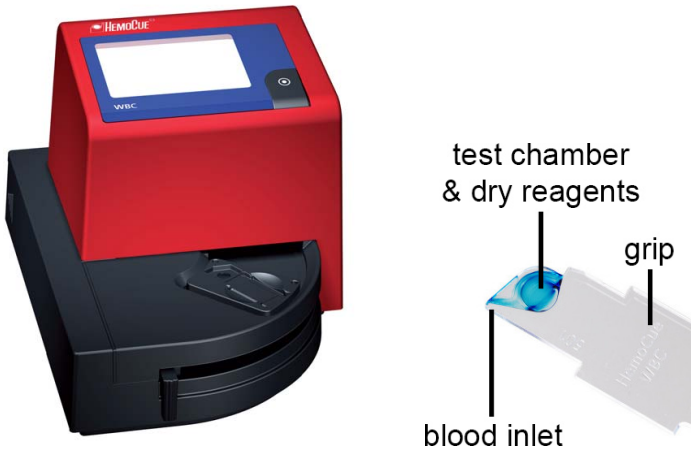


Figure 1.11: The HemoCue WBC device and corresponding cartridge. The components shown are practically identical for the WBC Diff [71].

77 patient sample size, they find that the point-of-care device significantly reduces pain and increases convenience, highlighting the conceptual advantages. Bui *et al.* utilize the HemoCue WBC Diff and focus mostly on clinical accuracy *versus* gold standard laboratory tests. With a sample size of 60, they determine that point-of-care measurements can serve to screen for agranulocytosis. For diagnosis, however, they suggest that follow-up testing utilizing venous sampling is called for. This is due to the general differences between venous and capillary blood samples (with regulatory limits only having been established for the former), as well as the generally higher variability, even within-patient, for the latter [74]. It should also be noted that all available data for these devices comes from

Europe; neither are available in the US.

Overall, while impressive progress has been made in point-of-care differential blood counts, both research and commercial devices suffer from drawbacks. A notable limitation is the reliance on chemicals to achieve sufficient cell type differentiation. For eventual clinical application, limiting the amount of required chemicals is an important consideration, as additional reagents complicate lab-on-a-chip packaging (*cf.* Chempaq cartridge). Moreover, the fabrication complexities of the multi-layer devices by Holmes *et al.*, or the assembly of Chempaq cartridges from multiple separately manufactured components, represent practical drawbacks. Finally, these single-purpose devices cannot easily be integrated with other sensing modalities, a critical point that I will explore further in the following Subsection.

### 1.3.4 Systems Integration

A significant challenge toward a combined clozapine and granulocyte monitoring device is the underlying systems integration of cellular and acellular sensors. The research-type blood cell sensors reviewed above are sometimes integrated with downstream sorting of the cell populations, analogous to benchtop fluorescence-activated cell sorting (FACS) – cell populations of interest are separated out, to then be subjected to further intracellular analysis, *e.g.* for DNA or protein biomarkers [49,61,75,76]. In continuous-flow type devices dealing with large cell numbers, *i.e.* microfluidic flow cytometers, such analysis is however typically carried out off-chip. For blood cell counters, to the best of my knowledge, hemoglobin analysis is the only existing example of simultaneously sensing a molecular species. This is implemented in both the Chempaq XBC, and by van Berkel *et al.* in a device based off that by Holmes *et al.* [69,77]. The analysis relies on absorption measurements of the red blood cell lysate to quantify the released hemoglobin in the sample stream.

Considering molecular species in serum, the literature is even more sparse. In

typical biomarker analysis, researchers generally employ some form of blood/plasma separation, as blood cells would add significant interference to most transduction methods – blocking optical pathways, adding mass, or changing the effective refractive index. Off-chip, such separation is typically accomplished through centrifugation and addition of chemical reagents. For lab-on-a-chip applications, researchers have attempted adapting similar concepts based on external force application, ranging from actual centrifugation to electrophoretic and acoustophoretic [76,78]. Such approaches, however, significantly increase the complexity both in terms of fabrication and integration of the overall lab-on-a-chip system. Passive approaches as illustrated in Figure 1.12 are based solely on blood flow behavior in the device through informed design of materials and geometry (cell sedimentation, cell filtration, inertial force separation, *etc.*). They also add complexity for fabrication, but do not require additional external components for operation. Most still suffer from additional drawbacks such as requiring dilution of the samples (*e.g.* micro-pillar arrays), which precludes tests for all but the most abundant plasma biomarkers, or conversely discarding the cellular fraction during or after plasma separation (*e.g.* micro-filters). Only a few are theoretically capable of recovering both cellular and acellular components intact, and to the best of my knowledge Fan *et al.* published the only paper utilizing one such an approach in a biosensor [79]. Specifically, they detect an array of protein biomarkers in plasma skimmed off 10-fold diluted blood (I discuss the approach in more detail in Section 4.1) but discard the cellular fraction.

From both perspectives, the progress toward concurrent cellular/acellular sensing approaches remains unsatisfactory. The hemoglobin measurement represents a special case that is not easily generalized, as the protein features highly specific optical properties and is one of the most abundant biological targets available at a concentration of 10 mM (exceeding even that of glucose). Conversely, Peter Sorger notes the possibility for downstream recovery of the cellular fraction in the work by Fan *et al.* in an opinion piece in the relevant journal issue and acknowledges the promise of such an integrated

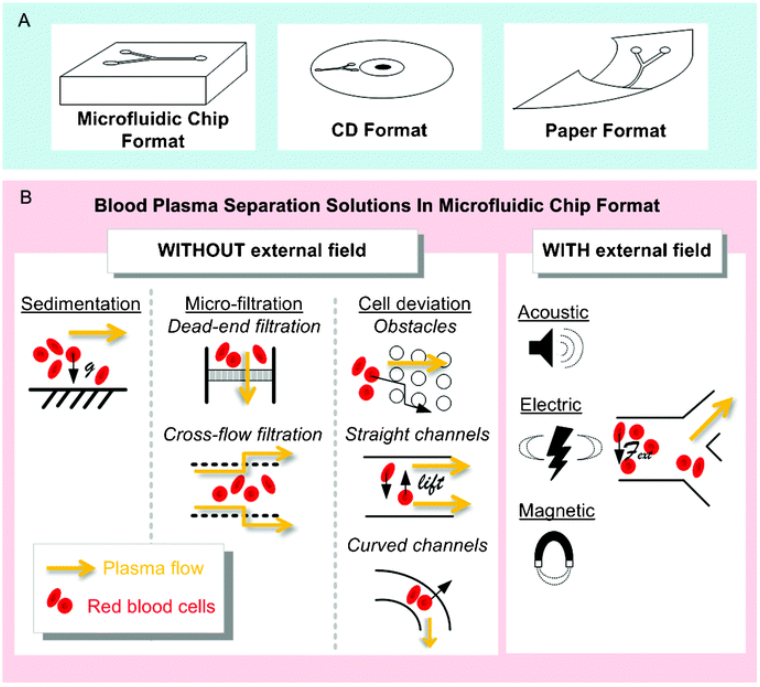


Figure 1.12: Illustration of different blood/plasma separation formats (a) and solutions specifically for microfluidic chips (b). Reproduced with permission from [78].

sensor. Yet this approach remains unexplored to date. The only works attempting to develop and study true cellular/acellular sensors are the recent ones by Huang *et al.* They employ a microfluidic device for capturing cellular and protein analytes from blood samples using antibody-coated magnetic beads as shown in Figure 1.13. Specifically, they target cancer-associated proteins and circulating cells – folate receptor protein and folate receptor-expressing cells, or prostate-specific membrane antigen and -expressing cells [80,81]. Both free proteins and the protein-expressing cells are captured by the magnetic beads, and the concentration assessed by fluorescence microscopy. The protein and cell signals are deconvoluted based on the large discrepancy in sizes, employing image analysis (cells are identified and then excluded from subsequent protein quantification) or a built-in membrane for cross-flow filtration. These microfluidic chips still suffer from a number of limitations, however. First, the use of magnetic beads limits the applicability to molecular analytes with matching traditional biorecognition elements (antibodies, aptamers, *etc.*) and to rare cell types – targeted at white blood cells, this approach

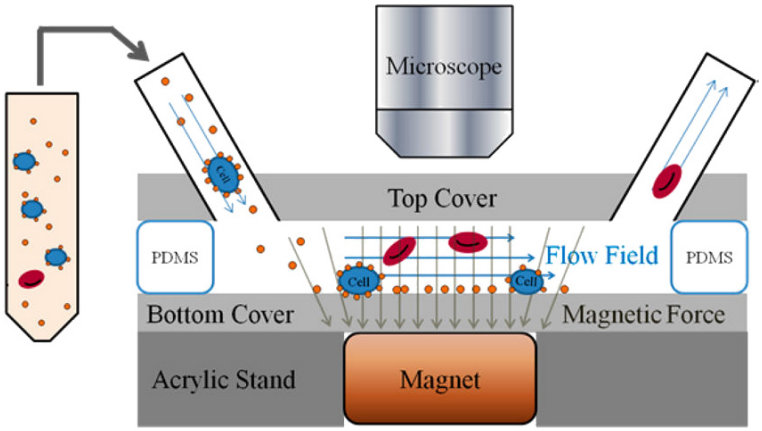


Figure 1.13: Schematic showing the operation principles of the microfluidic chamber designed for immunomagnetic detection of folate receptor-positive cells and free folate receptor. Reproduced with permission from [80].

would lead to signal saturation and/or device clogging. Second, in combination with the fluorescent labels, the approach necessitates readout optics as well as multiple changes in solution (sample, wash, label, wash), both factors that are not ideal for point-of-care applications as discussed earlier. Therefore, a broadly applicable cellular/acellular whole blood analysis microsystem will present a significant advancement in lab-on-a-chip technology.

## 1.4 Structure of Dissertation

In the preceding Chapter 1, I have discussed the underlying motivation for my research and reviewed related research in existing literature. In Chapter 2, I present the electrochemical detection of clozapine with the chitosan-catechol and chitosan-carbon nanotube/graphene signal amplification systems. In Chapter 3, I investigate the integration of hydrodynamic focusing and osmotic lysis with impedance cytometry, approaches that are critical for label- and reagent-free white blood cell counting. I proceed to discuss overall microsystem integration for concurrent clozapine and white blood cell monitoring in Chapter 4. Finally, I summarize the contributions of my dissertation and

cover future relevant directions of study in Chapter 5.

# Chapter 2

# Chitosan-based Clozapine Sensors with Electrochemical Signal Amplification

Chitosan is a versatile bio-derived hydrogel-forming polysaccharide. Its applications range from wound healing to drug delivery [82,83]. It can also easily be integrated into lab-on-a-chip systems, pioneered through efforts led by our group and collaborators [84]. In this regard, chitosan's selective electrodeposition capabilities are especially useful. With its pKa of 6.5, it is soluble in weakly acidic medium. Applying a cathodic current to induce electrolysis at an electrode locally generates an excess of protons, equating a localized increase in pH. This deprotonates chitosan's amine groups, insolubilizing the polysaccharide chains as shown in Figure 2.1. The resulting deposited hydrogel films are stable at neutral pH, and the amine groups allow for facile biochemical modification. Thus, the chitosan can serve as a matrix for anything from small molecules to proteins.

For the purposes of detecting clozapine, I consider two options in particular: First, chitosan can be modified biochemically with the small quinone catechol. Most of my own work focuses on the in-depth characterization of the resulting redox cycling system as laid out in Section 2.1. Second, nano-carbon compounds such as nanotubes or graphene can be dispersed in the chitosan. This redox catalysis system is discussed in Section 2.3. In this Chapter, I demonstrate that both of these compound film types exhibit high sensitivity and selectivity to clozapine, based on entirely distinct mechanisms, each with distinct strengths and weaknesses.

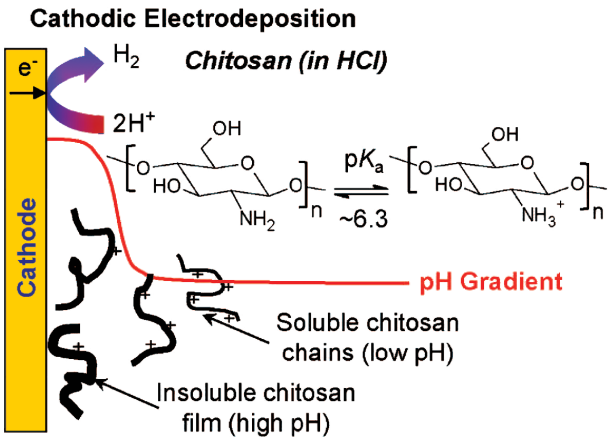


Figure 2.1: Schematic drawing of chitosan electrodeposition due to the highly localized pH gradient formed at the electrode, turning dissolved chitosan polymer into an insoluble chitosan hydrogel at the electrode. Reproduced with permission from [85].

## 2.1 Redox Cycling System

The chitosan-catechol redox cycling system was first presented by my collaborator Dr. Eunkyoung Kim in 2010 [86]. After chitosan electrodeposition, redox-active catechol ($E^{o\prime} = +0.14$ V [87]) can be electrochemically grafted onto the film, oxidizing it so the resulting 1,2-benzoquinone can react with the chitosan amine group as shown in Figure 2.2a. The resulting redox capacitor was initially demonstrated with model redox mediators 1-1'-ferrocenedimethanol (Fc; $E^{o\prime} = +0.23$ V) and hexaammineruthenium (Ru; $E^{o\prime} = -0.14$ V [88]) and was later utilized to detect the bacterial metabolite pyocyanin (a reducing mediator akin to Ru) [89].

I demonstrate that clozapine can act as an oxidizing mediator akin to Fc in this system, as schematically illustrated in Figure 2.2b–c. The drug can diffuse through the chitosan film and undergo an electron transfer reaction at the electrode (at $E \geq E^{o\prime}_{CLZ} = 0.37$ V). Without catechol in the film, oxidized clozapine would diffuse away and not participate further. In the catechol-modified chitosan film, however, catechol is immobilized in close proximity to the electrode and can reduce back oxidized clozapine. The same clozapine molecule can then be re-oxidized at the electrode, further contributing to the measured current. This action of clozapine as an oxidizing mediator results in a

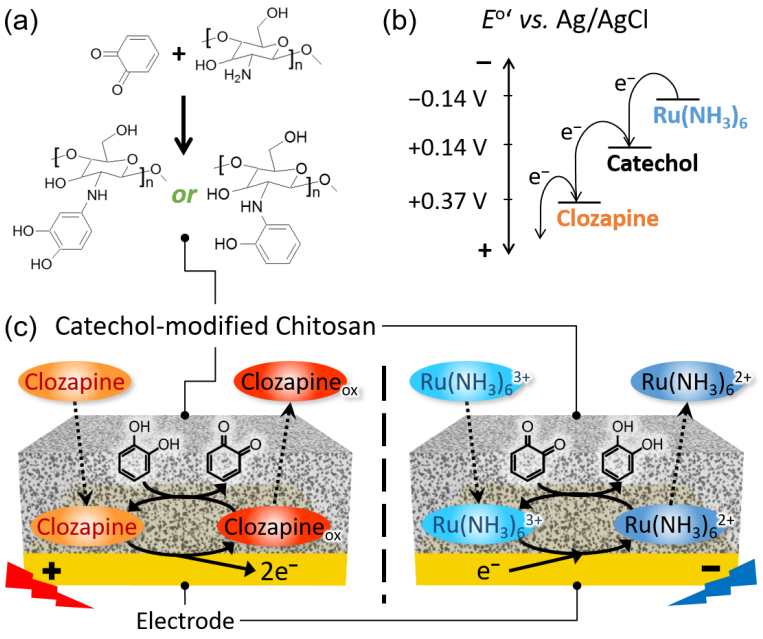


Figure 2.2: (a) Putative chemistry of catechol grafting to chitosan [86]. (b) Standard reduction potentials and overall electron transfer scheme for the major redox species discussed. (c) Schematic of the catechol-modified chitosan redox cycling system. The diffusing clozapine acts as an oxidizing mediator; the redox capacitor allows for a repeating cycle of clozapine reduction in the presence of reduced catechol, followed by clozapine re-oxidation at the anode (left; $E \geq 0.37$ V). Conversely, under negative potentials, Ru in solution acts as a reducing mediator, regenerating the oxidized catechol (right). Adapted with permission from [90].

continuous cycle of oxidation at the electrode, followed by reduction in the presence of catechol. Consequently, the total charge transfer generated by the available clozapine is increased, amplifying the measured electrochemical current and thus the signal. To recover the catechol to the reduced state, negative potential can be applied in the presence of a reducing mediator such as Ru.

Redox cycling is rather obviously expected to enhance sensitivity due to redox signal amplification. However, in complex biological fluids with many redox-active species, the redox cycling amplification approach could be expected to indiscriminately amplify everything, enhancing not only the clozapine signal but also the background noise. However, selectivity for clozapine in this system is intuitively three-fold. First, because the amplification relies on redox cycling, redox species that show irreversible

reduction or oxidation will contribute significantly less to the electrochemical signal. Only the signal from reversible or quasi-reversible species, such as clozapine, will be amplified. Second, based on the standard reduction potential of catechol, signal amplification is limited to species with $E^{o\prime} \gtrsim +0.15$ V. Those with lower $E^{o\prime}$ cannot participate in the redox cycling. Third, the chosen electrochemical technique allows for further discrimination. Voltammetry, where voltage is scanned continuously (or, depending on the specific technique, in a step-wise fashion) at a certain rate while recording current, allows for direct differentiation based on $E^{o\prime}$ – the signal will show a peak in current at that potential. In the following Subsections, I will be addressing both sensitivity and selectivity, as well as other aspects of this compound film to establish its suitability for point-of-care clozapine sensing.

### 2.1.1 Experimental Methods

For my research, I employ three-electrode electrochemical cells controlled by a CH Instruments 660D or Bio-logic VSP-300 potentiostat. The cells consist of a 1.5 ml volume sample reservoir with a platinum counter electrode and an Ag/AgCl (1 M KCl electrolyte) reference electrode immersed, as shown in Figure 2.3. As a working electrode, I generally utilize custom planar microfabricated gold electrodes, which are intended to provide a similar surface to later microsystem implementations. I fabricate the $7.5 \times 7.5$ mm$^2$ surface area electrodes utilizing standard photolithography processes on a silicon wafer. Specifically, I coat the wafer with 500 nm silicon oxide using plasma-enhanced chemical vapor deposition (PECVD) for electrical insulation. The subsequent metal coating, lithography, and wet etching are described in full in Subsection 3.1.3 (here, I use mask 6.1 in Appendix A: Photomasks). Before use, I dice the wafer and clean electrodes using Piranha (3:1 sulfuric acid : hydrogen peroxide).

For some fundamental studies on the molecular processes in the redox cycling system – requiring either deoxygenation of solutions, which is difficult to implement

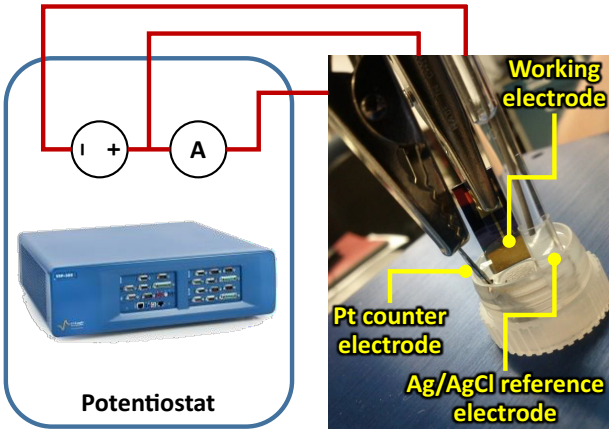


Figure 2.3: Schematic and photograph of typical three-electrode electrochemical cell setup.

utilizing the microfabricated electrodes, or large (> 50) numbers of independent experiments, which become prohibitively expensive and time-consuming using the single-use microfabricated electrodes – I instead employ commercial 2 mm gold disk electrodes. These electrodes are polished before each use with alumina powder according to manufacturer specifications.

I prepare a 1% w/w solution of chitosan by adding flakes to deionized (DI) water under constant stirring overnight, with the pH gradually adjusted to 5.5 by titrating 1 M hydrochloric acid. The solution is then filtered successively through a mesh filter and a porous glass filter to remove any undissolved chitosan. The final concentration is determined by weighing ~ 2 ml of solution before and after dehydration in an oven at 65 °C overnight, and adjusted to 1% by adding water if needed (the concentration is typically slightly above 1%). Catechol is prepared as a 5 mM solution in deionized water. Chitosan electrodeposition is achieved by applying a constant cathodic current of 6 A/m² for 45 s, followed by immersing the electrode in 0.1 M, pH 7 PB. Catechol is electrografted onto the films at a constant anodic potential of +0.6 V over 180 s, followed by rinsing in DI water.

Test solutions are generally based on 0.1 M phosphate buffer spiked with 25 µM Ru (reducing mediator), though some experiments were carried out with 1× phosphate

buffered saline (PBS) or commercial human serum. Commercial human serum is more readily and inexpensively available compared to clinical samples and is thus employed in the initial studies of this Section. I utilize every redox capacitor film at least twice – first a baseline measurement, followed by one in solution also containing the oxidizing mediator of interest, *i.e.* typically clozapine. At the very start of experiments, I find that a film initialization procedure (cyclic voltammetry in a test solution with 25 μM Fc) is helpful. The purpose of this is three-fold: First, it serves as an electrochemical cleaning step to oxidize any remaining entrapped ungrafted catechol. Second, it ensures a consistent charge state of the film prior to subsequent measurements. Third, it provides quality control – a working film will amplify the Fc signal.

The measurement method utilized, unless noted otherwise, is cyclic voltammetry. Operated here between −0.4 and +0.7 V at a scan rate of $\nu = 0.02$ V/s, this has the added advantage of allowing for repeated cycles of clozapine oxidation (at positive potentials) as well as catechol recharging by Ru (in the negative range). I run at least three cycles, with the third cycle – where the system typically reaches an equilibrium and signal amplification saturates – used for analysis, particularly in terms of peak current $I_\mathrm{p}$ and corresponding potential $E_\mathrm{p}$. It is worth here to consider the governing equations for these two parameters in traditional electrochemical systems, *i.e.* with bare, unmodified electrodes. The Randles–Sevcik equation describes the peak current as [88]:

$$I_\mathrm{p} = 0.4463ACFn\sqrt{\frac{Fn\nu D}{RT}} \tag{2.1}$$

Therein, $A$ is the electrode surface area, $C$ the concentration of the analyte, $D$ its diffusion constant, $n$ the number of electrons per reaction, $T$ the solution temperature, $F$ the Faraday constant, and $R$ the universal gas constant. The corresponding potential for this (here, oxidative) current peak is given by the Nernst equation at equilibrium [88]:

$$E_\mathrm{p} = E^{\circ\prime} + \frac{29.58}{n}\mathrm{mV} \tag{2.2}$$

Both equations assume an ideal, diffusion-limited, fully reversible redox couple, which is an assumption that does not apply to clozapine (as explored in more detail in Subsection 2.1.5). However, the equations can still serve as first-order approximations, and deviations can give insight into underlying processes.

### 2.1.2 Signal Amplification

The first figure of merit I consider is the signal amplification, calculated as:

$$\frac{\left(I_{\mathrm{p}}^{\mathrm{sample}} - I_{\mathrm{p}}^{\mathrm{background}}\right)_{\mathrm{modified\ electrode}}}{\left(I_{\mathrm{p}}^{\mathrm{sample}} - I_{\mathrm{p}}^{\mathrm{background}}\right)_{\mathrm{bare\ gold\ electrode}}} \tag{2.3}$$

That is, the background-subtracted peak current with a modified electrode (*e.g.* the redox cycling system) expressed relative to that observed with a bare electrode. The background-subtracted current in general is useful to better visualize the signal caused specifically by the analyte, and is employed in many of the following figures. The amplification ratio provides a simple though imperfect way to assess the gain in sensitivity for a given set of conditions. Only two or four measurements are required for assessing electrode modification or a set of electrochemical measurement parameters, respectively. However, this approach does not take into account variations over the clinically relevant concentration range needed to determine the true sensitivity as shown in Subsection 2.1.3.

My exemplary results in Figure 2.4 show that chitosan-catechol yields 3.64-fold signal amplification [91]. Compared to 0.91 for only catechol and 0.24 for only chitosan, this demonstrates significant bio-amplification through the redox cycling system. Without chitosan, the catechol cannot be efficiently immobilized in the vicinity of the electrode. This leads to the lack of amplification and increased signal interference from residual free catechol. Without catechol, I hypothesize that the lower mobility of clozapine in the chitosan compared to in solution, combined with the film's non-conductive nature, lead to the decreased faradaic currents. This is further explored in 2.1.5.

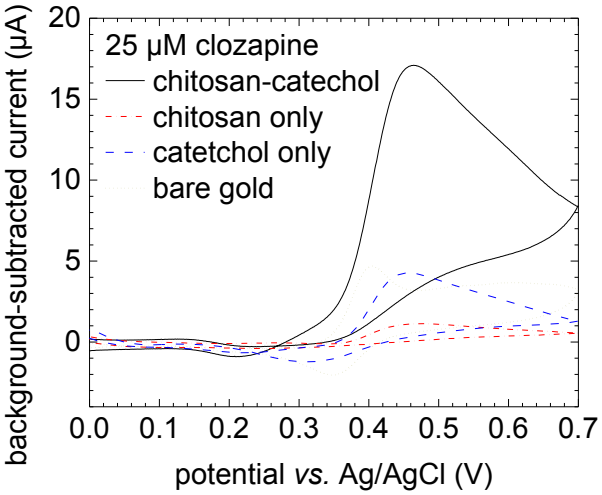


Figure 2.4: Signal amplification in the redox cycling system. Oxidative current (background-subtracted) measured in clozapine solutions using electrodes bare (black dash-dotted), chitosan-modified (dashed green), catechol-modified (dashed blue), or modified with the chitosan-catechol redox cycling system (solid red). Adapted with permission from [91].

Besides the film components, another factor in the amplification system is the reducing mediator. In Figure 2.5a I show results from an optimization study utilizing various concentrations of Ru [90]. Its utility is immediately apparent – the peak current $I_p$ reduces by up to 1.75 times in the absence of Ru, compared to its presence. The specific dependence of the signal amplification on the Ru concentration is intriguing in that it is non-monotonous. At 6.25 μM, Ru is significantly less abundant than the 25 μM clozapine. In this case, the oxidizing mediator is more efficient at discharging the catechol than the reducing mediator is at recovering it, resulting in sub-optimal amplification of the clozapine signal. At 25 μM, I record maximum amplification, the clozapine oxidation now no longer limited by insufficient recharging of the catechol. While intuitively an even higher concentration of Ru should not adversely affect redox cycling performance, I note a drop in amplification performance at 100 μM. I hypothesize this is due to the large concentration of Ru causing a very high background signal in the control measurements (Figure 2.5b), yielding smaller relative changes when introducing clozapine. Thus, while the reducing mediator is essential for sustained

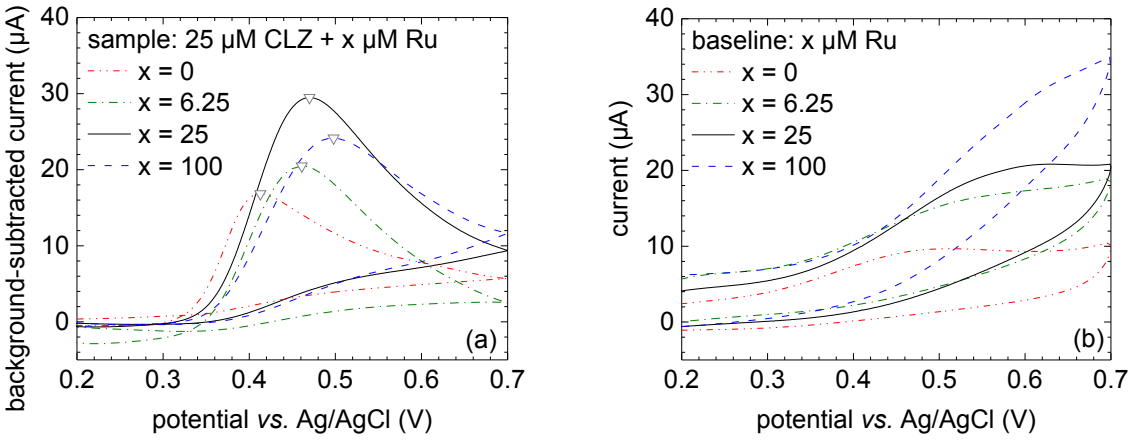


Figure 2.5: Impact of Ru on redox cycling performance. (a) Cyclic voltammograms (oxidative region shown; baseline subtracted) measured with the redox cycling system for solutions containing 25 µM clozapine and Ru at 0 µM (red dash dot dot), 6.25 µM (green dash dot), 25 µM (black solid) or 100 µM (blue dash). (b) Corresponding baseline measurements (*i.e.*, without clozapine). Both adapted with permission from [90].

clozapine signal amplification, its concentration needs to be chosen with the dynamic range of the application in mind. In addition to the changes in electrochemical current, I also observe a positive shift in peak potential $E_p$ by $391 \pm 15$ µV per µM of Ru ($R^2 = 0.998$), with an additional positive offset of $46 \pm 1$ mV likely from non-linear effects at lower concentrations than the ones investigated. Typically, shifts in peak potential speak to underlying changes in electron transfer kinetics, as explored further in Subsection 2.1.5. These are, however, unlikely to be affected for clozapine by the presence of Ru. Instead, the reducing mediator enables longer sustenance of the redox cycle – with time and potential inherently conflated by the very nature of voltammetry with its potential scan rate $v$, this results in a mainly temporal delay of the peak potential.

### 2.1.3 Sensitivity

While the signal amplification verifies the underlying principle of the approach, a sensor requires a dose-dependent response. To obtain a calibration curve, I measured test solutions of clozapine concentrations between 100 nM and 30 µM. This is chosen based on the clinically relevant range of 1–3 µM [13], plus or minus one order of magnitude.

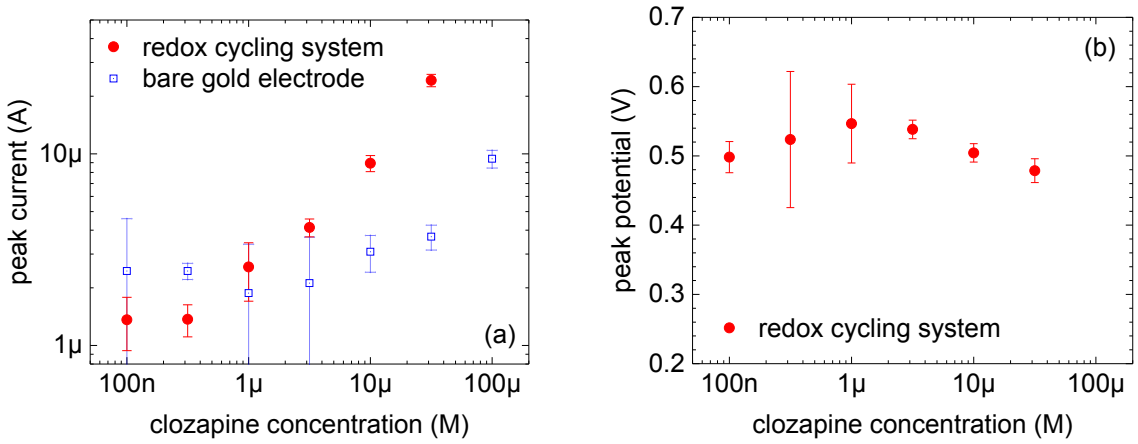


Figure 2.6: Clozapine sensing performance with the redox cycling system. (a) Clozapine detection in buffer solutions plotted in terms of background-subtracted peak current as a function of concentration for both unmodified (open blue squares) and redox cycling system-modified (solid red circles) electrodes. (b) The corresponding effect of the clozapine concentration on the oxidative peak potential. Both adapted with permission from [91].

Figure 2.6a presents such curves for clozapine detection in phosphate buffer with the redox cycling system as well as with a bare electrode for comparison [91]. In terms of figures of merit, I define sensitivity as the slope of the dose-response plot in the linear regime (as per the plot, on a log-log scale), with the detection limit as the intersection of that line with the constant background signal level, plus three standard deviations, loosely following [92]. Thus, for the chitosan-catechol electrodes, I obtain a sensitivity of 0.55 log A / log M and a detection limit of 0.95 µM. Critically, this detection limit is compatible with the clinically relevant range of 1–3 µM clozapine. While the very best existing electrochemical detection approaches reviewed in Subsection 1.3.2 can exceed this by up to an order of magnitude, their limitations need to be considered as well. For one, my study here is carried out in physiological buffer solutions where most of the reviewed techniques perform poorly. More importantly, however, all of these approaches focus exclusively on detection limit, ignoring many of the other important factors for a point-of-care sensing approach that I will explore throughout this Chapter.

For the bare electrodes, the high noise level at low concentrations makes

determination of both figures challenging. They can be estimated to be at least 2-fold lower in sensitivity and 30-fold higher in detection limit. This bears comparison with the approximately 3.6-fold amplification provided by the redox cycling system, implying that a large component of the system is not only amplification of the clozapine signal, but more importantly suppression of background noise. This is in line with the observations from chitosan-only electrodes, which showed a significant reduction in electrochemical signals earlier. Overall, these results highlight the significant promise of the chitosan-catechol system for clozapine detection.

Alongside the observed changes in $I_p$, I also find interesting behavior in the corresponding peak potentials $E_p$ in Figure 2.6b [91]. While the lowest-concentration values can be regarded simply as background noise according to the observations in $I_p$, there is a clear inversely proportional trend in peak potentials for clozapine concentrations $\geq 1$ µM. This may be attributed to the slow electron transfer kinetics of clozapine, further discussed in 2.1.5. At higher clozapine concentration, this can yield a relative excess of reduced clozapine near the electrode, lowering the observed potential as described by the Nernst equation outside equilibrium conditions [88].

### 2.1.4 Film Stability with Reuse and Storage

While sensitivity is critical, an eventual point-of-care sensor also needs to be robust. Testing reusability gives useful insights into film fouling mechanisms, and also helps evaluate the potential use of the biosensor as a continuous monitoring system. For this, I reuse individual films for 20 successive measurements, alternating between control and sample solutions prepared fresh with each iteration. The cyclic voltammograms in Figure 2.7a reveal a gradual decrease in peak current with reuse, combined with an increase in peak potential [90]. Both are highly linear at $-1.04 \pm 0.03$ µA (2.2% of the absolute signal; $R^2 = 0.992$) and $5.47 \pm 0.22$ mV (1.2%; $R^2 = 0.988$) per reuse. As also seen in the plot, the baseline signals from the control solutions decrease in a similar

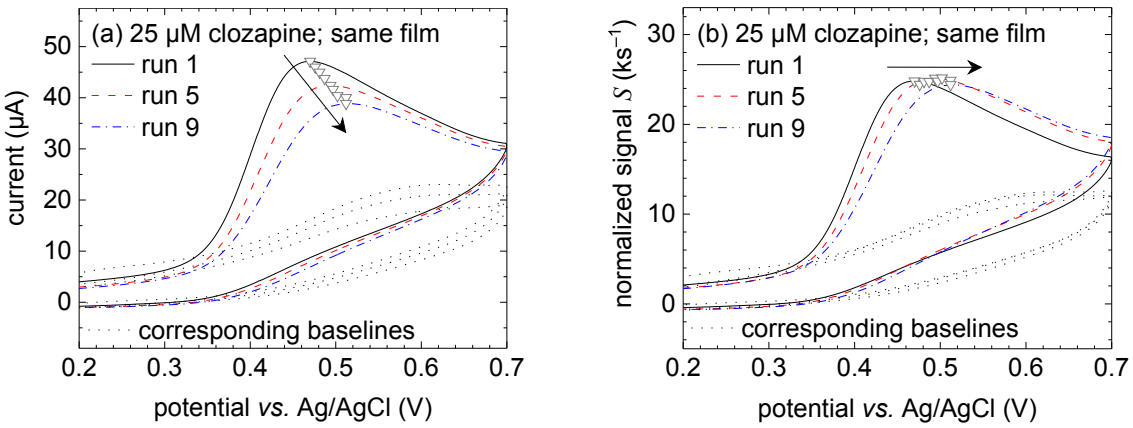


Figure 2.7: Reusability of the redox cycling system. (a) Selected cyclic voltammograms (lines; oxidative region shown) and signal peaks (gray triangles) for 25 µM clozapine samples measured with the same chitosan-catechol electrode. Corresponding baseline measurements are included (black dots). The arrows indicate the progression of measurement runs. (b) Normalization of the same data with respect to immediately preceding baseline measurements. Both adapted with permission from [90].

fashion. The concurrent decrease of both clozapine peak current and baseline current suggests gradual degradation of the film from repeated use and/or the associated wash steps. If clozapine fouling of the film were responsible, both sample and baseline signals would instead be expected to increase, with clozapine from previous solutions adding to the measured signals. The observed increase in the required overpotential is also consistent with film degradation. Specifically, it implies a slowing-down of the redox cycling kinetics, which could be due to gradual loss of catechol with reuse, thereby leading to longer mean diffusion times of the clozapine between the electrode and the catechol.

Interestingly, the film degradation mechanism provides a means to adjust for the observed signal loss independently of the actual sample measurements. Specifically, I calculate the total baseline charge transfer $Q = \int I^{\text{background}} \, \mathrm{d}V$ from the respective control solutions to quantify the degradation, and divide the measured clozapine current $I$ by this value to derive a normalized signal $S = I/Q$. This is plotted in Figure 2.7b, showing that the peak signals remain constant with film reuse at $24.8 \pm 0.7$ ks$^{-1}$.

While biofabrication enables our unique sensor functionality, the biomaterials are

inherently more fragile than solid-state components. Therefore, toward suitability for point-of-care application, I seek to understand the material degradation of the redox cycling system with reuse as well as with storage. Without a shelf life, the chitosan-catechol modification in a real-world lab-on-a-chip would need to happen on-site, adding complexity and variability to the device. Storage lifetime is evaluated by fabricating redox cycling films and immediately transferring them to either air or buffer solution for extended periods of time. At intervals up to 77 days, films are removed from storage and assessed in terms of signal amplification. Based on the results with reuse, I visualize the storage data in a similarly normalized fashion in Figure 2.8, in comparison to data from as-fabricated films (solid black lines) [90]. This reveals a consistent 57.5 ± 3.0% loss in peak signals from storage in air independent of storage duration (representative time points shown with red dashed and blue dash-dotted lines). I attribute this to an irreversible collapse of the hydrogel matrix upon prolonged exposure to air, wherein re-hydration fails to recover the typical loose polymer network structure. A collapsed hydrogel with a denser polymer network would lead to slower diffusion of clozapine, in line with the significantly lower currents observed. While quantitative measurements of the film thickness were not possible in its hydrated state, this was qualitatively confirmed by visual inspection of the films.

For storage in solution, the mechanism is shown to be quite distinct, with the measured clozapine signals gradually decreasing by 0.255 ± 0.072% per day ($R^2 = 0.64$) over the first 1.5 months before saturating. This is accompanied by an increase in peak potential reminiscent of what was observed with film reuse. These symptoms imply a similar film degradation mechanism at work, yet more pronounced due to the inability to adjust for it solely by considering the background signals. Other factors potentially affecting degradation (oxygen, temperature, light) were similar for both in-air and in-solution storage, thus are not thought to play a role in the observed differences. The results suggest that solution storage is advantageous over short times due to the low

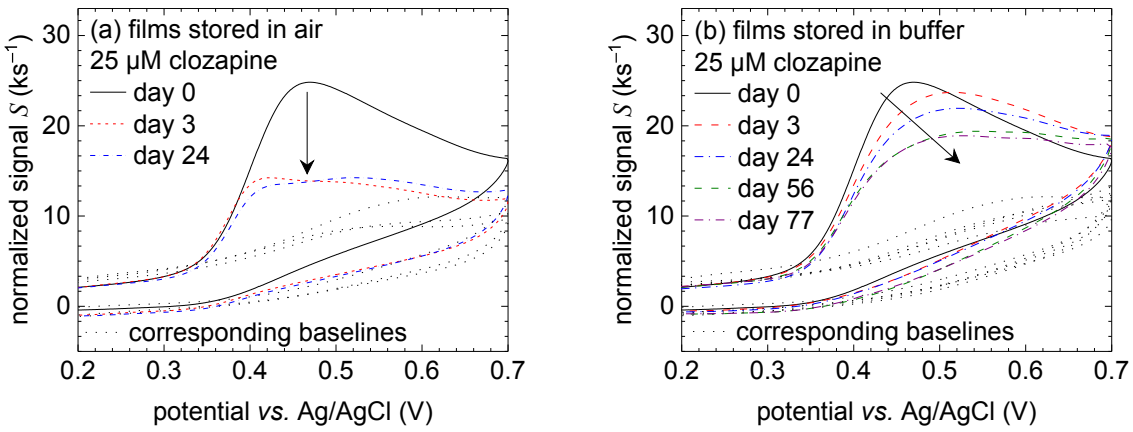


Figure 2.8: Storage of the redox cycling system. Normalized cyclic voltammograms (oxidative region shown) for solutions containing 25 µM clozapine measured with redox cycling system electrodes immediately after biofabrication (black solid) and for representative timepoints after storage in air (a) or buffer solution (b). Corresponding baseline measurements are included (black dots). The arrows highlight the impact of storage on the clozapine signal. Both adapted with permission from [90].

associated signal loss; at longer timescales, however, air storage appears beneficial due to the practically constant (albeit lower) performance over time.

### 2.1.5 Diffusion and Redox Kinetics

Diffusion and electron transfer kinetics have been alluded to in a number of places within this Section to explain certain behavior observed in the redox cycling system. They can also help in understanding and even enhancing selectivity of the system. My goal is thus to systematically study and gain a deeper understanding of the interplay between chitosan morphology, catechol grafting, and clozapine detection. This can be investigated with the same techniques utilized for sensing, recalling the two equations governing cyclic voltammetry from Subsection 2.1.1. In the Randles–Sevcik Equation 2.1, the measured peak current $I_p$ is related to the diffusion coefficient $D$. The latter can thus be extracted from measurements, more accurately so when conducted at various scan rates $v$ (another parameter in the equation). While the relation is derived for reversible redox couples, it can also serve as a first-order approximation for quasi-reversible ones.

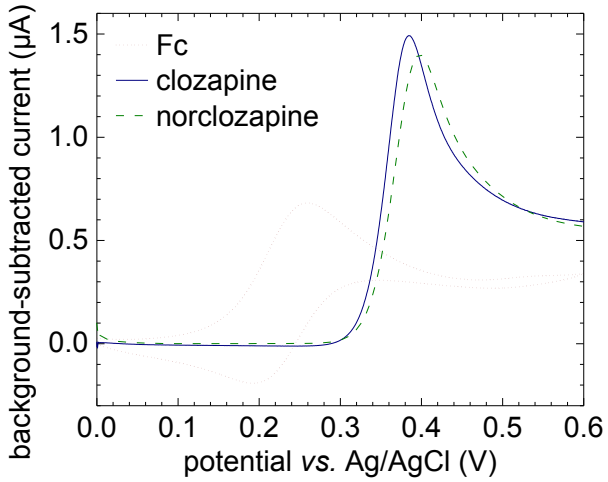


Figure 2.9: Cyclic voltammograms (background-subtracted) of Fc (red dotted), clozapine (blue solid), and norclozapine (green dashed) in buffer solution. Only the oxidative scan direction is shown for the latter two for clarity. Adapted from [93].

In the Nernst Equation 2.2, the oxidative peak potential $E_p$ is given for ideal redox species as 29.6 mV (or 14.8 mV, for an $n = 2$ electron reaction) above the standard reduction potential $E^{o\prime}$. Slow (or not fully reversible) redox species will show an increase in this separation particularly at high scan rates, when the electron transfer rate (rather than diffusion) becomes a limiting factor. The redox kinetics of a given analyte can thus be inferred by tracking $E_p - E^{o\prime}$.

As a known control to validate the general approach, I utilize the well-described fully reversible redox mediator Fc ($E^{o\prime} = +0.23$ V), known to be suitable for redox cycling [86]. I compare this with clozapine for three conditions: Bare electrodes to establish a baseline, chitosan-catechol, and chitosan only to differentiate chitosan matrix effects from those of the full redox cycling system. Additionally, I compare clozapine to its metabolite norclozapine – structurally similar and also known to be redox-active [31] – under the same conditions to investigate selectivity. Representative cyclic voltammograms with 2 mm diameter bare gold electrodes are shown in Figure 2.9, highlighting the ideal nature of Fc as well as the practically indistinguishable nature of clozapine and norclozapine signals [93].

In Table 2.1 I lay out diffusion parameters for all three redox species [93]. While a literature value is available for Fc, this is not the case for clozapine and norclozapine. Thus, I derive diffusion approximations from a modified version of the Stokes–Einstein equation:

$$D = \frac{k_\mathrm{B}T}{3\mu}\sqrt[3]{\frac{1}{6\pi V}} \tag{2.4}$$

Therein, $k_\mathrm{B}$ is the Boltzmann constant and $\mu$ the viscosity of the medium. The equation is typically expressed as a function of the molecular radius. However, as becomes obvious from the molecular structures in Figure 1.3, both clozapine and norclozapine are distinctly non-spherical. Therefore I instead rely on the van der Waals volume $V$ – determined from molecular dynamics simulations [94] – to derive the respective expected diffusion coefficients in the table. By conducting cyclic voltammetry for scan rates from $\nu = 1$ mV/s to 10 V/s, I determine the experimental diffusion coefficients also listed in the table from a linear fit of the measured peak currents $I_\mathrm{p}$ to the Randles–Sevcik Equation 2.1. For the control mediator Fc, the experimental result agrees reasonably well with the literature value, considering that my system is not necessarily optimized for the highest-accuracy diffusion coefficient determination, and that the exact value can depend on the ionic strength of the buffer. For both clozapine and norclozapine, however, I observe a much more significant two-fold difference between theory and experiments. As the Stokes–Einstein diffusion calculation is quite accurate for Fc with respect to the literature value, this approximation is insufficient to explain such a discrepancy. One aspect may be electrophoretic effects, where negative charge on the electrode at low potentials may attract the (at neutral pH) predominately positively charged clozapine and norclozapine. Their respective net charge properties, as a function of pH, are illustrated in Figure 2.10. This would also be in line with the larger discrepancy observed for norclozapine, which is even more positively charged compared to clozapine at neutral pH. The electrophoretic transport hypothesis is further explored in separate experiments described at the end of this Subsection. Another aspect in the observed diffusion coefficient discrepancy

| Analyte | Diffusion coefficient | | |
|---|---|---|---|
| | literature | Stokes–Einstein Eq. 2.4 | experimental |
| Fc | 7.5 µSt [95] | 7.6 µSt | 8.2 ± 0.2 µSt |
| clozapine | — | 5.3 µSt | 8.9 ± 0.3 µSt |
| norclozapine | — | 5.4 µSt | 11 ± 1 µSt |

Table 2.1: Expected and experimental diffusion behavior of the three analytes. The Stokes–Einstein calculations and experimental measurements are described in the text. Adapted from [93].

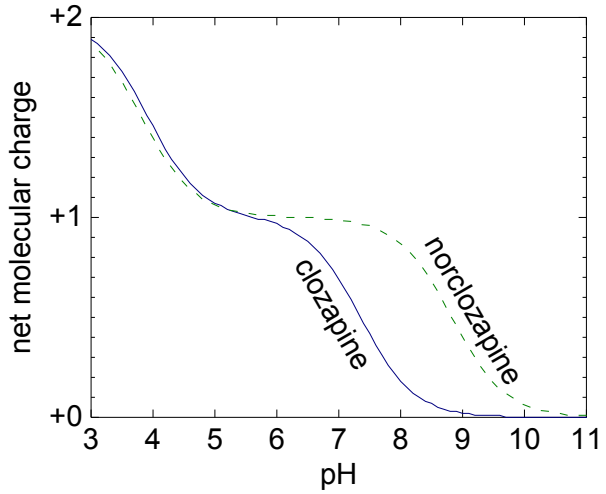


Figure 2.10: Net molecular charge of clozapine (blue solid) and norclozapine (green dashed) as a function of pH, highlighting the different charge states at neutral pH [94]. Adapted from [93].

may be, to reiterate, the non-ideal redox nature of both molecules, which renders the Randles–Sevcik equation only an approximation.

In the presence of chitosan, calculating the diffusion coefficient at each scan rate from the measured peak current becomes insightful, shown in Figure 2.11a [93]. Two regimes become apparent for all species. At low scan rates, diffusion coefficients approach those observed with a bare electrode (gray area). At high scan rates, diffusion coefficients drop – significantly so for clozapine and norclozapine – before saturating. This is broadly in line with expectations: At low scan rates, the depletion layer will extend significantly beyond the thin chitosan film, therefore leading to dominance of bulk diffusion in solution as with a bare electrode. At high scan rates, the depletion layer will be fully contained

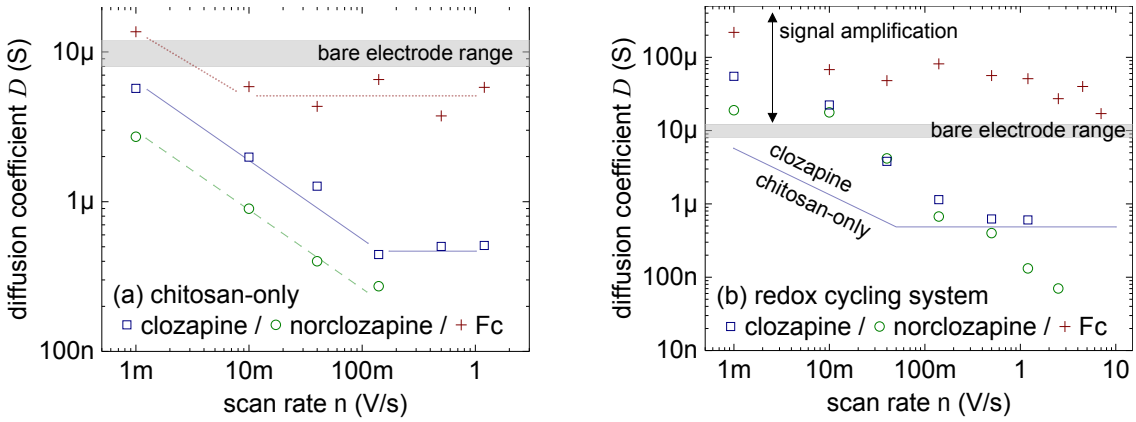


Figure 2.11: Calculated diffusion coefficients $D$ as a function of cyclic voltammetry scan rate for clozapine (blue squares), norclozapine (green circles), and Fc (red crosses) with chitosan-only electrodes (a; lines are for visual guidance only) or the redox cycling system (b; blue line indicates clozapine chitosan-only data). The bare electrode regime for all three species (*cf.* Table 2.1) is represented as a shaded gray area in both plots. Adapted from [93].

within the chitosan film, which restricts diffusion compared to free solution. The smaller Fc is significantly less restricted compared to both other species. However, the orders-of-magnitude difference, especially in light of the reversed trend on bare electrodes, could also point to clozapine-specific interactions with the chitosan. A likely candidate is electrostatic interactions of the largely positively charged clozapine with the similarly positively charged chitosan matrix. One aspect not necessarily expected *ab initio* is the consistently 2-fold lower diffusion of norclozapine compared to clozapine – both molecules are practically the same size (*cf.* calculated diffusion coefficients in Table 2.1), and were observed to have very similar diffusion behavior on bare electrodes. The trend is in line, however, with the charge repulsion hypothesis, since norclozapine is even more positively charged compared to clozapine at neutral pH as seen in Figure 2.10, and would thus be more strongly restricted within the chitosan matrix. This chitosan-based selectivity is remarkable, considering the identical electrochemical characteristics of both species with bare electrodes.

With the chitosan-catechol system, diffusion determination is not as straightforward. Due to redox cycling, underlying assumptions of the Randles–Sevcik Equation 2.1

break down as multiple diffusion lengths and rates (in bulk solution, within the film, and between the electrode and the catechol) and redox reactions (at the electrode and with the catechol) become relevant. Thus, apparent diffusion coefficients calculated based on the equation will mostly reflect signal amplification in the system. Indeed, Figure 2.11b shows all species with higher apparent $D$ compared to their chitosan-only values, indicating the expected signal amplification [93]. While the signal for Fc is amplified above even its bare electrode values for all scan rates, clozapine and norclozapine show this behavior only at the lowest scan rates investigated. Critically, clozapine amplification is shown to be higher than for norclozapine, further emphasizing emergent selectivity due to electrode biomaterial modifications. The reasons for this can in part be attributed to the differing diffusion behavior observed in chitosan, as well as to the differing electron transfer kinetics considered below. At high scan rates, the observed $D$ for clozapine again saturates at the same value as when there is only chitosan on the electrode. In this regime, the electron transfer kinetics are too slow to allow for more than a single reaction, thus again reflecting true diffusion, which is apparently not altered by the presence of catechol in the film.

Looking next at electron transfer kinetics, the theoretical behavior for all species is summarized in Table 2.2 [93]. Fc, with its ideal single-electron reaction should show a peak potential in line with the at-equilibrium Nernst Equation 2.2. Both clozapine and norclozapine feature two-electron redox reactions, but are expected to deviate strongly from the tabulated Nernstian behavior due to slow and quasi-reversible kinetics. Fc indeed closely follows theoretical expectations for an ideal single-electron redox mediator on a bare electrode as seen in Figure 2.12. Its oxidative peak potential deviates from the expected $E_p = +0.26$ V only at very high scan rates $\nu \geq 1$ V/s, highlighting the fast electron transfer kinetics. Both clozapine and norclozapine, conversely, rapidly diverge from the expected $E_p = +0.39$ V for scan rates above 10 mV/s, indicating significantly slower reaction kinetics. Interestingly, this trend is highly similar for both species, with a

| Analyte | Electron transfer | | | |
|---|---|---|---|---|
| | $E^{o\prime}$ | $n$ | $(E_p - E^{o\prime})_{ideal}$ | $E_p$ |
| Fc | 0.23 V | 1 | 29.6 mV | 0.26 V |
| clozapine | 0.37 V | 2 | 14.8 mV | 0.39 V |
| norclozapine | 0.37 V | 2 | 14.8 mV | 0.39 V |

Table 2.2: Electron transfer parameters for the three analytes. The calculations are based on the assumption of ideal Nernstian behavior as described in the text. Adapted from [93].

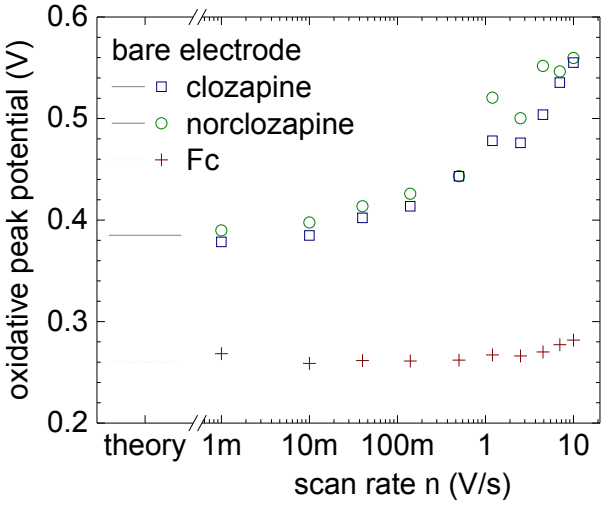


Figure 2.12: Observed oxidative peak potentials as a function of cyclic voltammetry scan rate for clozapine (blue squares), norclozapine (green circles), and Fc (red crosses) with bare electrodes. The theoretical ideal values for all three species (*cf.* Table 2.2) are indicated by lines to the left of the data. Adapted from [93].

correlation of $R^2 = 0.99$. Thus, while diffusion differs slightly between these two species, the remaining similarities practically prevent differential determination of the two species with a gold electrode.

In the presence of chitosan, as shown in Figure 2.13a, only minimal changes are observed for Fc and clozapine *versus* their respective bare electrode results [93]. For the latter, this can be quantified with a correlation of $R^2 = 0.99$; since Fc yields a flat line in both cases, correlation cannot be applied. More interesting is the case of norclozapine, which shows a drastic change toward a nearly constant oxidation peak potential 0.1 V above its $E^{o\prime}$. Similar to its effect on diffusion, chitosan appears to confer selectivity between the two highly similar species to the system. A simple two-process view of

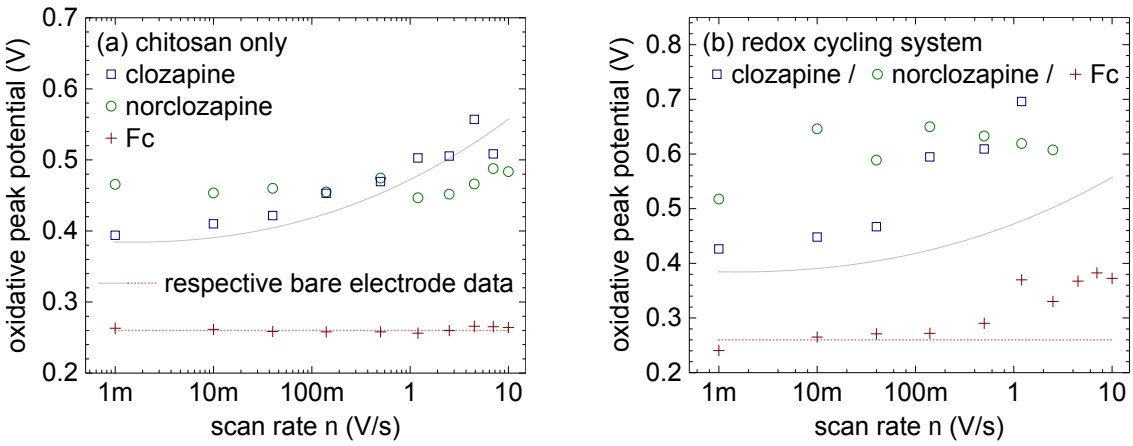


Figure 2.13: Observed oxidative peak potentials as a function of cyclic voltammetry scan rate for clozapine (blue squares), norclozapine (green circles), and Fc (red crosses) with electrodes modified with chitosan-only electrodes (a) or the redox cycling system (b; dotted red line indicates Fc bare electrode data). Clozapine and norclozapine bare electrode data is represented as a gray line in both graphs. Adapted from [93].

the electrochemical reaction (diffusion to the electrode, followed by electron transfer) is insufficient to explain such behavior, as the presence of chitosan on the surface should not change the inherent reaction kinetics between norclozapine and gold. A three-process picture more closely aligned with reality, however, can offer more insight: Between diffusing to the electrode and reacting with it, the redox species needs to adsorb to the electrode surface, and subsequently desorb again. I hypothesize that the reaction constant for this adsorption process changes for the case of norclozapine, and actually begins dominating the overall kinetics. I posit that the underlying factor in play here is the strong electrostatic repulsion between norclozapine and chitosan, which would hinder adsorption more strongly than for clozapine (where the electron transfer reaction remains the dominant factor).

For the chitosan-catechol redox cycling system, the complexity of the electron transfer system increases to not only include the oxidation at the electrode, but also the reduction facilitated by catechol (separated by a short diffusion path from the electrode) with its separate reaction rate. The electrochemical results in Figure 2.13b reflect this in a slowdown of electron transfer kinetics across the board, wherein the diffusion between

the electrode and the catechol likely becomes a limiting factor with Fc, which similarly slows down clozapine [93]. Norclozapine still exhibits generally constant oxidative peak potential (albeit with high variability), now at an even higher $E_p = 0.61$ V, likely also reflecting the aforementioned added reaction steps occurring in the system. Importantly, however, this breaks the symmetry between clozapine and norclozapine even further than chitosan alone. Indeed, at low scan rates $\nu < 100$ mV/s, the high similarity between both species in diffusion and reaction kinetics is broken for both factors. Thus, the chitosan-catechol film can enable selective detection of both clozapine and norclozapine *via* electrochemical methods, a feat not previously demonstrated using electrochemical detection. This selectivity applies especially when investigating a range of scan rates, where both species exhibit quite distinctive changes in behavior.

To further investigate the hypothesis of electrostatic effects for clozapine, I consider variations on the typical redox cycle for the redox cycling system, bare electrodes, and chitosan only. In the absence of Ru, omission of the negative potential would not be expected to affect electrochemical signals in the positive potential range – the negative potential only serves to reduce Ru to enable catechol regeneration in the film. However, comparing the current signals in Figure 2.14b corresponding to the voltage sweeps in (a) highlights critical differences [90]. In the absence of Ru, omission of the negative scan potentials causes a significant $\sim$ 2.5-fold decrease in the clozapine redox signal. The signal can be recovered, however, by applying a short negative potential pulse. This aligns with the previous hypothesis of electrostatic effects. Specifically, I believe that electrophoretic transport of the predominantly positively charged clozapine (*cf.* Figure 2.10) to the electrode increases the locally available concentration. Although the high ionic strength of the buffer leads to charge screening and thus a decrease in mobility, the latter can be calculated to retain half its magnitude [96,97]. Electrophoretic effects are further supported by some capillary electrophoresis studies operating in a similar range of ionic strength and pH [32,33].

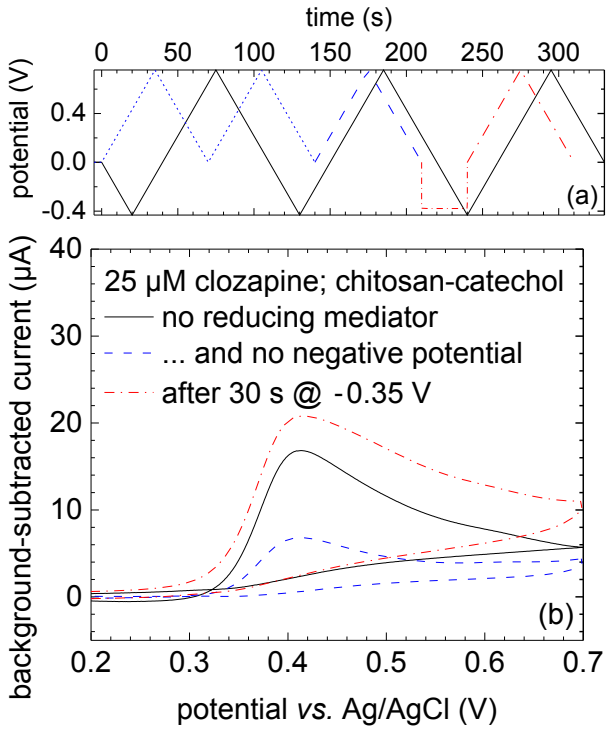


Figure 2.14: Impact of applied negative potential on amplification. (a) Schematic of potential sweeps utilized in these experiments: Standard full voltammetry cycle (black solid); omission of negative potential range (blue dash); application of negative potential pulse (red dash dot). The current measurements corresponding to the bold sections are plotted in (b) for the redox cycling system. Reproduced with permission from [90].

A compounding factor may be the presence of oxygen, which is reduced around −0.2 V, a pronounced reaction that is omitted in the absence of negative potentials. To consider this, I carry out further experiments in an oxygen-deprived environment. The test solutions are bubbled with nitrogen gas prior to measurements, and nitrogen is flown across the solution surface during the measurements. These experiments necessitated the use of commercial gold disc electrodes to better seal the measurement chamber, thus current magnitudes are not comparable to the earlier results. However, with bare electrodes, a less pronounced yet similar trend is apparent in Figure 2.15a: The clozapine signal current decreases by 26% when omitting negative potentials from the scan, and recovers with a negative potential pulse. The behavior is amplified in the presence of a chitosan film only, as seen in (b) [90]. Thus, I believe that diffusion dominates over

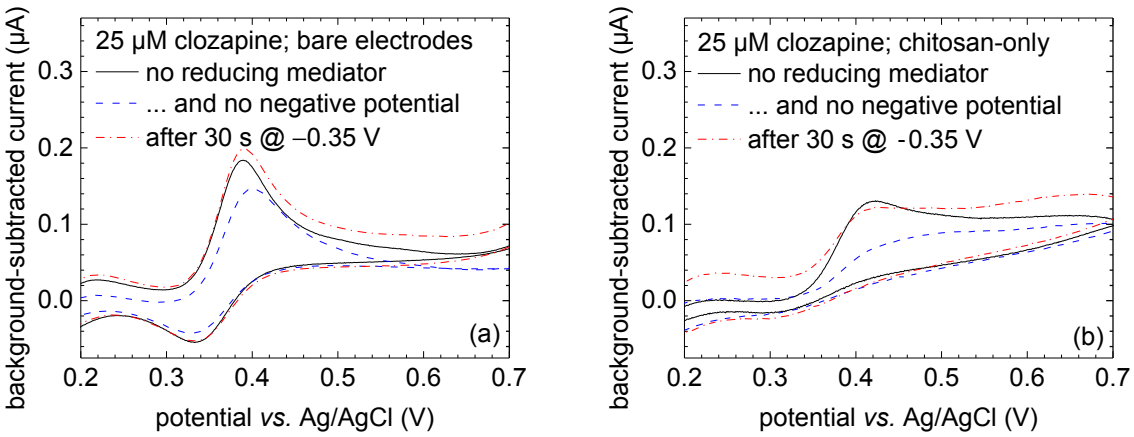


Figure 2.15: Impact of applied negative potential on amplification, continued from Figure 2.14, showing electrostatically driven transport of clozapine for bare (a) and chitosan-only-modified electrodes (b). Adapted with permission from [90].

electrophoretic transport with bare electrodes, but plays a significant role in the presence of the diffusion-restricting chitosan film, which can be further amplified when catechol is also present. This electrophoretic transport may serve to explain pre-concentration effects observed, but not further investigated, by other electrochemical studies of clozapine [40–42,98]. Signal gains in those works were up to an order of magnitude higher compared to this work, but that is likely due to the different nature of the electrode material – the carbon-based electrodes utilized therein have stronger inherent interactions with clozapine due to pi-pi interactions, likely enhancing the electrophoretic pre-concentration much like the redox cycling film does.

### 2.1.6 Serum Selectivity

The significant gain in clozapine sensitivity with the redox cycling system in buffer solutions was illustrated in Subsection 2.1.3, and in the previous Subsection I demonstrate that the biomaterial films confer selectivity between clozapine and its metabolite norclozapine. The situation is of course significantly more complicated when transitioning from buffer samples to human serum, where thousands of other species are present. Some of these species could interfere with the sensor through various

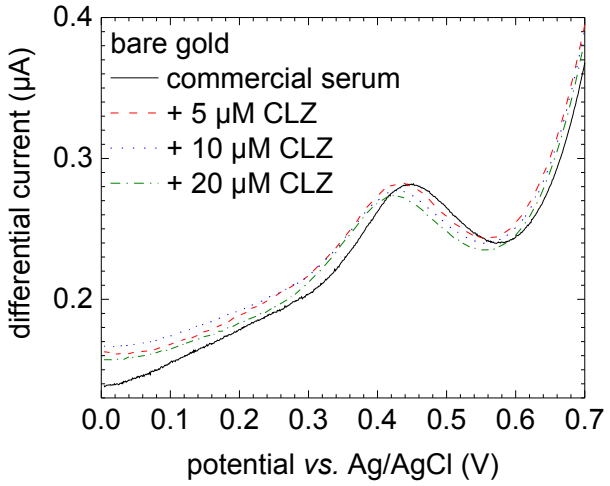


Figure 2.16: Clozapine detection in spiked commercial human serum samples using differential pulse voltammetry using a bare gold electrode. Adapted with permission from [99].

mechanisms, from redox activity of their own, or fouling of the electrode surface, to direct reactions of the interferents with the clozapine in solution. Broadly, there are two approaches to study this: Bottom-up, by analyzing the effects of individual potential interfering species (such as previously norclozapine) in buffer solution mixed with clozapine, or top-down by looking at human serum mixed with clozapine directly; in my work, I have employed both.

First, a simple electrochemical measurement of clozapine in commercial human serum with a bare gold electrode is instructive. These are conducted utilizing 2 mm disk electrodes and differential pulse voltammetry – the potential is not swept continuously, but instead in an oscillating step-wise fashion – which can be more sensitive than cyclic voltammetry, as discussed further in Section 2.3 (but is less suitable for the redox cycling system). As observed in Figure 2.17, serum exhibits a pronounced electrochemical background peak around 0.4 V, which coincides with the typical clozapine oxidation potential [99]. The additional signal of added clozapine does not become clearly apparent even at the highest concentration of 20 µM shown here.

Continuing the top-down approach with the chitosan-catechol system in Fig-

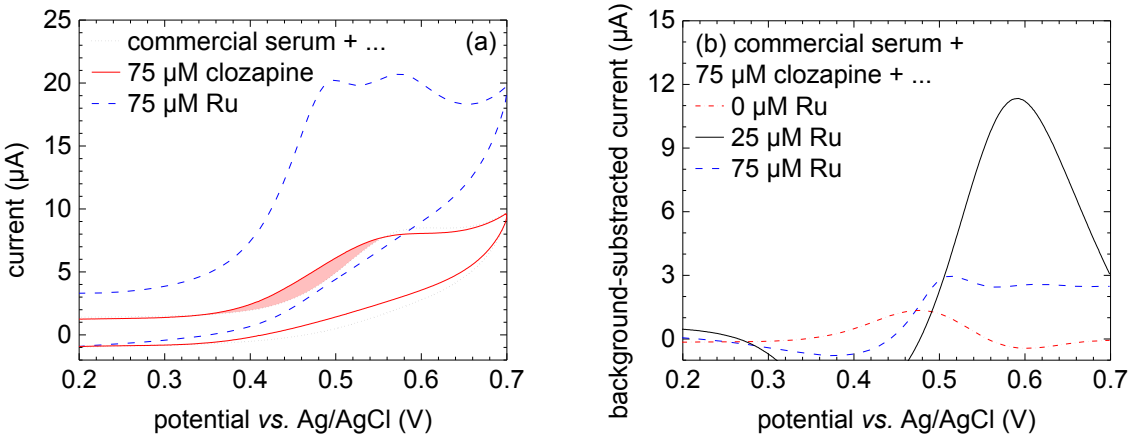


Figure 2.17: Clozapine detection in commercial human serum with the redox cycling system. (a) Cyclic voltammograms (oxidative region shown) for serum background (dotted black) plus either 75 μM Ru (dashed yellow) or 75 μM clozapine (solid red; difference *vs.* background shaded). (b) Cyclic voltammograms (background-subtracted; oxidative scan direction only) for 75 μM clozapine in serum at various concentrations of Ru.

ure 2.17a, I observe similarly pronounced serum background signals, shifted to higher potentials compared to bare gold. The significant increase in background signals in the presence of Ru indicates redox cycling of serum interferents. Adding a high concentration of clozapine to the solution causes a comparably minor increase in the observed current (in the absence of Ru). Looking at background-subtracted currents for clearer visualization of the clozapine signal in Figure 2.17b, the clozapine-specific current is revealed to increase in the additional presence of Ru. The trend is however non-monotonous – the highest concentration of Ru (matching that of clozapine) only serves to depress the clozapine signal compared to the case of 25 μM Ru. This bears comparison to earlier observations in Subsection 2.1.2, where matched concentrations provided the best signal-to-noise ratio. I hypothesize that this is due the to significant protein binding of clozapine as discussed in Subsection 1.3.1. With only a small fraction of the 75 μM clozapine free in solution (and electrochemically active as laid out later in this Section), it is actually the lower Ru concentration that more closely corresponds to the "matched" concentration condition. The general requirement for Ru in solution observed here defeats the *ab initio* hypothesis that serum's intrinsic reducing mediators might be sufficient for sustained redox cycling.

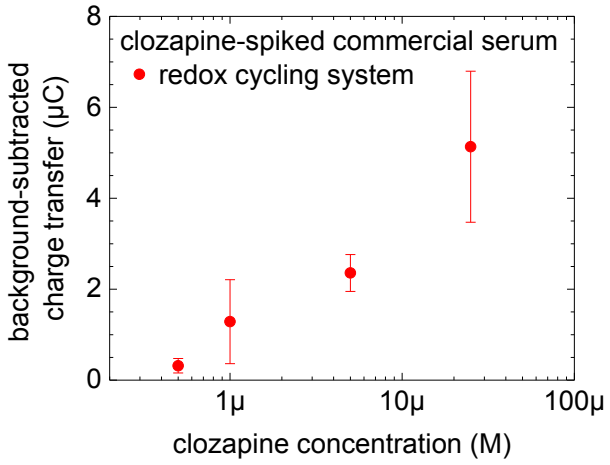


Figure 2.18: Clozapine sensing performance in spiked commercial human serum with the redox cycling system in terms of background-subtracted charge transfer from chronocoulometry for a range of clozapine concentrations. Adapted with permission from [91].

As the clozapine-specific peak can be ill-defined at lower concentrations in serum (somewhat akin to what is observed in the absence of Ru), I instead employ chronocoulometry to produce the calibration plot in Figure 2.18. For this technique, I apply a constant potential −0.4 V to (re-)charge the catechol, and then measure the total oxidative charge transfer over 60 s at an applied potential of +0.6 V. From the previous plot, this potential clearly aligns with the observed clozapine peak current. Due to the integrative nature of this method, it offers higher sensitivity at the expense of some selectivity in terms of the potential. The result is a sensitivity of 2.17 μC/log M and a detection limit of 0.59 μM, comparable to that achieved in buffer using cyclic voltammetry (in serum, cyclic voltammetry yields a detection limit at least 20 times higher). This represents the very first example of a sensor capable of measuring clozapine at clinically relevant levels directly in serum samples, in stark contrast to the previous examples in literature involving extensive pre-treatment as reviewed in Subsection 1.3.2.

The bottom-up approach now becomes useful toward attributing electrochemically influential elements of the serum background to individual interfering species. For an extensive study of the most common and abundant endogenous interferents in mixtures

with clozapine in buffer solutions, conducted with a glassy carbon electrode (shown to be inherently more sensitive to clozapine, but unsuitable for chitosan film deposition due to its inability to hydrolyze water), I refer to my colleague Sheryl Chocron's extensive work and resulting Master's thesis [100]. She determined uric acid ($E^{o\prime} = +0.28$ V [101]) to be the primary electrochemical interferent, responsible for the background signal in human serum at its native concentration of up to 410 μM. It is worth noting that uric acid requires significant overpotentials for oxidation on either gold or glassy carbon electrodes, explaining its interference with the clozapine signal (with a theoretically 0.1 V higher $E^{o\prime}$) as observed *e.g.* in Figure 2.16. Cysteine and serum albumin also exhibited interference, but with distinct mechanisms – a complex alteration of the current response, and a simple inhibition of clozapine's redox current, respectively. The latter is not surprising, and likely accounts for the decreased sensitivity observed in serum with the bare electrode (in buffer, 25 μM is easily detected on such). As mentioned in Subsection 1.3.1, clozapine is highly protein-bound in circulation, mostly to AAG and albumin. A separate study by my colleague George Banis further investigated the protein-binding in a bottom-up study, and found that 1) protein-bound clozapine possesses negligible electrochemical activity, and 2) while protein binding accounts for most of the signal loss, and fouling was shown to not be a significant issue (at least for a carbon electrode), the presence of serum-level amounts of protein inherently decreases all redox signals, likely due to crowding-type interactions [102]. While the latter presents a challenge for electrochemical sensors regarding serum measurements in general, the former provides an advantage over most of the other transduction methods reviewed in Subsection 1.3.2. Those generally measure the total concentration of clozapine in circulation, including the protein-bound fraction. Our approach, however, is sensitive only to the therapeutically active free clozapine, potentially providing better treatment monitoring [103].

Returning to the chitosan-catechol system, I consider some specific relevant interfering species in Figure 2.19. Previously discussed in depth in Subsection 2.1.5,

clozapine's metabolite norclozapine is one such candidate. While it is virtually indistinguishable from clozapine when utilizing a bare electrode, the biomaterial modifications enable differentiation. An interferent potentially more specific to the chitosan-catechol system is dopamine – although only present at nanomolar concentrations in blood, it serves as a representative catecholamine that may exhibit structure-specific interactions with the catechol-based redox capacitor. Dopamine produces a pronounced signal peak around +0.2 V, very near its standard reduction potential and far removed from the clozapine peak. The higher peak current compared to the other species is likely due to its faster diffusion and electron transfer kinetics, and thus higher redox cycling efficiency. Importantly, the baseline measurement remains unchanged after the dopamine measurement, indicating that no significant dopamine grafting onto the chitosan occurs. The catechol appears to occupy a near-equilibrium of available sites, which – combined with the short residence time of oxidized dopamine – limit such film adulteration. Next, acetaminophen is one of the most likely exogenous interferents present in patient samples, being present in a wide range of over-the-counter and prescription medications to reduce fever and/or relieve pain. This molecule shows a redox peak at or above the +0.75 V limit of the cyclic voltammetry scan shown here, with similar signal amplification to clozapine or norclozapine, but well removed from both their reaction potentials. These results illustrate the capability of the redox cycling system to differentiate certain endogenous and exogenous redox-active species. Finally, uric acid – the dominant interferent in serum – shows electrochemical signals significantly lower than that of clozapine, implying less efficient redox cycling. However, its peak potential still matches that of clozapine with the redox cycling system, aligning with the serum background signal observed previously. As mentioned earlier, uric acid is also typically present at a 100-fold higher concentration than clozapine. This presents a challenge for the redox cycling system, since high variability in uric acid can thus translate into still significant variability in clozapine measurements.

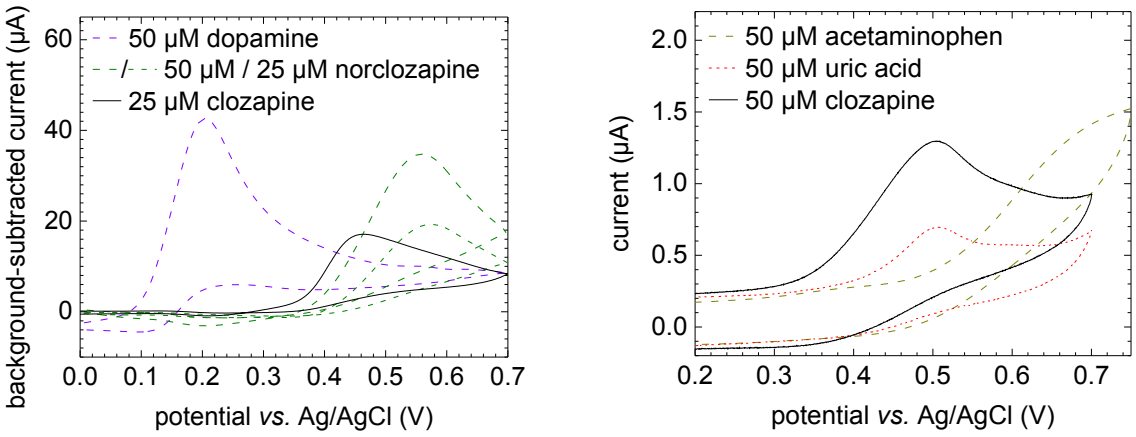


Figure 2.19: Cyclic voltammograms (oxidative region shown) measured with the redox cycling system for solutions containing various oxidizing mediators. (a) Baseline-subtracted measurements showing 25 μM clozapine (black solid); 25 μM (green dash dot) or 50 μM (green dash) norclozapine; and 50 μM dopamine (purple dash). Adapted with permission from [90]. (b) Measurements from 2 mm disk electrodes for 50 μM each of clozapine (black solid), uric acid (red dash), and acetaminophen (yellow dash).

### 2.1.7 Synopsis

I demonstrated that the chitosan-catechol redox cycling system offers high amplification of clozapine's electrochemical signal, yielding a limit of detection compatible with the clinical range. Moreover, I showed that the films are suitable for reuse and storage when proper corrections in data analysis are made. I explored the rich interplay of biomaterials and electrochemistry offered by the redox cycling system, highlighting that this enables differentiation of clozapine and its metabolite norclozapine. Additionally, I established selectivity with respect to a number of other relevant compounds and showed a dose-dependent clozapine response directly in serum with a clinically compatible limit of detection – a first for clozapine sensing methodologies. However, I found that the dominant serum interferent uric acid – though less amplified than clozapine – undergoes redox cycling in the chitosan-catechol system with a signal overlapping that of clozapine, calling for other strategies to supplement this sensing approach.

## 2.2 Alternative Electrode Materials

Gold is often the default material of choice for microfabricated electrochemical sensors due to its ease of fabrication and relative inertness, and indeed is utilized throughout most of this work for these very reasons. Yet, it is not as inert as often assumed, and may not be an optimal choice for a given sensor application [104]. The electrode material plays a critical role in determining analyte interactions. This includes surface morphology, direct physicochemical interactions with the analyte, as well as surface fouling or oxidation. For instance, different surface chemistry could reduce the free energy associated with clozapine oxidation, and surface morphology could provide more surface area for reactions to occur. In the case of the chitosan-catechol redox cycling system, the importance is two-fold as the electrode material will also affect the film deposition process.

Here, I consider materials covering a wide range of characteristics. Gold serves as a reference material, as well as the base layer on which the others are fabricated. Specifically, I investigate titanium nitride, platinum, platinum black, and glassy carbon. Platinum, like gold, is a noble metal like gold with low reactivity, but at the same time has well-established catalytic properties. This can shift the observed reaction potential of redox species, possibly enhancing sensor selectivity. Platinum black is atomically identical, but exhibits an extremely high surface roughness, sufficient to scatter most incoming light and therefore appear black [105]. This could be expected to further enhance electrochemical currents simply due to the increase in surface area. Titanium nitride possess characteristics at the other end of the spectrum as it is a conductive ceramic with high stability and inertness [106]. Glassy carbon is often utilized in macro-scale electrochemical systems due to its favorable properties [107], and for clozapine specifically could provide advantages due to resulting pi-pi interactions. At the macro-scale, this was indeed observed by my colleague Sheryl Chocron in her interference studies [100]. However, as carbon electrodes cannot be utilized for hydrolysis, I do not

expect to be able to form chitosan films (which rely on the hydrolysis-induced increase in local pH).

### 2.2.1 Experimental Methods

The underlying electrodes utilized are standard planar gold-on-silicon oxide as described previously, except with a surface area of only $5 \times 5$ mm$^2$. Fabrication methods for the three material types vary as much as the materials themselves. Titanium nitride is deposited using atomic layer deposition to yield a highly homogeneous layer to further emphasize its inert properties. Platinum black is formed by electrodeposition at 300 A/m$^2$ from a solution of 1% chloroplatinic acid, 0.0025% hydrochloric acid, and 0.05% lead acetate as a catalyst [108]. Platinum is similarly electrodeposited for consistency, at a third of the current density and without the lead acetate. Glassy carbon is formed by patterning negative SU-8 photoresist on top of the gold, and subsequently pyrolyzing it under an inert nitrogen atmosphere in a furnace (200 °C for 0.5 h, 900 °C for 1 h, 600 °C/h ramping) [109]. Chitosan-catechol modification, as well as testing procedures otherwise, are carried out as described in Subsection 2.1.1.

### 2.2.2 Surface Characterization

The titanium nitride yields an almost invisible film, adding only a slight tint to the inherent colors of the gold and the substrate. Platinum deposits as a shiny silver film, with platinum black exhibiting the expected black color. At the nanoscopic level, visualized in electron micrographs in Figure 2.20, observations differ slightly. Titanium nitride and gold both show similar low-contrast surfaces with only nanoscopic defects, in line with the conformal nature of ALD films. Platinum black, as expected, shows a highly structured surface, with fractal features from micro- down to nanometer length scales. Electroplated platinum – somewhat surprisingly – also reveals distinct roughness, albeit only at sub-micron length scales, explaining its optically reflective qualities.

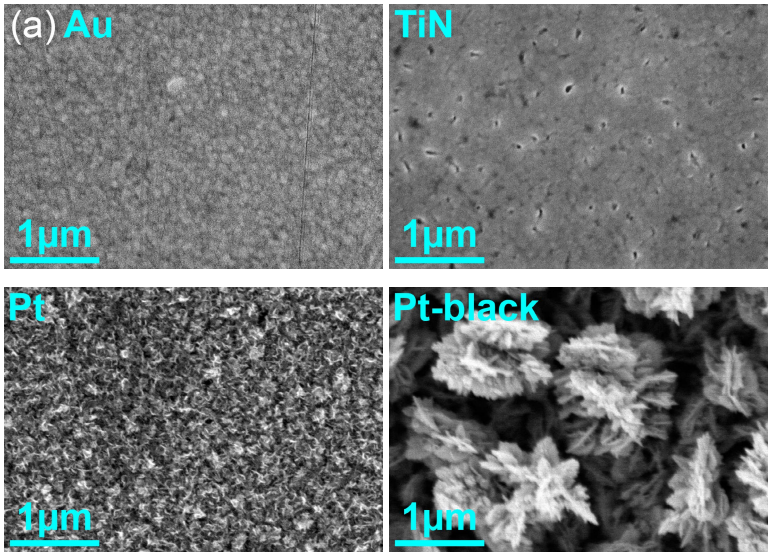


Figure 2.20: Scanning electron micrographs of gold, titanium nitride, platinum, and platinum black electrode surfaces. Adapted from [110].

Energy-dispersive X-ray spectroscopy confirmed the atomic nature of the observed structures. Glassy carbon represents a special case: Although the photoresist successfully pyrolyzes, the high temperatures appear to compromise the gold layer itself, resulting in gold and carbon peeling off the substrate. Although not exceeding the bulk melting temperature of gold, significant melting point suppression can occur at thicknesses in the hundreds of nanometers or less, potentially explaining this peeling effect. Glassy carbon microelectrodes were thus not pursued further.

For electrochemical characterization, I first utilize cyclic voltammetry with the standard ferri/ferrocyanide redox couple on bare electrodes as a control. This provides a measure of the electrochemical surface area independent of any specific clozapine-catalytic effects. I report the results in Table 2.3 as the peak current $I_p$-derived signal amplification relative to a bare gold electrode (*cf.* Equation 2.3). Titanium nitride shows a negligible 5% increase over gold, indicating that the surface area is still defined by the underlying gold electrode, rather than by lateral conductivity in the thin ceramic. With platinum, I see a 40% increase, confirming that electroplating yields non-negligible surface roughness in spite of its mirror-like visual appearance. Platinum black, as expected, shows

| material | ferri/ferrocyanide |
|---|---|
| gold | *1.00 ± 0.02* |
| titanium nitride | 1.05 ± 0.01 |
| platinum | 1.40 ± 0.04 |
| platinum black | 2.70 ± 0.18 |

Table 2.3: Effective electrochemical surface area as characterized using the model redox couple ferri/ferrocyanide. All values are normalized to that of gold (italics). Adapted from [110].

the biggest increase at 2.7-fold. These findings align well with the qualitative imaging observations.

### 2.2.3 Electrochemical Sensing

After the initial electrochemical characterization above, both bare and chitosan-catechol-modified electrodes are then tested with clozapine, where I quantify signal amplification relative to bare gold as per Equation 2.3. The experiments, summarized in Table 2.4, are conducted in both PB and PBS to investigate further the effects of chloride, which will become especially relevant for platinum. For gold, the redox cycling system yields ~ 3-fold amplification – in line with previous observations – with minimal difference between these condition. The generally high associated variability illustrates one of the challenges of the chitosan-catechol films on gold. During chitosan electrodeposition, cell potentials typically exceed +1.5 V, sufficient to cause oxidative surface fouling of the gold film, which I hypothesize is central to the high variability observed here [104]. Moreover, nanoscopic defects in the gold may be translated into much larger inhomogeneities.

For bare titanium nitride electrodes, I verify a practically identical response compared to gold in Figure 2.21a (PBS results shown; refer to the table for PB). This matches what was observed with the standard ferri/ferrocyanide redox couple. The intrinsic background reactions seen at potentials higher than that of clozapine – possibly related to ozone formation or hydrogen peroxide decomposition [111] – are also conserved, indicating they do not rely on surface chemistry. However, in the presence of

| material | clozapine in PB | | clozapine in PBS | |
|---|---|---|---|---|
| | bare | RCS | bare | RCS |
| gold | *1.00 ± 0.05* | 3.04 ± 0.59 | *1.00 ± 0.25* | 2.86 ± 1.25 |
| titanium nitride | 0.88 ± 0.07 | **6.14 ± 0.86** | 1.10 ± 0.15 | **7.54 ± 0.36** |
| platinum | **250 ± 56** | **125 ± 19** | **32 ± 11** | — |
| platinum black | **1490 ± 150** | — | **193 ± 20** | — |

Table 2.4: Electrochemical characterization results for the electrode materials studied in this work. Toward therapeutic drug monitoring of clozapine, materials were tested with (RCS) and without (bare) further redox-cycling system modification in either PB or PBS. For each group, the relevant gold reference is in *italics*, and relative amplification by more than a factor of five is in **bold**. Adapted from [110].

the redox cycling system, significant differences between the two become apparent. The signal amplification is 2.5-fold higher compared to the chitosan-catechol on gold, and the signal variability 9-fold lower. This aligns well with our hypotheses on the underlying reasons for the inherent variability with gold, in contrast to the highly homogeneous ALD titanium nitride film here [112].

With platinum in phosphate buffer, I observe an intriguing signal amplification of 250-fold as shown in Figure 2.21, and I confirm that this signal indeed depends on the clozapine concentration. However, the high amplification is largely lost upon switching to PBS, and the redox cycling system also decreases (rather than increases) the electrochemical signal. Furthermore, the signal variability is larger than 10% for all conditions. Apart from the higher currents, the corresponding peak potentials decrease significantly in PB, indicating that platinum functions as a redox catalyst as expected and reduces the need for an overpotential. The observed behavior regarding amplification, however, is counter-intuitive considering the much more limited signal enhancement with the ferri/ferrocyanide. A key difference between the standard redox couple and clozapine is the much slower (limiting; *cf.* Subsection 2.1.5) electron transfer kinetics of the latter compared to the traditional diffusion limitation of the former (akin to Fc). For a diffusion-limited reaction, surface roughness below the micron scale will hardly contribute, since the depletion layer thickness will extend far beyond (tens of microns)

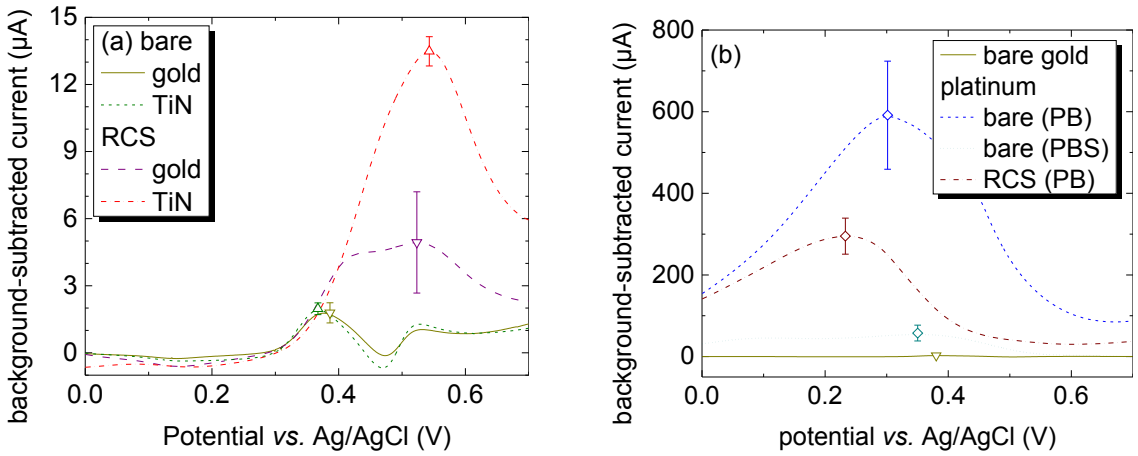


Figure 2.21: Cyclic voltammograms (oxidative section of third cycle) of clozapine solutions (b) in PBS utilizing gold and titanium nitride (TiN) electrodes, without or with further redox cycling system modification; (c) in PB or PBS utilizing gold and platinum electrodes, without or with further redox cycling system modification. Peak potentials are marked by symbols on the curves together with peak current standard deviations. Adapted from [110].

[88]. By contrast, kinetics-limited species like clozapine exhibit a much more surface-conformal depletion layer. These types of reactions are thus selectively amplified by nano-scale morphology such as observed in our platinum films. This effect has previously been observed and exploited with enzyme-free sensors for glucose, another redox kinetics-dominated analyte [113,114]. The performance decrease with the redox cycling system also supports this interpretation, as the film will slow down diffusion and decrease the dominance of electron transfer kinetics. The lower signals in the presence of chloride are believed to be due to formation of a Pt-Cl complex at the electrode surface [115]. This presents a major hurdle to the otherwise impressive performance of a bare platinum clozapine sensor, since chloride will also be present in biological samples. The high variability presents another limitation – this is notably not observed with the standard redox couple, thus likely related to the sub-micron morphologies. The mechanism could therefore be similar to that which resulted in the high variability with the redox cycling system on gold – nanoscopic defects compounding to much larger effects upon deposition.

Platinum black further amplifies the clozapine signal over that observed with

platinum, again far more than the 2.7-fold increase seen with ferri/ferrocyanide. As with platinum, the almost 1500-fold amplification decreases rapidly in the presence of chloride, and suffers from high variability. Here, however, variability is already significant for the standard redox couple, aligning well with the presence of both micro- and nanostructures. No film deposition was attempted based on the negative results with platinum alone. Moreover, the platinum black electrodes degraded rapidly after fabrication within a few days, likely due to surface oxygen interactions [116]. Even more so than platinum itself, platinum black thus shows impressive clozapine detection performance that are outweighed by a number of limitations for real-world use.

### 2.2.4 Synopsis

I discovered that platinum and platinum black can serve as highly sensitive clozapine sensors based on redox catalysis and clozapine's slow reaction kinetics. Associated drawbacks are high variability as well as negative interactions with chloride, which present challenges with application to biological samples. For the redox cycling system, I found that titanium nitride offers a significantly better underlying electrode surface compared to gold, reducing noise, and increasing signal amplification.

## 2.3 Redox Catalysis System

Instead of modifying chitosan post-deposition, carbon nanotubes or graphene can be physically mixed into the chitosan solution. Compound films can then be directly electrodeposited, as pioneered by my colleagues Dr. Eunkyoung Kim and Dr. Mijeong Kang. These films offer three advantages: First, the aforementioned favorable pi-pi interactions between carbon compounds and clozapine; second, an increase in electrode surface area from the high-surface-area conductive carbon network in the film; third, electrocatalytic properties akin to those provided by platinum [117–119]. These features

are expected to significantly amplify electrochemical signals in general, and clozapine's in particular, in addition to reducing required overpotentials and thereby shifting observed signal peaks closer to their inherent $E^{o\prime}$. Here, I present data concerning these hypotheses, focusing specifically on the film's selectivity to critical interfering species as well as on sensitivity in clinical serum samples.

### 2.3.1 Experimental Methods

Experimental methods largely follow those employed in Subsection 2.1.1, with commercial 2 mm diameter gold working electrodes. Carbon nanotubes up to 5% w/v or graphene up to 2% w/v are dispersed in chitosan solution by ultrasonication for 45 minutes, preceded and followed by brief vortex mixing. Immediately thereafter, films are electrodeposited onto the electrode surface at a constant cathodic current of 8 A/m² for 60 s (CNT) or 90 s (graphene or mixtures). Excess material is allowed to dissociate with the electrode immersed in DI water, followed by PB prior to experiments.

The measurement method utilized, unless noted otherwise, is differential pulse voltammetry. The chosen parameters are a potential sweep from 0 to +0.7 V at a scan rate of $\nu = 2$ mV/s in discrete 1 mV steps, overlaid with $\Delta E = 50$ mV, $\tau = 200$ ms pulses. The current is measured just before the current pulse as well as at its end and expressed as a differential current. The main advantage offered here is that the differential nature of the measurement suppresses non-faradaic background currents, and yields sharper peak definition of electrochemical signals [88]. For reference, the peak current in DPV is described by:

$$I_{\mathrm{p}} = ACFn\frac{1-\exp\left(\frac{nF\Delta E}{2RT}\right)}{1+\exp\left(\frac{nF\Delta E}{2RT}\right)}\sqrt{\frac{D}{\pi\tau}} \tag{2.5}$$

In this Section, experiments are carried out with clozapine-spiked serum samples from healthy subjects are employed instead of the commercial human serum employed

in Section 2.1. These samples more closely resemble clinical patient samples, and were collected at the Maryland Psychiatric Research Center under procedures approved by the University of Maryland, Baltimore, Institutional Review Board (HCR-HP-00058348-2, "Screening protocol for the evaluation of research participants", and HCR-HP-00058348-2, "Microsystem Development for Clozapine Monitoring in Schizophrenia", both subject to yearly review; and ). In the course of this study, blood is collected from healthy control subjects as well as from schizophrenia patients, either treated with clozapine or on a different treatment regimen. The serum is fractionated out in the collection tubes on site, and aliquoted for research use as well as centralized clinical laboratory analysis for clozapine. Samples are kept frozen until use.

### 2.3.2 Sensitivity and Selectivity

To verify the hypothesis of redox catalysis improving selectivity, a bottom-up-type experiments with clozapine and select interferents in buffer solutions is shown in Figure 2.22a [120]. Specifically, this illustrates the the electrochemical signals of clozapine, uric acid, and norclozapine with 2% chitosan-graphene electrodes. Clozapine's oxidative peak is observed at its $E^{o\prime} = +0.37$ V, similar to observations on bare gold electrodes in earlier Sections, but amplified $\sim$ 50-fold. Uric acid, critically, shows a redox signal at significantly lower potentials around 0.2 V – in stark contrast to the overlap observed with the chitosan-catechol system in Subsection 2.1.6. This verifies the hypothesis that the low-dimensional carbon compounds reduce the required overpotential for oxidation of this dominant serum interferent. Norclozapine, on the other hand, shows indistinguishable redox activity from clozapine. Unlike the chitosan-catechol system in Subsection 2.1.5, the chitosan matrix here does not impart selectivity between these two compounds. In the redox catalysis system, the redox reaction can occur at or near the surface of the compound film due to the conductive carbon network, eliminating the need for diffusion through the porous, charged chitosan network. While a drawback compared to the

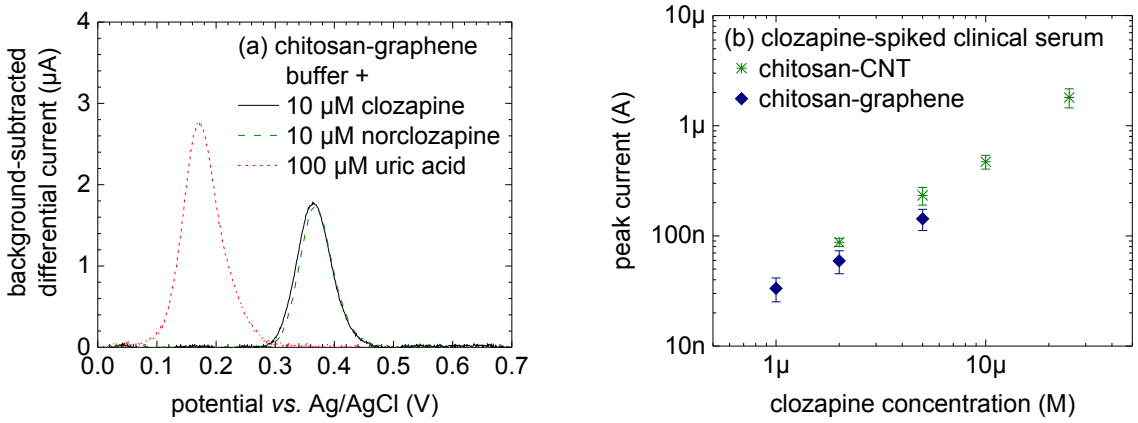


Figure 2.22: Selectivity and sensitivity of the redox catalysis system. (a) Differential pulse voltammograms from clozapine (solid black), uric acid (dashed red), and norclozapine (dashed green) in buffer solutions with chitosan-graphene electrodes, with the buffer background current subtracted. (b) Clozapine detection in spiked clinical serum from healthy subjects plotted in terms of peak current as a function of concentration for both chitosan-CNT (green) and chitosan-graphene (blue) electrodes. Adapted with permission from [85] and [120].

chitosan-catechol system, the summed clozapine and norclozapine concentration (which the redox catalysis system would thus measure) can still serve as a useful clinical marker [121].

With the selectivity for clozapine over uric acid established, measurements in human serum should prove relatively straightforward with the redox catalysis system. Indeed, a calibration plot can be obtained directly from the DPV peak currents measured in spiked clinical samples from healthy subjects as shown in Figure 2.22b. Following previously utilized definitions, I calculate a sensitivity of 1.04 log A / log M (chitosan-CNT) and 0.91 log A / log M (chitosan-graphene), with corresponding limits of detection of 0.55 μM and 0.73 μM clozapine. Both systems are further validated with serum samples from people with schizophrenia currently undergoing clozapine treatment (not shown; *cf.* [85,120]). The higher sensitivity and lower detection limit of the CNT-based films can likely be attributed in part to the higher carbon mass loading at 5%, compared to 2% for graphene. Both of these loadings are at the very upper limit for effective suspensions. On balance, graphene appears to perform better in the redox catalysis system, as its signals

lag behind those of the CNT by less than the 2.5-fold difference in mass loading. Its 2% suspensions are moreover subjectively less prone to aggregate formation and variability in film formation. Compared to the chitosan-catechol redox cycling system results in Subsection 2.1.6, the limit of detection here falls in a very similar range. The redox catalysis system offers greater selectivity, however, as those same figures of merit could be obtained with voltammetry as opposed to chronocoulometry. The difference in methods also accounts for the difference in linear behavior and thus the incomparability of the sensitivity values; since sensitivity remains roughly conserved in the double-logarithmic representation between serum and buffer samples such as those in Subsection 2.1.3, the redox catalysis system likely also scores better on that metric by a factor of two.

### 2.3.3 Synopsis

I demonstrated that the chitosan-CNT/graphene redox catalysis system offers high amplification of clozapine's electrochemical signal, with only minimal interference of the dominant serum interferent uric acid. This enabled similarly sensitive, more selective detection of clozapine directly in clinical serum samples as compared to the redox cycling system. However, I showed that clozapine and its metabolite norclozapine exhibit overlapping electrochemical signal peaks and cannot be differentiated with the redox catalysis system.

## 2.4 Chapter Summary

In this Chapter, I have explored various electrochemical sensing strategies for clozapine. Both the chitosan-catechol redox cycling system and the chitosan-CNT/graphene redox catalysis system have been shown capable of detecting clozapine directly in human serum with limits of detection below 1 μM. This is in line with clinical requirements as laid out in Subsection 1.3.1, and represents a breakthrough for electrochemical sensors,

which to date have relied on extensive sample pre-treatment procedures as reviewed in Subsection 1.3.2. I have also demonstrated the potential of high-surface-area platinum surfaces for electrochemical clozapine detection, with even higher signal amplification than chitosan-CNT/graphene. Particularly with the chitosan-catechol redox cycling system, I have further explored the molecular mechanisms and interactions underlying its functionality, from film stability to diffusion effects. All modalities offer unique advantages – as well as limitations. Platinum is susceptible to performance degradation by chloride, present in biological samples. The chitosan-catechol system allows for differentiation between clozapine and its metabolite norclozapine, but uric acid interferes with clozapine's signal. The chitosan-CNT/graphene system shows the reverse behavior, and allows for more selective detection in serum. The latter moreover does not rely on a separate reducing mediator. Therefore, the redox catalysis system is the best candidate for a stand-alone electrochemical clozapine sensor, and is thus selected for the integrated system in Chapter 4. However, future work (*cf.* Section 5.3) should focus on integrating these modalities in an array of sensors to ultimately unlock their full synergistic potential.

# Chapter 3

# Hydrodynamic Focusing and Osmotic Lysis for Impedance Cytometry

Even if flawless implementations of all the individual components needed in a clozapine treatment monitoring lab-on-a-chip (blood fractionation, differential cell counting, clozapine sensing) were available today, the barrier of system integration remains. In a microsystem combining these elements, a multitude of interactions, respective limitations and requirements has to be considered. The flow rates are one main aspect of this in an interconnected microfluidic device, governed not only by the external inputs, but also by the fluidic resistances of all other parts of the design (for the relevant theoretical treatment, see Subsection 4.1.4). Another example is that solutions to induce red blood cell lysis could interfere with an impedance-based cell sizing method due to the altered

solution resistivity. These points illustrate the challenges of microsystem integration; overcoming these is a major contribution of this thesis.

To gain a better understanding of such microsystem integration, in this Chapter I investigate integration of two critical sub-systems. First, in Section 3.1, that of impedance cytometry with in-plane hydrodynamic focusing for enhanced sensitivity. Second, in Section 3.2, that of impedance cytometry with osmotic lysis of erythrocytes to enable entirely label- and reagent-free white blood cell counting. Although hydrodynamic focusing and osmotic lysis themselves are not novel concepts, in this Chapter I present the first studies of systems interplay, highlighting the promise and feasibility of a fully integrated device.

## 3.1 Hydrodynamic Focusing for Enhanced Sensitivity

One challenge for impedance cytometers becomes evident by considering the simplified governing Equation Equation 1.1: $|\Delta Z| \propto \phi^3/DA^2$. Thus, the relative change in impedance caused by a cell of diameter $\phi$ passing through the aperture $DA$ is strongly dependent on their relative size, with the aperture optimally as small as possible – that is, $DA \approx \phi$ considering the obvious constraint that the aperture cannot be smaller than the cell. However, this optimization condition competes with biophysical limitations of blood – granulocytes generally have diameters on the order of 10–15 µm, but clusters of cells or other (albeit rarer) cell types in circulation can significantly exceed that, with macrophages at ~ 20 µm [45]. An impedance cytometer perfectly matched to granulocyte sizes will thus inevitably clog.

Hydrodynamic focusing has long been studied in microfluidics, and has even been applied to cytometry (including impedance cytometry), with Larsen *et al.*'s initial microfluidic implementation a prime example as discussed in Subsection 1.3.3. The approach relies on laminar flow phenomena to tightly confine a sample stream within one or more sheath flows. Its appeal is many-fold, providing 1) sample dilution to avoid

coincident cell counting events and 2) well-defined cell positioning with respect to the detector to reduce variability. For impedance cytometry, non-conductive sheath flows in particular have the added advantage of also providing 3) detection volume confinement within the (conductive) sample stream between the non-conductive sheaths. This results in a virtual aperture $VA$ within a potentially much larger channel that offers the same benefits as a smaller physical aperture $DA$ while minimizing the risk of clogging from larger cells or aggregates.

As mentioned earlier, a few researchers have previously considered these advantages with regard to impedance cytometry. Akin to the initial concept by Larsen *et al.*, a study by Rodriguez-Trujillo *et al.* employs in-plane DI water sheath flows for particle counting [53,122]. Although both consider the hydrodynamics involved (the latter in depth), both are lacking in experimental characterization of cytometry performance. Works by Bernabini *et al.* and Evander *et al.* are aimed at impedance analysis of bacteria and platelets, much smaller than typical blood cells, made possible by in-plane oil-based sheath flows [123,124]. The systems interplay between focusing and cytometry, however, is only considered briefly in – respectively – theory and experiments. The two-phase flow approach is moreover prone to suffer from interfacial instabilities which can disrupt the flows [125,126]. Many other researchers have further considered adding additional confinement in the out-of-plane direction, as again pioneered (though not characterized) by Larsen *et al.* utilizing additional sheath flows [125,127,128]. Alternative approaches employing inertial, acoustic, or other forces have also been investigated [52,58,59,126,129].

Still, the systems interplay of in-plane hydrodynamic focusing with impedance cytometry – upon which many of the more elaborate techniques are based – remains poorly understood. My study of the systems interplay consists of two parts: Modeling and device experiments. Both are equally critical to develop a comprehensive understanding of the phenomena at play. I construct models both analytically and numerically to consider geometrical design parameters as well as experimental parameters such as

flow rates, frequency dependence, *etc.* I conduct experiments with two populations of polystyrene beads – equivalent to cells under certain conditions – to validate models and reveal dependencies not captured by either modeling approach.

### 3.1.1 Design Overview

My design, shown in Figure 3.1, employs co-planar microelectrodes at a distance $d$ = 170 µm downstream from a hydrodynamic focusing junction, where the sample stream (flow rate $Q_s$) is met perpendicularly by two streams of DI water (combined flow rate $Q_f$ from a shared inlet port) [130]. The co-planar electrode design avoids the alignment challenges in fabrication of facing ones with only a minor trade-off in sensitivity – provided the channel height is dimensioned close to the cell diameter of interest, thereby limiting the variability of how close (or far away) these cells pass over the electrodes [54]. The water sheath flows provide lateral confinement of the detection volume over the electrodes. The perpendicular confluence angle design has previously been shown to provide the tightest focusing over distances less than 1 mm [131,132].

Specifically, my design to study the interplay of hydrodynamic focusing and impedance cytometry utilizes microfluidic channels with a height of $h$ = 20 µm (close to the ~ 15 µm diameter of granulocytes) and a width of $w$ = 50 µm to still allow for passage of larger cells and aggregates. Electrode width and spacing are chosen as $l = g$ = 25 µm based on design rules for interdigitated electrode sensors as well as biophysical cell size considerations [133]. Furthermore, I study the hydrodynamic focus channel width $w_{fc}$, a parameter that has not previously been considered with respect to hydrodynamic focusing geometries. I choose to operate in a creeping flow regime of constant Reynold's number $Re < 1$, *i.e.* constant total flow rate, specifically $Q_s + Q_f$ = 40 µl/h based off of instrumentation capabilities.

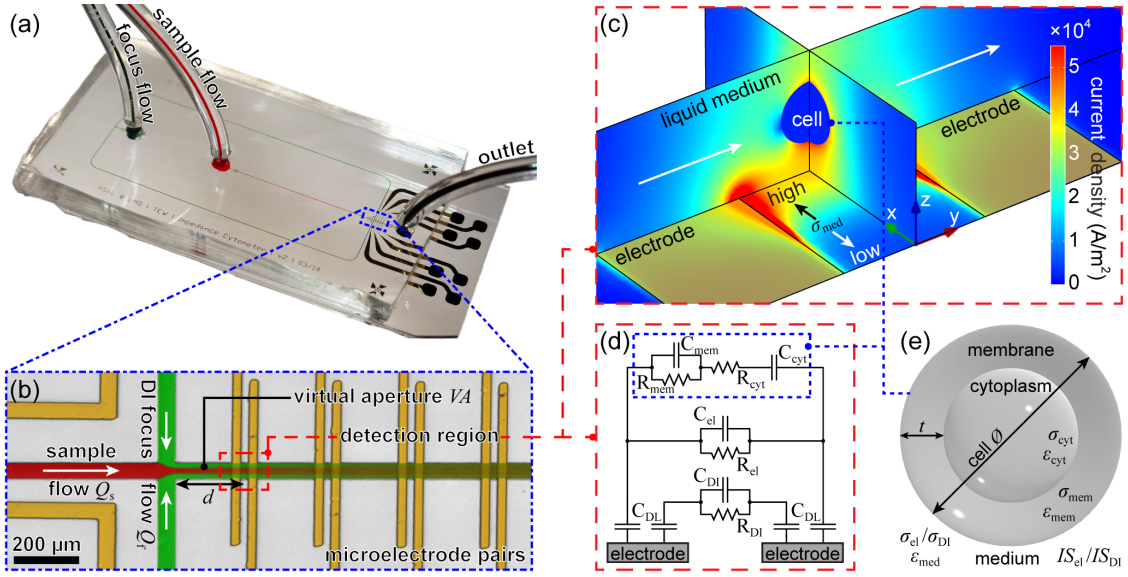


Figure 3.1: (a) Photograph of my impedance cytometry lab-on-a-chip. The microfluidic channels are filled with dye to enhance visualization. (b) Micrograph of the region of interest highlighted by the blue dash-dotted box in (a). In-plane hydrodynamic focusing is schematically illustrated by overlaid numerical simulation for a 1:1 ratio of sample (particles in electrolyte; red) to focus (DI water; green) flows. The virtual aperture $VA$ sample confinement is conserved downstream, where impedance is measured across the first gold microelectrode pair, separated from the junction by distance $d$. The other pairs serve as backups and are not utilized here. (c) Numerical impedance cytometry model corresponding to the red dashed box in (b). The cell (center) is suspended in a microchannel between two electrodes (bottom; gold rectangles). The colors correspond to the current density from blue (low) to red (high), clearly illustrating the diffusely focused electrolyte, with conductivity $\sigma_{\text{med}}$ ranging from high in the center to low on either side. (d) Analytical equivalent circuit model corresponding to the red dashed box in (b). Shown for $VA > \phi$, this accounts for conduction pathways from the cell (top), the electrolyte (middle), as well as the ionic double layer capacitance and the DI water aperture (bottom). (e) Model of a cell as a spherical shelled particle consisting of cytoplasm and membrane, surrounded by liquid medium. Reproduced with permission from [130].

### 3.1.2 Analytical and Numerical Models

The analytical and numerical models both consist of three aspects: A hydrodynamic model to predict the virtual aperture width $VA$ based on geometry and flow parameters, an electrodynamic model to calculate impedance cytometry performance based on geometry and environment, and an approach for coupling these two aspects for comprehensive analysis. Although numerical models are exceedingly useful in modeling complex systems and geometries, they are at a small but nonzero risk to produce nonsense results through solutions in local, rather than global, minima. Thus, analytical models are critical to validate numerical model results. They also require significantly less computing power, allowing for much faster exploration of the (albeit smaller) parameter space that is accessible to them.

For hydrodynamics, an analytical description of in-plane flow focusing was published by Lee *et al.* [134]. It defines the ratio of focus to total flow rate $FR$ and how that relates to the downstream width of the focused flow – *i.e.* the virtual aperture width $VA$ – based on the channel's geometric parameters:

$$FR = \frac{Q_s}{Q_s + Q_f} = \frac{VA}{w}\gamma\left(VA, w, h\right) \tag{3.1}$$

$$\text{where } \gamma\left(VA, w, h\right) = \frac{1 - \frac{192h}{\pi^5 VA}\sum_{n=0}^{\infty}\frac{\sinh\left(\frac{\pi(2n+1)VA}{2h}\right)}{(2n+1)^5\cosh\left(\frac{\pi(2n+1)w}{2h}\right)}}{1 - \frac{192h}{\pi^5 w}\sum_{n=0}^{\infty}\frac{\tanh\left(\frac{\pi(2n+1)w}{2h}\right)}{(2n+1)^5}}$$

The velocity ratio $\gamma$ arises out of integrating the velocity profile in the sample and focus flow streams. The form of this equation obviates a closed-form solution for $VA(FR)$, but the problem is nonetheless easily solved by a numerical root-finding algorithm in Wolfram Mathematica.

My finite element model, overlaid in Figure 3.1b, fulfills the same overall purpose, but can offer a few refinements [130]. I implement it in COMSOL Multiphysics utilizing

coupled Creeping Flow and Transport of Diluted Species modules. It allows for variations in the focus channel geometry not considered in the analytical model, such as their angle with respect to the sample channel or the width of the focus channels $w_{fc}$. Most importantly, this allows for including diffusion of ions ($D_{ion}$ = 16.83 µSt; average of dominant sodium and chloride ion diffusion coefficients [135]) that ultimately determine medium conductivity $\sigma_{med}$ and thus the virtual aperture $VA$. I similarly include slow-diffusing cells ($D_{cell}$ = 1 nSt; red blood cell diffusion coefficient [136]) in the sample stream as a control. Diffusion of the ions into the DI water sheath flows eliminates a clearly-defined two-phase virtual aperture in the finite element model. Instead of a simple $VA$ value it provides a concentration profile $C(x)$ (normalized to the input concentration) across the width of the channel at a given distance $d$ downstream from the focusing junction. A limiting factor of the employed numerical model is its 2-dimensional nature, which neglects out-of-plane variations in ion concentration.

Although the concentration profile allows for direct coupling into a numerical electrodynamic model as described below, deriving a value for $VA$ is still useful for assessing the impact of diffusion exclusively on the hydrodynamics and for comparison to the analytical model. Analytically, diffusion profiles are described by the sigmoidal error function, and can be closely approximated by hyperbolic trigonometric functions that are more amenable to curve fitting algorithms. For my case of symmetric flow focusing, the diffusion profiles can thus be fitted with the double-sigmoidal peak function as shown in Figure 3.2:

$$C(x) = C_{offset} + \frac{1}{2} C_{amp} \left( \tanh\left( \frac{2x + s_p}{4 s_s} \right) - \tanh\left( \frac{2x - s_p}{4 s_s} \right) \right) \tag{3.2}$$

This describes the ionic concentration profile in terms of only four parameters: The offset from zero $C_{offset}$, the double sigmoidal peak amplitude $C_{amp}$, the peak's full width at half maximum $s_p$, and the width (= 1/steepness) of the peak's slope $s_s$, yielding fit errors of less

than 2% for all conditions studied. Based on these parameters, I design an approximation for the virtual aperture as:

$$VA = C_{\text{amp}}\left(s_{\text{p}} + s_{\text{s}}\right) + \frac{C_{\text{offset}}}{C_{\text{offset}} + C_{\text{amp}}} s \tag{3.3}$$

This form converts the diffusion profile into a roughly equivalent discrete-phase concentration profile as overlaid in Figure 3.2 [130]. The first term considers the central focused concentration profile, somewhat analogous to integrating the double sigmoidal peak (without its offset). The second term accounts for the offset – which reduces the efficacy of any focusing in the center – by integrating over the area under the offset, scaled to the prominence of the central peak. The equation is designed such that for limiting cases, it reduces to expected values: For completely discrete phases ($C_{\text{amp}} = 1$, $C_{\text{offset}} = 0$, $s_{\text{s}} = 0$) it yields $VA = s_{\text{p}}$, while for complete interdiffusion ($C_{\text{amp}} = 0$, $C(x) = C_{\text{offset}}$) it reduces to $VA = w$, reflecting the equivalence to a simple decrease in input concentration and the resulting lack of flow focusing effects.

For electrodynamic modeling, impedance cytometry itself has been extensively analyzed in the works of Gawad, Morgan, Sun, and others [54,59,137]. They derive an equivalent circuit model for the cell between the electrodes based on a model of the cell as a spherical shelled particle (Figure 3.1e). Therein, the cell membrane (thickness $t$) and cytoplasm, with respective conductivities $\sigma$ and relative permittivities $\varepsilon$, are treated as the two relevant components of a spherical cell of diameter $\phi$. The equivalent circuit model likewise assigns each component a respective resistor and capacitor value in parallel, arrayed in a series circuit. Maxwell's Mixture Theory allows for derivation of an overall effective conductivity and permittivity, including the surrounding medium [138,139]. The double layer capacitance at the electrodes can be included as an additional series circuit element [140]. For coplanar (rather than facing) electrodes, the highly non-uniform electric field presents an added challenge that can be addressed through

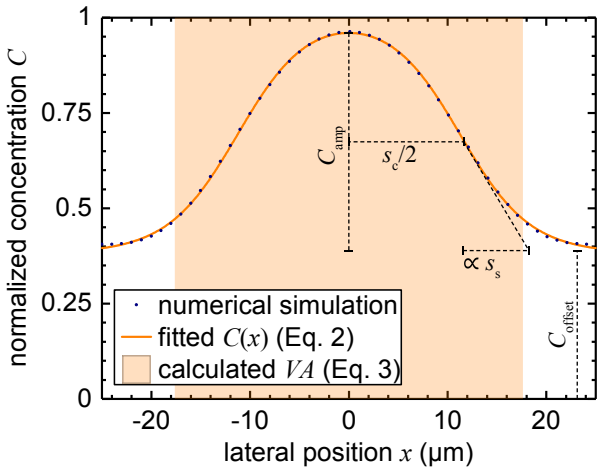


Figure 3.2: Concentration (averaged along the height of the channel and normalized to the input concentration) as a function of lateral position in the channel for an exemplary $FR = 0.75$ (total flow 40 µl/h). The plot shows both numerical data (blue dots) as well as the corresponding fit with Equation 3.2 (orange line). The fit parameters are illustrated with black dashed lines, and the corresponding $VA$ according to Equation 3.3 overlaid as as an orange rectangle (illustrating a discrete-phase concentration profile resulting in the same $VA$ value). Reproduced with permission from [130].

Schwarz–Christoffel mapping, constructing an equivalent facing electrode scenario [133].

While these aspects of the model have been published on, they have never been presented in a fully integrated form. I address this in my thesis, and extend the approach to be able to account for hydrodynamic focusing. The model is implemented in Wolfram Mathematica and included in Appendix B: Analytical Model [130]. I choose a Helmholtz approximation for the ionic double layer with a capacitance of $F = lw\varepsilon_{\mathrm{med}}/\lambda_{\mathrm{D}}\,(IS)$, where $\lambda_{\mathrm{D}}$ is the Debye length as a function of the relevant ionic strength. For coupling the hydrodynamic and electrodynamic models, assuming discrete phases of focusing and sample flows downstream of the focusing junction as in analytical hydrodynamic model, entirely parallel conduction pathways are introduced: One inside the focusing DI water, another one through the sample solution containing the cell. For the case of $VA > \phi$, this is illustrated in Figure 3.1d. However, focusing can exceed this condition to yield $VA < \phi$, *i.e.* parts of the cell exposed to pure water, with only the center spherical section $P_{\mathrm{el}} = \frac{1}{12}\pi VA\left(3\phi^2 - VA^2\right)$ still inside the sample solution. I account for this by modifying

the volume fraction $\Pi = P/V$ of the particle within the electrical interaction volume by substituting $P \longrightarrow P_{\mathrm{el}}$. The remaining particle volume $P - P_{\mathrm{el}}$ is then conversely introduced into the particle fraction within the focus flow (otherwise 0 for $VA > \phi$).

I implement the finite element model in COMSOL Multiphysics, relying on the Electric Currents and Electrical Circuits modules. With the aforementioned Maxwell's mixture theory, the cell can be modeled as a homogeneous sphere with an effective conductivity and permittivity [141]. It is placed in a microchannel between electrodes as shown in Figure 3.1c. Again, the numerical model allows for exploration of a much bigger parameter space such as cell location (enabling also transient cell passage studies). For the double layer capacitance, I rely on the same approximation as in the analytical model, included as circuit elements at the electrodes. To couple in the hydrodynamic model, the suspending electrolyte is described as a continuous phase with conductivity $\sigma_{\mathrm{med}} = \sigma_{\mathrm{el}} C_{\mathrm{ion}}(x)$, *i.e.* as the electrolyte conductivity scaled linearly by the ion concentration calculated in the numerical hydrodynamic simulation. The double layer is similarly adapted by substituting $IS \longrightarrow IS_{\mathrm{DI}} + IS_{\mathrm{el}} C_{\mathrm{ion}}(x)$. Although the linear assumption for conductivity neglects certain non-linear contributions, these become exceedingly complex for multi-ionic electrolytes such as PBS and only yield corrections on the order of 15% even at high dilutions (where they would be most pronounced) [142,143]. A limiting factor for the coupled model is that it neglects changes in flow and ion concentration caused by the particle, such as boundary layer formation around it.

### 3.1.3 Device Fabrication

The design is implemented in two physical layers – the coplanar electrodes on glass, and the microfluidics in PDMS. The fabrication process flow is schematically illustrated in Figure 3.3. The electrodes are fabricated by first depositing 20 nm chrome (functioning as an adhesion layer) and 200 nm gold on a borofloat glass wafer utilizing e-beam deposition. Subsequently, I clean the metal utilizing a 60 s immersion in Piranha (1:3 hydrogen

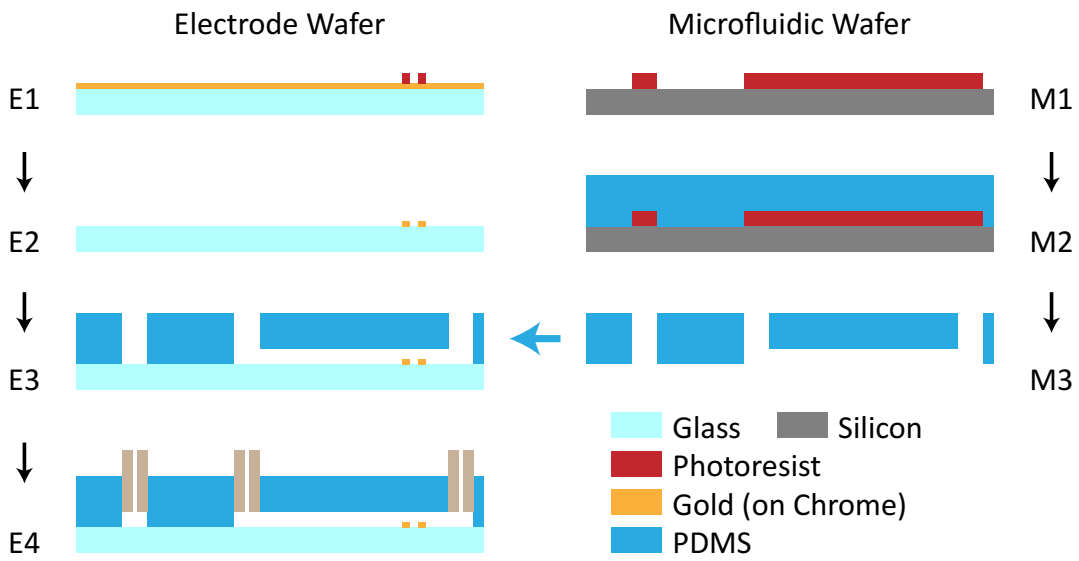


Figure 3.3: Abbreviated fabrication process flow for the first-generation devices described in the text.

peroxide : sulfuric acid), and dehydrate on a hotplate for at least 5 minutes. Then, I spin-coat a layer of Shipley 1813 positive photoresist (4 s ramp, 4000 rpm, 30 s hold), followed by a 60 s bake at 115 °C. The photomask 6.2 shown in Appendix A: Photomasks (printed on transparency film) is used to expose the resist to 140 mJ/cm² UV light, followed by another 60 s bake at 115 °C. I develop the resulting patterns for at least 45 s in Microposit 352 developer, followed by incremental 5 s immersions guided by pattern inspection under a microscope (E1). Finally, I wet-etch the exposed metal utilizing Transene TFA (gold) and 1020 (chrome) etchants (E2). The process is monitored utilizing microscopy and conductance measurements. To protect the structures from scratches during the subsequent wafer dicing, the entire wafer is again processed with photoresist as described above, only utilizing flood exposure with a 3-fold higher dose and omitting development.

For the microfluidics, I spin-coat negative SU-8 2015 photoresist to a thickness of ~ 20 µm (4 s ramp, 500 rpm, 10 s hold, followed by 3 s ramp, 1700 rpm, 30 s hold) on a dehydrated Piranha-cleaned blank silicon wafer, followed by a 25 minute bake at 60 °C (ramped up from room temperature at 5 °C/minute). Utilizing the photomask 6.3 shown in Appendix A: Photomasks, again on transparency film, I expose at a dose of

157.5 mJ/cm$^2$, followed by another 60 °C bake for 35 minutes (same ramp speed). I find that the long bake times and slow ramp speeds (compared to manufacturer specifications) used throughout processing are necessary to prevent the formation of small bubbles in the photoresist layer. The patterns are developed by immersion in SU-8 developer for ~ 5 minutes, stopped by a rinse in isoproyl alcohol, whereafter I inspect geometries under a microscope and utilizing a contact profilometer (M1). I hard-bake the resist at 150 °C for 10 minutes (ramp as before). To prepare the wafers for PDMS molding, I submerse the wafer in a solution of ~ 0.35% Alconox in water for five minutes, then spin-dry. The detergent is intended to form a non-stick coating on the silicon, enabling removal of the molded PDMS. Spin drying was found to yield better coating retention than blow drying, and a more homogeneous coating than evaporation drying. PDMS is prepared as a 10:1 mixture of Sylgard 184 base to curing agent to a total weight of 33 g, mixed well and degassed under vacuum until no bubbles are observed. I pour the liquid PDMS over the molds and cure it in a box furnace utilizing a 5 minute ramp up from room temperature to 60 °C, followed by a 15 minute hold time (M2). I remove the PDMS when the oven cools to ~ 55 °C, where the PDMS has lost most of its inherent stickiness but is not yet fully cured. I dice the PDMS slab using a knife, and punch connection holes utilizing 2 mm diameter biopsy punches (M3).

For assembly, I clean the electrode chips by rinsing successively with acetone, methanol, isopropanol, and DI water, followed by immersion in Piranha solution for 60 s. Both the electrodes and the microfluidics are rinsed with DI water and blow-dried. I expose both layers to oxygen plasma in a cylindrical chamber at a pressure of 1 Torr, power of 20 W, for 30 s, in line with existing literature on the strongest glass/PDMS bond [144]. Drop-coating the electrode chip with methanol immediately after removal from the plasma chamber allows for alignment of the two layers under a stereomicroscope without instantaneously forming a permanent bond. It further strengthens the ultimately resulting bond due to the negative pressure created by methanol pervaporation. Finally,

I fully cure the devices in a box furnace with a 15 minute ramp to 60 °C, followed by 3 hours hold time, and left to cool down naturally (E3). I verify final geometries to be within 10% of specifications under an optimal microscope.

### 3.1.4 Experimental Methods

The electrodes are connected to an Agilent E4980A Precision LCR meter using spring-loaded pins and coaxial cables. I employ an AC potential of 0.7 Vrms at a frequency of 100 kHz to read out the absolute impedance $Z$. The instrument is capable of a single measurement per 5 ms, which presents a limitation for other experimental parameters. Specifically, since the electrical interaction volume is roughly $V = wh\,(2l + g)$, a particle has to reside within that volume for a comparable time. Thus, the maximum possible total flow rate is on the order of $V/5$ ms, or approximately 55 µl/h.

Flow actuation is provided by two New Era NE-1002X syringe pumps, holding plastic 1 ml syringes connected to the microfluidic inlet ports using 30- or 32-gauge needles and Tygon tubing (0.19 mm inner and 2.03 mm outer diameter; shown as E4 in Figure 3.3). The compliant nature of the PDMS and the tubing creates an excellent friction-fit seal. Although the syringe pumps are chosen for their nanometer-size stepping, flow rates should still be maximized to provide accurate flow control. High flow rates further reduce other artifacts such as particle settling, *etc.* To balance these requirements with the upper limit given by impedance readout and the overall $Re < 1$ creeping flow condition, I choose a total flow rate of $Q_s + Q_f = 40$ µl/h, varying the ratio between flows to explore flow ratios from $FR = 0.875$ down to 0.075. The sample stream is provided by 1× PBS solution containing polystyrene beads of diameters $\phi = 6$ µm and 10 µm, as well as 10.9% w/w sucrose to match solution and particle density, minimizing particle settling. The focus flow consists of DI water with resistivity > 17 MΩ cm.

I control flows and record data with custom graphic user interfaces developed in LabView. For each flow condition, the experiments run for 0.5 to 2 hours to ensure

sufficient sample sizes. I analyze the data in MATLAB, employing the code in Appendix C: MATLAB Code. It determines the background signal $Z_{\text{empty}}$ by first removing obvious peaks and outliers from the raw $Z$ signal based on the second derivative and then applying a 9 Hz low-pass filter. I subsequently calculate $|\Delta Z|$ and detect peaks using a simple built-in algorithm. This set of local maxima is transformed into histograms using OriginPro. By fitting a Gaussian distribution between the first and second minima in the histograms, I derive population averages and spreads.

### 3.1.5 Theoretical Analysis

As mentioned previously, the virtual aperture $VA$ represents the critical hydrodynamic parameter for impedance cytometry. Thus, it provides a logical starting point to begin the theoretical analysis of systems interplay. The primary control parameter for a given geometry is the flow ratio $FR$ between sample and total flow rates as evidenced by the analytical Equation Equation 3.1. While this is independent of the absolute flow rates, the numerical model introduces diffusion and is thus expected to be affected by changes in those as well. In Figure 3.4, I plot the virtual aperture width $VA$ as a function of flow ratio for both models as a heat map, with values ranging from $VA = w = 50$ µm (maroon) down to 0 µm (purple). For the numerical model, the second coordinate represents the sample flow rate $Q_s$ [130]. Two overlaid lines indicate $Re = 1$ (black dashes) and the experimental regime of a constant total flow rate of 40 µl/h (solid gray, with squares representing individual measurement conditions) well within the creeping flow regime. Overall, lower flow ratios $FR$ clearly correspond to better sample confinement (colder colors). At high sample flow rates or low flow ratios (upper right quadrant), the deviation between numerical and analytical models is moreover minimal. However, diffusion asserts itself at low sample flow rates and high flow ratios. This is most obviously apparent at the bottom of the plot, where diffusion washes out the rapid color progression seen in the analytical model. Thus, use of the analytical model has to be judicious, keeping the

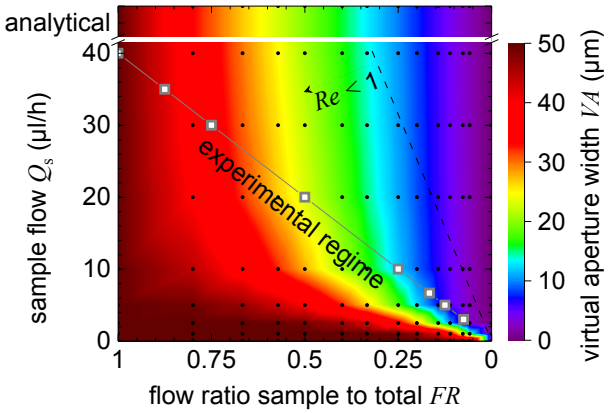


Figure 3.4: Color map of the virtual aperture width $VA$ (from low to high as purple to maroon) as a function of sample flow $Q_S$ and the flow ratio $FR$, as determined by numerical modeling for $w_{fc} = 75$ µm. The analytical model, independent of $Q_S$, is included at the top. The experimental regime of constant total flow is shown by gray squares. The flow regime of Reynolds number $Re < 1$ is indicated by the black dashed line and the arrow. Adapted with permission from [130].

employed flow regime in mind.

Figure 3.5a represents a section of the above color map along the gray line of the experimental regime, plotting $VA$ as a function of $FR$ for the analytical model (dotted line), the numerical ion model (orange crosses), and the numerical cell model (maroon circles) [130]. The deviation between the two modeling approaches can be more clearly observed here as compared to the heat map, with the relative deviation quantified as $RMSE = 17.6\%$. At the diffusion timescales investigated, cells should practically yield a nearly two-phase flow solution at the experimental condition, and thus serve as a basic validation of the numerical *versus* the analytical model. Indeed, the agreement is much better in this case, at $RMSE = 8.9\%$. This underestimation by the numerical cell model is likely due to my speculative formulation for $VA$ in the finite element model. The difference between cells and ions within the numerical regime, however, should be less sensitive to this factor. Therefore, the overall ~25% deviation between the two can serve as an approximate indicator of the effect size that may be expected from diffusion when subsequently looking at impedance cytometry performance.

Considering diffusion effects further, Figure 3.5b shows another section of the

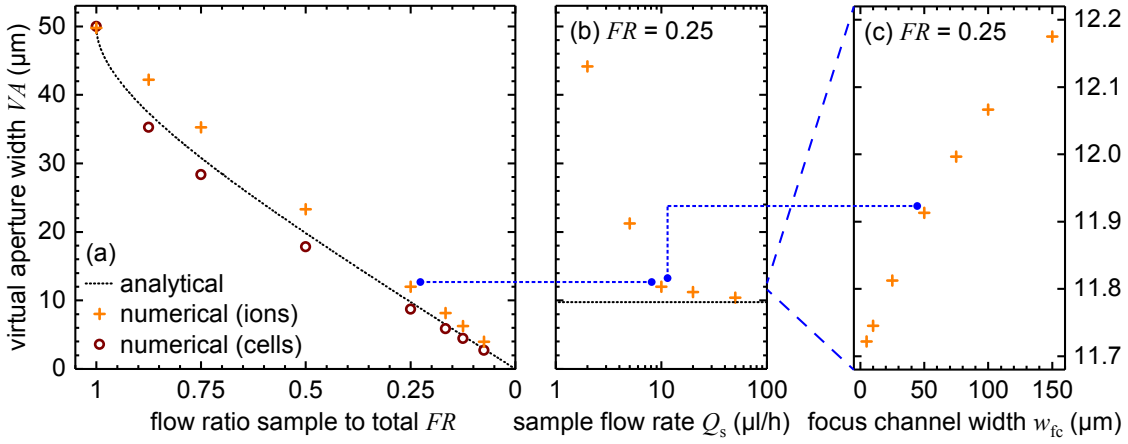


Figure 3.5: Hydrodynamic analytical (dotted line) and numerical (orange crosses) models revealing the dependence of the virtual aperture width $VA$ (a) on the flow ratio $FR$ in the experimental regime (constant total flow), with numerical results for slow-diffusing cells (maroon circles) also presented for comparison; (b) on the sample flow rate $Q_S$ for a representative, fixed $FR = 0.25$; (c) on the focus channel width $w_{fc}$ for a representative, fixed $FR = 0.25$. Adapted with permission from [130].

heat map, along a representative vertical line of constant $FR = 0.25$, thus showing $VA$ as a function of $Q_s$ [130]. As the latter increases, $VA$ rapidly decreases from its upper limit of $VA = w$ down to the lower analytical solution limit. The experimental value of $Q_s = 10$ µl/h at this flow ratio clearly falls onto the asymptotic approach, where an order-of-magnitude change in flow only effects minimal improvements in model agreement.

Finally, in Figure 3.5c, I explore geometric variations in focus channel width $w_{fc}$ on $VA$ at the same representative $FR = 0.25$ [130]. There is a clear positive correlation between the parameters; the scale of the $y$-axis, however, indicates that the effect size is marginal compared to what even a minor change in $FR$ can accomplish. Around the mean, the variation in $w_{fc}$ here is only $RMSE = 1.4\%$, which is below variations that can be expected from external interfering parameters on $FR$ such as syringe pump stepping. The small effect size here also bears comparison to that observed in the few other works that have considered flow focusing geometries, where changes in confluence angle altered $VA$ by up to 50% [131,132].

Before proceeding to analyze the fully coupled problem, a few purely electrodynamic considerations are of interest. In Figure 3.6, I first consider the dependence of the impedance signal $|\Delta Z|$ as a function of the applied electrical signal frequency [130]. The impedance response is plotted for a generic reference white blood cell (red circles; parameters from [140]), with variations considered here in diameter $\phi$ (yellow and blue triangles), membrane permittivity $\varepsilon_{\text{mem}}$ (green dashed and dash-dotted lines), and cytosol conductivity $\sigma_{\text{cyt}}$ (purple dashed and dash-dotted lines). This reveals three regimes with distinct sensitivity to cell size (around 90 kHz), membrane properties (0.9 MHz), and cytosol properties (20 MHz). The general behavior matches that expected from previous work – which has also shown how to compensate for the cross-talk of the size parameter into the other frequency regimes – with the specific frequency regimes particular to my device geometry [54,141]. I also find that other cell properties (membrane conductivity and cytosol permittivity) do not impact the signal response, again matching expectations. The major implication here is that a frequency of 100 kHz will be exclusively sensitive to cell size, independent of its internal structure or properties. Thus, at this frequency, cells and polystyrene particles can be treated equivalently, greatly simplifying device experiments without compromising the general nature of the conclusions.

Figure 3.7a–b presents the results from the coupled hydrodynamic and electrodynamic models both analytically (dotted lines) and numerically (symbols) [130]. Specifically, I plot the impedance signal $|\Delta Z|$ for $\phi = 6$ μm diameter particles and the population separation $\Delta\,|\Delta Z|$ between 10 μm and 6 μm diameter particles, both as a function of the flow ratio $FR$. The data overall clearly highlights the gains in performance that hydrodynamic focusing (*i.e.*, decreasing $FR$) can provide for impedance cytometry. These trends are also conserved in the membrane- and cytosol-sensitive frequency regimes (not shown).

When comparing between analytical and numerical models, however, there are obvious differences. In the weak focusing regime of $FR \geq 0.5$, the models agree reasonably

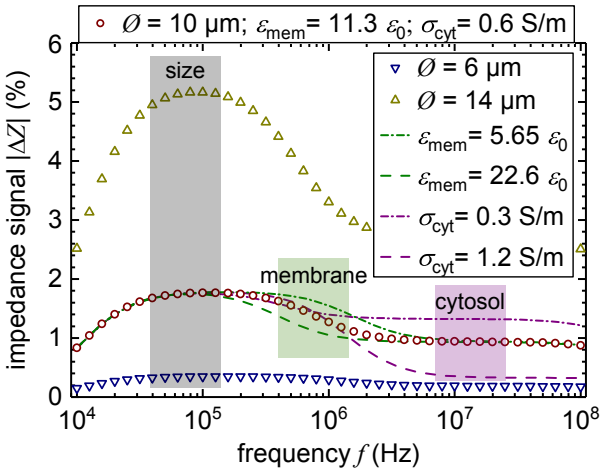


Figure 3.6: Impedance cytometry signals $|\Delta Z|$ from numerical modeling as a function of signal frequency $f$ for variations around the reference cell parameters (red squares) in terms of size $\phi$ (blue/yellow triangles), membrane permittivity $\varepsilon_{\mathrm{mem}}$ (green lines), and cytoplasm conductivity $\sigma_{\mathrm{cyt}}$ (purple lines). The resulting three frequency regimes are highlighted by overlaid colored bars. Adapted with permission from [130].

well, with $RMSE = 41\%$ for $\Delta\,|\Delta Z|$ combined with a matching trend. This contrasts with a corresponding value of 203% in the strong focusing regime. While the numerical model is already entering saturation in this regime, the analytical model continues to increase and saturates only once $VA < \phi$, where a further decrease in $VA$ also impacts the effective particle volume as discussed earlier in Subsection 3.1.2. The gain in sensitivity correspondingly decreases from up to tenfold in the analytical model down to 2.8-fold in the numerical one. Since model agreement without flow focusing validates the basic electrodynamic model, the large effect size has to be attributed to diffusion. This now bears comparison with the purely hydrodynamic results in Figure 3.5. The disagreement between models in that case is limited to around 20% – an order of magnitude less than seen here for low $FR$. Moreover, the deviation between hydrodynamic models only gradually changes with $FR$, unlike the relatively sharp change seen here.

To consider this further, in Figure 3.7c I plot the population separation $\Delta\,|\Delta Z|$ as a function of sample flow rate $Q_{\mathrm{s}}$ at an exemplary $FR = 0.25$ [130]. With increasing flow rate (and thus decreasing diffusion times, equating to a more well-defined $VA$), cytometry

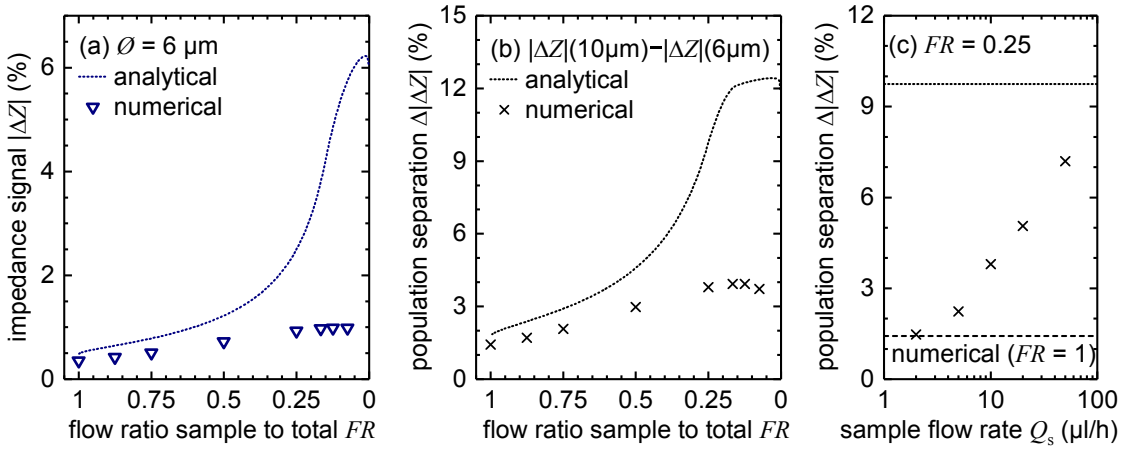


Figure 3.7: Analytical (dotted lines) and numerical (blue triangles, black crosses) models of impedance cytometry performance as a function of (a–b) hydrodynamic focusing in terms of the flow ratio $FR$ or of (c) sample flow rate $Q_s$ at a representative, fixed $FR = 0.25$. Performance is shown in terms of (a) impedance cytometry signals $|\Delta Z|$ for cells of diameter $\phi = 6$ µm and of (b–c) population separation $\Delta|\Delta Z|$ between $\phi = 10$ µm and 6 µm diameter cells. Adapted with permission from [130].

performance only gradually increases from the lower limit (where the timescales are long enough to allow for complete interdiffusion, equivalent to the numerical model in the absence of flow focusing) toward the upper limit from analytical modeling. While the basic positive correlation agrees with expectations, it again bears comparison to the similar results from hydrodynamic modeling in Figure 3.5. There, experimental conditions are within an asymptotic approach to the analytical limit; here, they do not even clear the half-way point.

Lastly, I consider the empty channel impedance $Z_{\text{empty}}$. On this parameter, both models show excellent agreement over the entire range of $FR$, with only $RMSE = 5.6\%$ deviation between analytical and numerical results. The empty channel impedance, of course, is intimately (and inversely) linked to the effective electrical interaction volume, and thus to $VA$. At the same time, the effect size from diffusion here is even less than predicted from the hydrodynamic model. Only when a particle or cell is present, however, I find that diffusion significantly exceeds those expectations with regards to impedance cytometry, especially in the regime of strong focusing.

Looking at the model assumptions, the intriguing implication of this result is that the Equation 3.3 serves as a good approximation of hydrodynamic focusing effects in terms of $VA$. For impedance cytometry, though, the dominant parameters are clearly not accounted for correctly. To investigate this further, I construct a partial least squares regression model from all available data in OriginPro. This multivariate analysis approach attempts to predict an output (here, $\Delta\,|\Delta Z|$) based on multiple inputs (here, the fit variables for the concentration profiles) without prior knowledge of their relation. In constructing this model, one quantifiable result is the relative importance of the various input variables. This is predicted as $C_{\mathrm{offset}} > s_{\mathrm{p}} \approx C_{\mathrm{amp}} > s_{\mathrm{s}}$, implying for instance that a high offset value carries a larger penalty regarding impedance cytometry performance than my equation accounts for. The dataset is too small and not properly designed for deeper multivariate analysis, however.

### 3.1.6 Device Experiments

The theoretical considerations of the last Subsection are only truly valuable when assessed against experimental results from my devices. I illustrate the operation and data analysis of these in Figure 3.8 [130]. Exemplary impedance signal $|\Delta Z|$ data of $\phi = 6$ µm polystyrene particles for the lowest investigated flow ratio $FR = 0.875$ is shown in Figure 3.8a after the MATLAB processing of the raw data as described in Subsection 3.1.4. The data reveal a highly populated background around $|\Delta Z| = 0$, as well as distinct datapoints corresponding to passage of particles through the detector. Clustering of these signals into a distinct band around $|\Delta Z| = 0.16\%$ is already apparent visually. Transformation of these data into the histogram in Figure 3.8b, and fitting of the peak with a Gaussian distribution, easily quantifies this population average as well as the corresponding spread $\delta = 0.02\%$. Repeating such experiments with both particle sizes and for multiple flow ratios yields data like that in Figure 3.8c for each of the devices investigated. This plot shows the population averages and spreads from

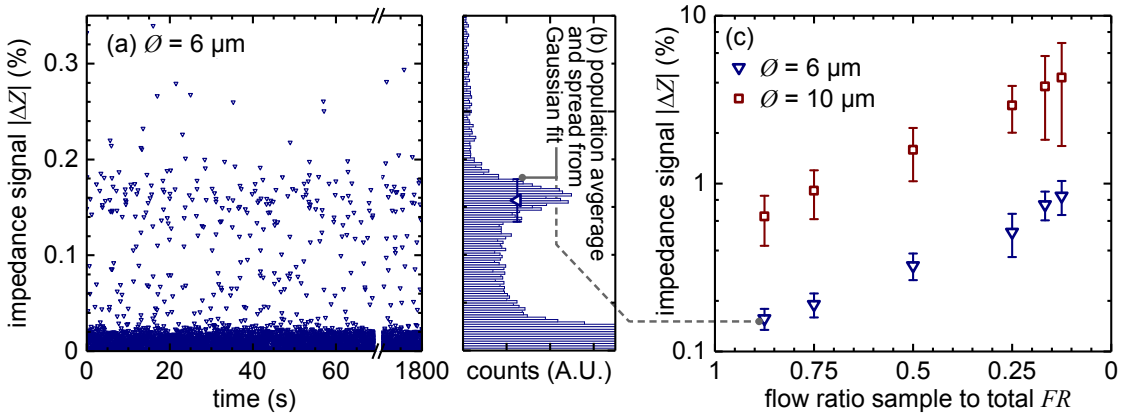


Figure 3.8: (a) Representative processed experimental impedance cytometry signals $|\Delta Z|$ from $\phi = 6$ µm diameter particles at the lowest investigated $FR = 0.875$. (b) Corresponding histogram for the entire 30-minute dataset, where population average $|\Delta Z|$ and spread $\delta$ (overlaid blue triangle and error bar, respectively) can be determined from Gaussian fitting between the first and second minima. (c) $|\Delta Z|$ and $\delta$ (symbols and error bars, respectively) for both $\phi = 6$ µm (blue triangles) and 10 µm (red squares) particle populations for a range of flow ratios $FR$ from a representative device. Adapted with permission from [130].

the Gaussian histogram fits – on a logarithmic $y$-axis to accommodate both $\phi = 6$ µm and 10 µm particles – as a function of flow ratio $FR$. The significant five-fold gain in impedance signals with hydrodynamic focusing becomes immediately apparent for both populations, which remain clearly separated. This experimentally validates the overall approach. Single-device results, in spite of an event count typically exceeding 1,000 for each population average, can still suffer from outliers such as the large population spreads $\delta$ occurring here with the 10 µm diameter population at the lowest $FR$. Thus, most of my analysis going forward considers data and trends across all devices and conditions.

One point of note regarding the analysis is that while the Gaussian fitting serves as a good first-order approximation, it suffers from limitations both from experimental and theoretical perspectives. First, the data clearly displays outliers in the range of $|\Delta Z| = 0.3\%$, which can be attributed to rare coincident detection of two particles. Second, the data also displays a strong negative skew – while some of this can be attributed to the tail ends of the background noise distribution, a significant part of it cannot. This leads to the third point, which is that a Gaussian distribution is not even expected from

underlying factors in the experiments. These are as follows: The polystyrene particles themselves have an inherent distribution in size – assuming it is normal in terms of diameter as implied by the manufacturer, this leads to a positive skew in impedance signals (as these are proportional to volume); while out-of-plane particle positioning in the channel likely follows a flat distribution, this would yield a negative skew due to the larger signals by those closer to the electrodes; most critically, the transfer function of the LCR meter – with measurement time on a similar timescale as particle transit time – introduces a dominant negative skew.

Keeping these limitations in mind, I proceed to compare theory and experiments in Figure 3.9a, specifically regarding impedance signals $|\Delta Z|$ for $\phi = 6$ µm diameter particles [130]. Experimental data is plotted for each device (symbols), alongside both analytical (dotted line) and numerical (dashed line) models. To emphasize trends, the $y$-axes are scaled by a factor of 3, which I will discuss further below. Considering just the experimental data, these match the observations in Figure 3.8c, revealing an increase in signals from $|\Delta Z| = 0.17\%$ up to $0.87\%$ at a low $FR = 0.125$.

Comparing models and experiments in terms of signal magnitude shows that the former exceed the latter by a factor of about 3 ($\pm 0.5$ depending on the model) in the weak focusing regime, in line with the axis scaling employed. I attribute a large part of this to the LCR meter transfer function mentioned earlier: Besides introducing negative skew to the signal distribution, having the measurement and particle transit on similar timescales (*cf.* Subsection 3.1.4) also causes transient averaging. With transient numerical simulations, I estimate this to account for a factor of approximately 1.7. The remainder of the discrepancy is likely due to parasitic effects primarily from the unshielded on-chip connection traces and contact pads. Moreover, the Helmholtz model potentially underestimates the ionic double layer capacitance.

The trends in the experimental and model data, however, allow for intriguing conclusions – specifically, that the experimental data appear to follow the analytical

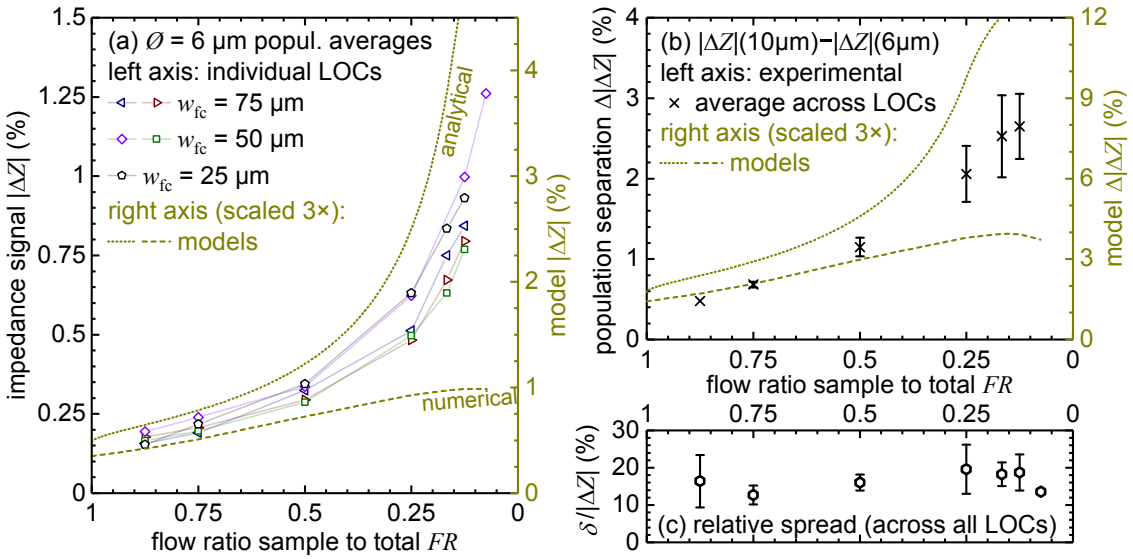


Figure 3.9: (a) (left axis) Experimental impedance cytometry population averages $|\Delta Z|$ of $\phi = 6$ µm diameter particles (symbols) from all LOCs as a function of the flow ratio $FR$. Each data point here represents an average of at least 1,000 particle passages. Connecting solid lines are visual guides only. (right axis) Corresponding analytical (dotted) and numerical (dashed) model predictions are overlaid, scaled by a factor of 3 to highlight trends. (b) Population separation $\Delta\,|\Delta Z|$ between $\phi = 6$ µm and 10 µm as an average across LOCs (crosses; left axis), with corresponding models overlaid scaled by a factor of 3 (lines; right axis). Error bars represent standard errors of the mean. (c) Average relative population spread $\delta/|\Delta Z|$ corresponding to the population averages in a across all devices (hexagons) shown separately for clarity. Error bars represent standard errors of the mean. Adapted with permission from [130].

trend somewhat more closely than the numerical one for strong focusing. It appears that while the analytical model provides an upper bound to experimental impedance cytometry performance, the numerical model provides a lower one. It is likely neglected higher-order effects, such as the direct particle–flow field interaction, that ultimately account for an experimental trend inbetween the limiting model cases.

In Figure 3.9b I present the aggregate data on population separation $\Delta\,|\Delta Z|$ across all devices as a function of flow ratio $FR$ [130]. Like the previous plot in $|\Delta Z|$, both models are overlaid with a separate $y$-axis scaled by a factor of 3. Experiments again reveal a robust increase from $\Delta\,|\Delta Z| = 0.48\%$ to 2.65%, with a trend falling inbetween that of the numerical and analytical models. Indeed, the interpretation follows practically the same

lines as that above, providing additional validation in the form of an independent set of data. Both results showcase interesting differences between experiments and theory, and moreover establish the benefits of employing hydrodynamic focusing with impedance cytometry in terms of sensitivity.

The population spreads $\delta$ in Figure 3.9c correspond to the averages from (a), shown here separately across all devices for clarity and to highlight other important characteristics [130]. Specifically, displayed in relative terms as $\delta/|\Delta Z|$, they appear to be constant and *FR*-independent at a value of 16%. I statistically confirm this with linear regression model ANOVA and its insignificant $p$-value of 0.15. This helps in attributing the observed population spreads to various phenomena. An *FR*-dependence would point to flow-related phenomena such as syringe pump stepping, where very low sample flow rates $Q_s$ at the lowest *FR* would be expected to increase noise levels. Similarly, increasing absolute impedance $Z$ with decreasing flow ratio could introduce additional measurement noise. Neither appears to be the case. Instead, two inherent geometrical factors appear to dominate: First, the intrinsic particle size distribution, specified by the manufacturer as 22% in terms of volume. Second, the variability in out-of-plane particle positioning. For a similar design, Gawad *et al.* predict around $\delta/|\Delta Z| = 30\%$ for $\phi = 10$ µm diameter particles [54]. Thus, my particle spread values in these experiments compare quite favorably to the underlying physical constraints. I further point out that while the spreads are significant, most of the broader conclusions here are based on the population averages and their much smaller related standard errors ($< 5\%$).

Considering observed variability, another factor that proves interesting to consider is inter-device variability such as seen inFigure 3.9a. While the trends are similar, I still find a relative $RMSE = 9.5\%$ across all flow ratios *FR*. This could point to one of the obvious differences between them – focus channel width $w_{fc}$, the geometric parameter of interest. Although modeling predicted minimal impact, this still bears experimental consideration. Thus, separately for each *FR* condition, I analyze $|\Delta Z|$ as a function of $w_{fc}$.

Employing linear regression ANOVA, I do not find a significant trend, with the average $p$-value (across all $FR$) at $\bar{p}\,(w_{\mathrm{fc}}) = 0.40$. This is in line with the models, but leaves the observed device variability unaccounted for.

Diffusion-related parameters are natural next candidates to consider, based on the observations thus far. Of particular importance in this regard is the distance between the flow focusing junction and the measurement electrodes. A longer distance equals a longer diffusion time and thus a less well defined $VA$. Although designed to be constant at $d = 170$ µm, manual alignment of PDMS and glass yields some variability in this regard within the 10% tolerance criterion followed overall. Interestingly, I do not observe a correlation directly between $d$ and impedance cytometry performance in terms of $|\Delta Z|$; instead, I find one in terms of a modified distance $d' = d + \frac{1}{2}w_{\mathrm{fc}}$, *i.e.* measured from the center of the focus junction. This is illustrated in Figure 3.10, where population averages are plotted as a function of this parameter for each flow ratio $FR$ [130]. A linear trend with $|\Delta Z|$ decreasing toward larger $d'$ is clearly apparent particularly in the strong focusing (low $FR$) regime, where diffusion effects would be most pronounced due to the narrower $VA$. Employing the same type of ANOVA as above, I confirm this statistically. The average $\bar{p}\,(d') = 0.06.$ is slightly above the traditional significance level; however, $d'$ is the only parameter where $p$-values are consistently less than 0.05 for $FR < 0.75$. The other parameters considered are $\bar{p}\,(d) = 0.22$, $\bar{p}\,(d + w_{\mathrm{fc}}) = 0.13$, and $\bar{p}\,(h) = 0.93$. The latter, variable due to inhomogeneous photoresist thickness in spin-coating, could also have been expected to impact cytometry performance by altering the electrical interaction volume as well as changing flow behavior.

Finding the center-to-center distance $d'$ (rather than other distance parameters) to play a role aligns with the inertial effects described in previous work on hydrodynamic focusing geometry [131,132]. Such effects can be expected to be most prominent in the region of highest flow velocity, *i.e.* the channel center. The finding also implies that the focus channel width $w_{\mathrm{fc}}$ does in fact play a role in cytometry performance, albeit a minor

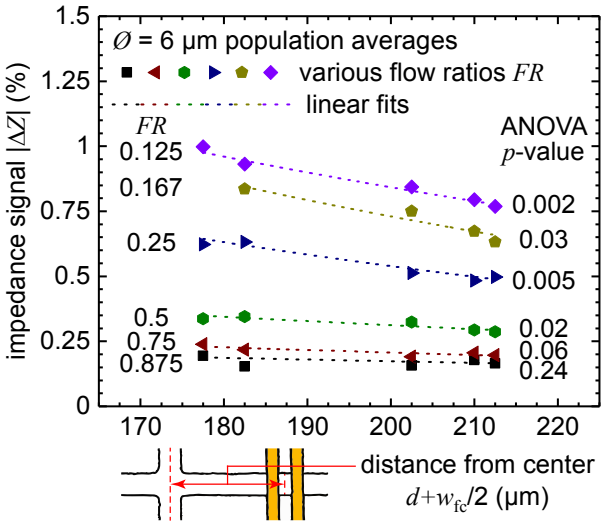


Figure 3.10: Experimental impedance cytometry population averages $|\Delta Z|$ of $\phi = 6$ µm diameter particles recorded using different LOCs as a function of the distance $d' = d + \frac{1}{2} w_{\mathrm{fc}}$. The geometrical parameter is highlighted in the schematic drawing of the device layout. $FR$ is listed on the left for each set of data and decreases from 0.875 (black squares) to 0.125 (purple diamonds). Linear fits to the data are shown as dotted lines, and $p$-values of corresponding ANOVA models are listed on the right. Adapted with permission from [130].

one. The general correlation of distance with $|\Delta Z|$ aligns with the other findings in my work on the importance of diffusion in cytometry and further reinforces this notion. I find that the impact of ionic diffusion in microfluidics generally seems to be underappreciated, with only few works on impedimetric systems devoting attention to this phenomenon [126,145]. Indeed, even considering the traditional measure of the importance of diffusion over convection – the Péclet number $Pe = 2\,(Q_{\mathrm{s}} + Q_{\mathrm{f}})\,/(w + h)\,D_{\mathrm{ion}} = 189$ – leads to the expectation of negligible diffusion effects, being much larger than 1. In the systems interplay between hydrodynamic focusing and impedance cytometry, however, my work shows that this is clearly a misplaced assumption.

### 3.1.7 Synopsis

I presented the first in-depth study of systems interplay between in-plane hydrodynamic focusing and impedance cytometry. From a performance standpoint, I demonstrated

up to five-fold improvement in size sensitivity with DI water sheath flows. I explored both analytical and numerical models of the system to compare the experimental data to. The models predicted negligible impact of the focus channel width on performance, but the numerical model revealed significant impact of diffusion on impedance cytometry performance in spite of a high Péclet number. I found experimental trends to actually fall between the two modeling approaches, which likely serve as upper and lower limits. Nevertheless, I observed the impact of diffusion experimentally in the dependence of cytometry performance on the distance from the focusing junction – specifically its center, likely related to inertial flow effects.

## 3.2 Reagent-Free Osmotic Lysis of Erythrocytes

The use of various reagents in existing white blood cell counters to eliminate the high red blood cell background, and the associated downsides for a point-of-care device in terms of packaging, have been covered in Subsection 1.3.3. An appealing alternative approach to erythrocyte lysis relies simply on pure water – a compound that is cheap, quite stable, and can even be produced on-site in resource-poor environments by distillation. This type of osmotic lysis is well-accepted for benchtop flow cytometry [146]. It relies on the higher resilience of white blood cells compared to red blood cells in the presence of a strong osmotic pressure gradient $\Delta P$. In bulk solution, while practically all erythrocytes are ruptured after an exposure time of $t = 30$ s, leukocytes can survive up to $t = 120$ s in pure water [147].

A few researchers have previously studied this approach with a focus on erythrocyte lysis [148,149] and on recovery of and potential changes in leukocytes [150]. In the former, both Sethu *et al.* and Zhan *et al.* employ simple PDMS-on-glass microfluidics, wherein whole blood and lysis agent combine at a junction and then mix by diffusion as the flow continues through a serpentine channel, with lysis efficiency monitored optically. Both groups find lysis efficiency to depend mainly on the exposure time $t$, with complete lysis

at $t = 15$ s. In terms of the osmotic pressure gradient $\Delta P$, both demonstrate an increase in the required lysis time depending on the ratio of water to blood flow rates – the increase is observed for ratios of less than 5:1 (Sethu *et al.*) or less than 10:1 (Zhan *et al.*). In later work, Sethu *et al.* confirm that osmotic microfluidic lysis is advantageous over bulk reagent-based lysis both in leukocyte recovery and cell activation, employing a device modified to enhance mixing of solutions by convection.

Although some critical aspects of microfluidic osmotic lysis have been characterized, integration with impedance cytometry has not been studied. With these integrated systems, two opposing optimization criteria come into play: Maximizing water flow to achieve a sufficient osmotic pressure gradient for efficient erythrocyte lysis, yet at the same time minimizing it to keep the absolute measured impedance $Z$ low. Although the solution conductivity $\sigma_{\text{med}}$ is a negligible factor in the models for $|\Delta Z|$ presented in Section 3.1, high $Z$ are inherently more difficult to measure. My work thus aims to study the relevant sub-system interplay by considering a range of exposure times and osmotic pressure gradients.

### 3.2.1 Design Overview

My design, shown in Figure 3.11, employs co-planar microelectrodes at a distance $L =$ 70 mm, 135 mm, or 200 mm downstream from a junction, where the blood sample stream (flow rate $Q_{\text{s}}$) is met perpendicularly by two streams of DI water (combined flow rate $Q_{\text{l}}$). To minimize clogging, the channel width is chosen as $w = 120$ µm, except in the measurement region, where it reduces to 50 µm to enhance sensitivity. The device dimensions are otherwise identical to those in Section 3.1. The same applies to the flow – I conduct all experiments under the condition of $Q_{\text{s}} + Q_{\text{l}} = 40$ µl/h. At this total flow rate, the three lysis channel lengths provide lysis exposure times of $t = 15$ s, 30 s, and 45 s. While laminar flow does not allow for rapid mixing, the interdiffusion time ($\sim w^2/8D_{\text{ion}} = 1$ s) still remains short compared to these lysis timescales. By adjusting the

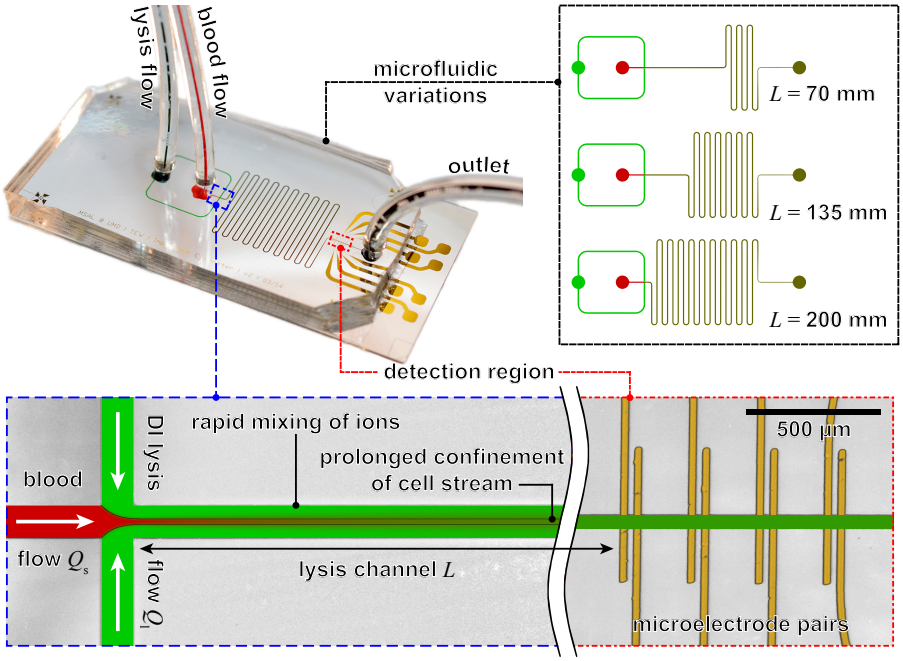


Figure 3.11: Photograph of my device. Right: Illustration of the microfluidic channel variations investigated in this study. Bottom: Micrographs of lysis inflow and impedance measurement regions, with overlaid hydrodynamic finite element model (DI water lysis flow (green) and blood sample flow (red; cells and ions) at $FR = 0.25$). Adapted with permission from [151].

ratio of lysis to blood flow rates, I can adjust the osmotic pressure gradient $\Delta P$. Analogous to Equation 3.1, I quantify this in terms of $FR = Q_s/(Q_s + Q_l)$. I can also set $\Delta P = 0$ by replacing the DI water lysis flow with PBS. Thus, I am exploring two independent key parameters for osmotic lysis with my design.

### 3.2.2 Experimental Methods

For device fabrication, I refer to Subsection 3.1.3, with the only difference being in the utilization of the photomask 6.4 shown in Appendix A: Photomasks to pattern the microfluidic mold (although the mask includes hydrodynamic focusing features, the respective channel inlet is not opened up in this study, rendering them inert). Instrumentation is similarly described therein. The lysis flow consists of DI water with resistivity > 17 MΩ cm, or 1× PBS for negative controls. For the sample flow, I obtained

heparinized whole blood from a blood bank, filtered through a 70 μm mesh size cell strainer prior to experiments. While in the particle experiments of the previous Section it was possible to employ sucrose for density matching, such an approach would cause cell damage from hyperosmotic conditions as well as decrease the achievable osmotic pressure gradient for any given flow ratio. Thus, cell sedimentation in the vertically mounted syringes becomes a concern, leading to hyper-concentration of cells. To circumvent this, I dilute the blood 1:3 with commercial human serum and supplement the solution with 5 mM ethylenediaminetetraacetic acid.

I again control flows and record data with custom graphic user interfaces developed in LabView. For each flow condition, the experiments run for 0.5 to 2 hours to ensure sufficient sample sizes. I analyze the data in MATLAB, employing the code in Appendix C: MATLAB Code. Due to the signal approaching (or, for some conditions, reaching) saturation, the algorithm utilized with particle experiments – which assumes sparse peaks – is not capable of determining the background signal $Z_{\text{empty}}$ here. Instead, an image erosion algorithm derives the signal floor, subsequently smoothed by a moving average filter. Using this background to calculate $|\Delta Z|$, I detect signal peaks with a simple built-in algorithm. Then, I employ a scaled version of the analytical electrodynamic model from Subsection 3.1.2 to express data in terms of equivalent spherical diameter $\phi$ instead of $|\Delta Z|$. Histograms are obtained and fitted as previously described, except I normalize these to the total number of counts to account for the unknown input cell density from settling.

### 3.2.3 Impact of Flow Ratio and Lysis Time on Lysis Efficiency

In Figure 3.12, I illustrate the data analysis with two exemplary signal distributions recorded in my devices, displayed both in terms of measured impedance signals $|\Delta Z|$ as well as in terms of the model-derived cell diameter $\phi$ [151]. Both experimental conditions shown exhibit clear Gaussian distributions (dotted lines) that can be represented in the

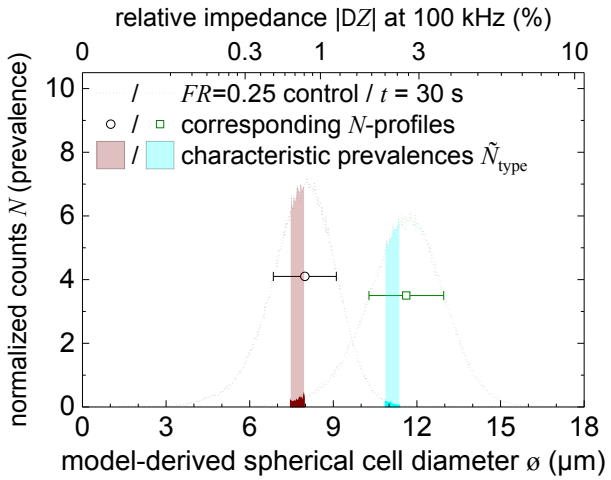


Figure 3.12: Exemplary impedance distributions in terms of $|\Delta Z|$ or $\phi$ (dotted lines), normalized by total counts. Fitted Gaussian $N$-profiles (symbols and error bars) are overlaid, and the derivation of characteristic cell size prevalences $\tilde{N}$ (shaded) is illustrated. Reproduced with permission from [151].

form of an $N$-profile (symbols and error bars) – the population average and spread obtained from fitting the data. A second relevant parameter is the characteristic prevalence $\tilde{N}$, used to describe the prevalence of erythrocyte-characteristic and leukocyte-characteristic cell sizes in a given histogram and defined as:

$$\tilde{N}_{\text{type}} = \sum_{\phi_{\text{type}} \pm \sigma_{\text{type}}} N \tag{3.4}$$

Illustrated with red and blue shaded overlays for red and white blood cell types in the figure, it quantifies the sum over the histogram counts $N$ within a standard error of the respective characteristic cell size.

Considering $N$-profiles first, I plot these as a function of the flow ratio $FR$ in Figure 3.13 [151]. The graph shows data for all three lysis times (colored triangles and squares) as well as a negative control utilizing buffer instead of water (black circles). The difference between osmotic lysis solutions and the negative control is the most apparent feature of this figure. It further contains many more facile conclusions regarding different regimes. The regime of flow ratios $FR \leq 0.25$ holds the central conclusion: Here,

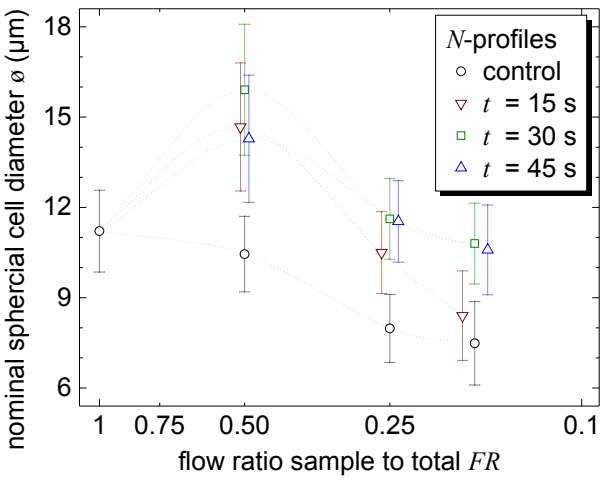


Figure 3.13: Signal distributions in terms of $\phi$ for a range of $FR$ and $t$ (colored squares and triangles), as well as negative control (black circles). Dotted lines are shown for guidance only. Reproduced with permission from [151].

the control saturates at signals corresponding to an equivalent spherical cell radius or $\phi = 7.8 \pm 0.2$ µm for flow ratios $FR \leq 0.25$. Allowing for their distinctly non-spherical shape, this size is in close agreement with the size of erythrocytes [45]. It is also in sharp contrast to active osmotic lysis with exposure times of $t \geq 30$ s. At the high osmotic pressure gradients in this flow regime, combined with the long exposure times, signals saturate at $\phi = 11.2 \pm 0.2$ µm, matching expected leukocyte diameters of 10–12 µm. The stark difference relative to the control, combined with the saturating behavior, appears to confirm that the maximum erythrocyte lysis efficiency is achieved in this regime, in general agreement with previous work [148–150].

Outside this regime, the control bears a further look. The "lysis" flow rate here does not affect the osmotic pressure gradient which remains constant at $\Delta P = 0$, yet the observations clearly deviate from the saturation value at low flow ratios. However, the decreasing flow ratio here does provide further sample dilution. Without such dilution at low flow ratios, I hypothesize that the high abundance of red blood cells causes measurement overload with multiple cells within the detection volume simultaneously, leading to unrealistically high observed values of $\phi$. This applies to conditions of $FR = 1$ or lysis time $t = 0$ in general.

For the flow ratio $FR = 0.5$, osmotic lysis at all exposure times shows a sharp increase to $\phi = 15$ µm, while the control already trends to lower values. Thus, though signal saturation is clearly still a factor, I believe that the low osmotic pressure gradient $\Delta P$ here exacerbates the situation by causing significant cell swelling while being insufficient to cause rupture. This is further supported by the significantly larger population spreads. Lastly, at the shortest lysis exposure time of $t = 15$ s, saturation is not achieved even at at the lowest flow ratio, with the signal strongly trending toward that of the control, and thus a signal dominated by erythrocyte-characteristic cell sizes. Since the osmotic pressure gradient appears to be sufficient for lysis, it seems the exposure time is not, leaving a significant number of erythrocytes intact and thus leading them to again ultimately dominate. This is broadly in line with previous literature reporting $t \geq 15$ s as the minimum lysis time [148,149].

While both for $t = 15$ s and in the $FR = 0.5$ case, erythrocyte lysis is not achieved, I need to emphasize the differing underlying hypotheses. This mechanistic insight is importantly a direct result of the on-chip monitoring capabilities – optical lysis monitoring *via* hemoglobin release as employed by Zhan *et al.*, for instance, would likely not be able to differentiate these cases [149]. I also need to note, however, that my experimental design suffers from a lack of independent (optical) validation. My hypotheses are thus based on combining the previous observations by Zhan *et al.* and Sethu *et al.* with my impedimetric observations of differing signal behavior at different lysis times and an overall non-linearity in terms of flow ratio (thus ruling out artifacts from changes in absolute impedance $Z$).

In Figure 3.14, I consider the alternative analysis approach mentioned earlier, employing the characteristic prevalences $\tilde{N}$ of red and white blood cell-equivalent sizes in the measured signal distributions [151]. Specifically, I plot the differential $\tilde{N}_{\mathrm{WBC}} - \tilde{N}_{\mathrm{RBC}}$ as a function of the flow ratio between lysis and sample flows for the same conditions as considered previously. This analysis yields positive values when white blood cell-

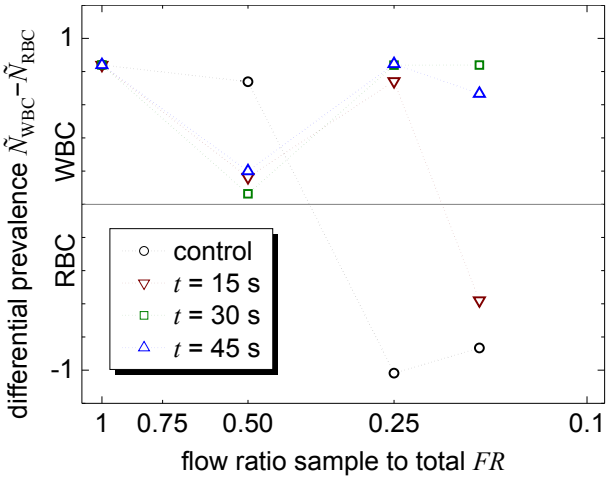


Figure 3.14: Differential prevalence of white- *vs.* red blood cell characteristic sizes for a range of $FR$ and $t$ (colored squares and triangles), as well as negative control (black circles). Dotted lines are shown for guidance only. Reproduced with permission from [151].

equivalent signals dominate strongly over red blood cell-equivalent ones, and *vice versa*. The trends observed here agree with those in Figure 3.13, corroborating the conclusions. The supposedly white blood cell-dominated signal for $t = 0$ or a flow ratio of 1 can be attributed to the saturation artifact. For $t = 15$ s, incomplete lysis is again in evidence, as is partial lysis at a flow ratio $FR = 0.5$. In the regime of high lysis times $t > 15$ s and low flow ratios $FR < 0.5$, leukocyte-characteristic signals dominate strongly, in sharp contrast to the erythrocyte-characteristic signals in the control. To compare these two, the ratio rather than the difference between characteristic prevalences $\tilde{N}$ provides a reasonable approach. Specifically, I can derive a lysis efficacy as:

$$1 - \left.\frac{\left(\tilde{N}_{\mathrm{RBC}}/\tilde{N}_{\mathrm{WBC}}\right)_{t\geq 30\,\mathrm{s}}}{\left(\tilde{N}_{\mathrm{RBC}}/\tilde{N}_{\mathrm{WBC}}\right)_{\mathrm{control}}}\right|_{FR\leq 0.25} = 99.92\% \tag{3.5}$$

This considers how common erythrocyte-characteristic signals are compared to white blood cell-characteristic ones with lysis as compared to the control, and exceeds the 99.5% criterion typically employed for quantifying successful erythrocyte lysis [148].

### 3.2.4 Synopsis

I explored the parameter space for osmotic lysis of erythrocytes when integrated with impedance cytometry. I identified the minimum requisite lysis time and osmotic pressure gradient to eliminate their dominant background signal in white blood cell measurements. The impedance measurements furthermore directly reflected distinct mechanisms when either both parameters or just the lysis time are insufficient. Within the lysis regime, I found osmotic lysis of red blood cells to be highly efficient.

## 3.3 Chapter Summary

In this Chapter, I have explored the integration of critical sub-systems needed for white blood cell counting: impedance cytometry, hydrodynamic focusing, and osmotic lysis. My study of the former two has highlighted the potential for an up to 5-fold improvement in sensitivity by employing DI water sheath flows to provide a virtual (rather than physical) aperture. While critical, the novelty of my work lies less in this result than in the breadth and depth that I have considered systems interplay in. I have constructed the first integrated analytical and numerical models for impedance cytometry with hydrodynamic focusing. In considering discrepancies between them, as well as with experimental results, I have shed light on the importance of diffusion phenomena in this system despite its large ($> 100$) Péclet number. While adversely affecting performance in this case, diffusion is critical for osmotic lysis of erythrocytes. I have demonstrated that for a regime of sufficient osmotic pressure gradient and exposure time, DI water is over 99.9% effective in on-chip red blood cell lysis. By studying the available parameter space, I have identified different modes of lysis failure when the necessary conditions are not met, and importantly demonstrated that osmotic lysis does not interfere with impedance cytometry. Overall, I have thus shown that the sub-systems are inherently compatible, a

critical prerequisite for further integration as pursued in Chapter 4.

# Chapter 4

## Development of Integrated Clozapine Sensor & White Blood Cell Counter

With clozapine sensing addressed in Chapter 2, and Chapter 3 exploring the sub-system compatibility between impedance cytometry and hydrodynamic focusing or osmotic lysis, the overall microsystem integration for concurrent clozapine and white blood cell monitoring remains. Two broad strategies are available, each with potential advantages and pitfalls: First, copying typical laboratory procedures by applying blood/plasma separation to connect the cellular/acellular sensing modalities in parallel. Second, integration of both sensors in series, with the clozapine measurement conducted directly in whole blood. The latter approach yields a simpler and thus ultimately more robust microfluidic device; the former provides the electrochemical sensor with a less complex matrix.

In this Chapter, I explore both approaches for overcoming remaining challenges in handling whole blood samples for concurrent cellular/acellular sensing. In Section 4.1, I study plasma skimming as a means to provide blood/plasma separation, with a label-free immunoassay serving as a proof-of-concept case study. Although the approach is not new, this is its first application to a true whole-blood sensor. With limitations outweighing benefits, I proceed to implement the series-type systems integration in Section 4.2. I demonstrate that this fully integrated device is indeed capable of concurrent clozapine and white blood cell analysis, a significant step toward point-of-care monitoring of clozapine treatment in schizophrenia.

## 4.1 Evaluation of Plasma Skimming for Blood/Plasma Separation in a Proof-of-Concept Immunoassay

As mentioned in Subsection 1.3.4, plasma skimming has been presented as a lab-on-a-chip blood/plasma separation approach with a unique combination of advantages: It relies solely on hydrodynamic forces, it does not adulterate or dilute either fraction of the sample, it can operate continuously, it is capable of handling whole blood, and it has successfully been implemented in a protein biosensor [78]. Other approaches tend to rely on external forces (centrifugation), are not capable of continuous flow (sedimentation), or require dilute blood samples (microposts). Especially the latter two capabilities are critical features for concurrent clozapine and white blood cell monitoring, however, due to the very nature of cytometry relying on a continuous flow of blood cells, and clozapine already being a low-concentration analyte (dilution therefore being counterproductive).

Plasma skimming relies on a combination of biophysical effects observed in the microvasculature: The Zweifach–Fung effect (at bifurcations, cells will follow the branch with the higher flow rate), the Fahraeus effect (the apparent cellular fraction of blood is lower in a capillary than in a large vessel), and the cell distribution within capillaries (red blood cells favor the center of the flow, with white blood cells favoring vicinity to the walls) [152–155]. While these phenomena are not fully understood, they can be replicated in microfluidics. Combined with laminar flow effects, they allow for the controlled "skimming" of the wall-adjacent cell-free layer of the blood stream through side channels that can exceed the dimensions of the cells themselves as initially demonstrated by Yang *et al.* [155]. The only requirement is that the flow rate $Q$ through the main channel needs to be at least six-fold higher than through those side channels. This flow rate condition is most readily understood when considering the streamlines that the cells are traveling on as illustrated in Figure 4.1a. Here, with the top channel flow rate four times higher than the bottom one, only cells (II) on streamlines below the critical one (III) can enter the low

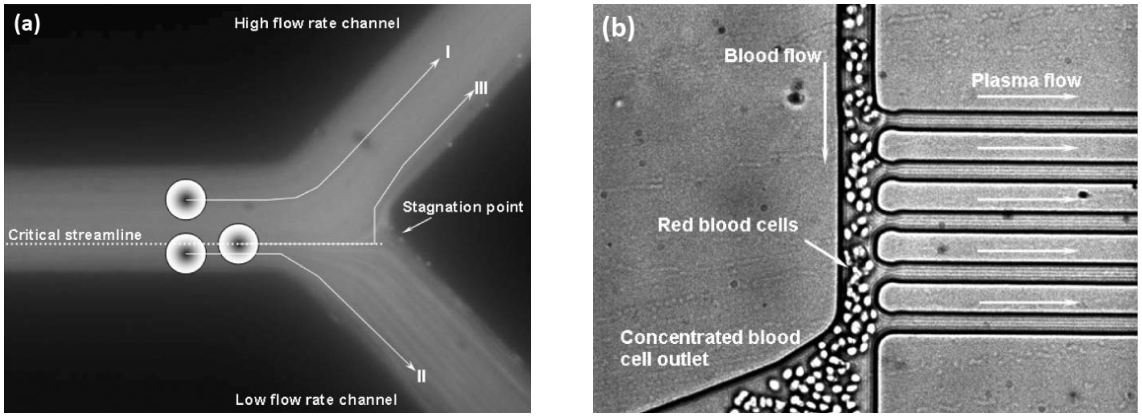


Figure 4.1: Plasma skimming. (a) Illustration of the critical streamline, where streamlines above (I) enter the high flow rate channel, and only those below (II) the low flow rate one. (b) Photograph of the blood plasma separation region in a plasma skimming device during infusion of defibrinated sheep blood (36% hematocrit) through the whole blood inlet (top). Reproduced with permission from [155].

flow rate channel. As the ratio between flows increases further, the critical streamline moves even closer toward the wall until – due to their finite diameter – no cells can occupy lower streamlines.

Since flow rates are related to fluidic resistances *via* pressure as $P = QR$, a flow ratio requirement of $Q_{\text{cells}}/Q_{\text{plasma}} \geq 7$ directly translates to $R_{\text{cells}}/R_{\text{plasma}} \geq 7$ for an infusion-type flow. The necessary conditions for plasma skimming can thus be satisfied solely by designing the channel geometry (height $h$, width $w$, length $L$) to provide the necessary fluidic resistances [155]:

$$R = \frac{12\mu L}{wh^3}\left(1 - \frac{192h}{\pi^5 w}\sum_{n=0}^{\infty}\frac{\tanh\left(\frac{\pi(2n+1)w}{2h}\right)}{(2n+1)^5}\right)^{-1} \tag{4.1}$$

Obviously, the flow condition also limits the plasma recovery efficiency of such a single-channel approach. Therefore, a fluidic network with multiple bifurcations such as the one in Figure 4.1b is typically employed, where the aforementioned conditions are met at each network node [79,155]. Due to the symmetry between the pressure equation and Ohm's law $U = IR$, electrical circuit simulation tools can be employed to derive the

relevant solution and design.

Upon closer examination, the literature on plasma skimming also offers two limitations: The initial study by Yang *et al.* utilizes defibrinated sheep blood, wherein cell sizes and flow properties can differ from human blood, and experimental results are only presented up to a hematocrit level of 36%, well below the 45–50% typical in humans [155]. The biosensor application study by Fan *et al.* employs human blood samples, but diluted almost 10-fold upon collection [79]. Thus, while plasma skimming appears promising to facilitate concurrent cellular/acellular sensing, a validation study for whole human blood is initially called for. I choose to carry this out in a proof-of-concept immunoassay – while I ultimately aim at an electrochemical sensor for a small-molecule analyte, the impact of a stand-alone whole-blood immunoassay would arguably be larger, and the particular nature of the sensor is inconsequential for this study.

### 4.1.1 Background: Impedimetric Immunoassays utilizing Tobacco Mosaic Virus-Like Particles

In his thesis, my colleague Dr. Faheng Zang presented a highly sensitive immunoassay approach based on impedimetric sensing combined with Tobacco Mosaic Virus-like particles (TMVLP) as biorecognition elements [156]. Tobacco Mosaic Virus is a plant virus comprised of 2130 identical coat proteins helically arranged around its central single-stranded RNA [157]. This gives it a well-defined high-aspect-ratio nano-rod structure with a diameter of 18 nm and a length of 300 nm. Genetic engineering allows for adding surface-binding peptides such as cysteine for self-assembly onto gold, as well as receptor peptides for biorecognition. Deprived of its RNA, the engineered coat proteins can be expressed in bacteria to form TMVLP – retaining the high aspect ratio of the original virus as shown in Figure 4.2 while adding novel functionalities and allowing for scale-up through traditional biotechnological processes. These TMVLP structures can thus serve as exceedingly effective bioreceptors, providing high surface density as well as simple

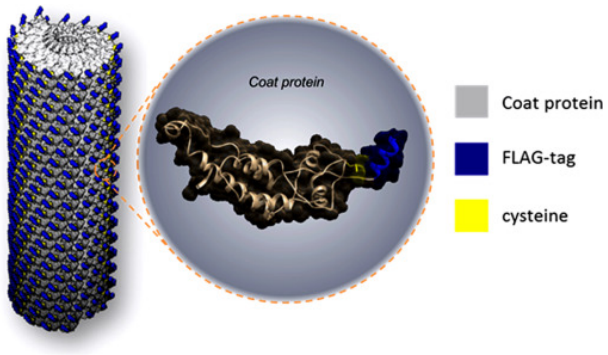


Figure 4.2: 3D schematic of a TMVLP segment (left) with helical arrangement of coat proteins (center) highlighting the native structure (gray) as well as the genetically engineered cysteine residues (yellow) and FLAG-tag sequences (blue). Reproduced with permission from [158].

device integration through self-assembly.

In typical immunoassays such as the gold-standard ELISA (enzyme-linked immunosorbent assay), labeling with a secondary antibody is required after the target antibody binds to the immobilized antigen. The secondary antibody is linked to an enzyme that – upon addition of its substrate – produces a visual change that amplifies the original detection event and is easily read out. In contrast, the high receptor density of TMVLP allows for direct, label-free detection. With the FLAG-tag (peptide sequence DYKDDDDK) as a receptor for the anti-FLAG antibody, a detection limit of 55 pM was demonstrated in buffer samples [156]. This relied on impedance-based detection, somewhat akin to the far-field impedance sensing of white blood cells described in Section 3.1. Here, the antibody binds to the TMVLP immobilized on interdigitated electrodes (IDEs). It displaces electrolyte and therefore alters the local effective permittivity, conductivity, and ionic concentration, all relevant factors in the measured impedance.

### 4.1.2 Design Overview

My system design is shown as a block diagram in Figure 4.3. The lab-on-a-chip device itself consists of two layers: The interdigitated electrode array (covering an area of $2 \times 2$ mm$^2$ with fingers of 6 µm width and spacing) is identical to a previous TMVLP-based

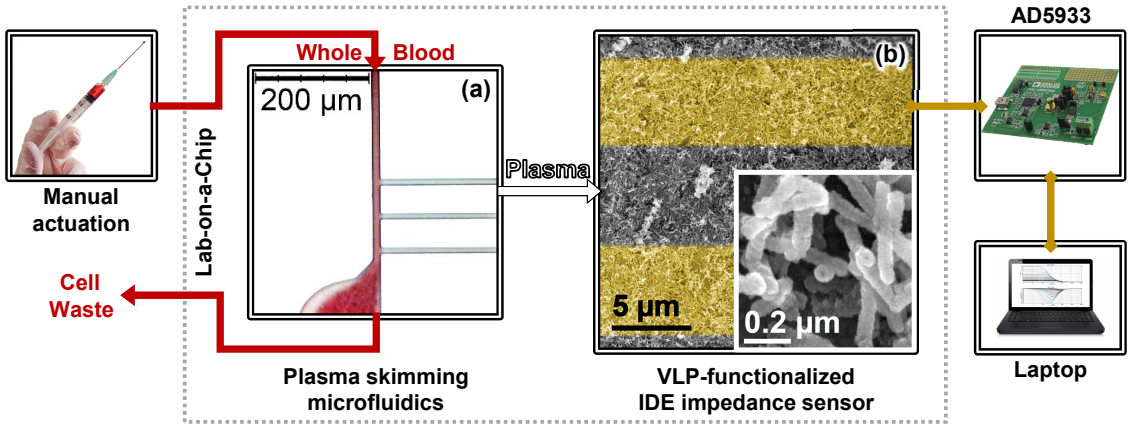


Figure 4.3: Block schematic of the impedimetric immunoassay system. (a) Micrograph of plasma skimming during operation. The cells (red) continue in the main channel toward the waste outlet, while plasma (clear) is skimmed off toward the IDEs. (b) False-color electron micrographs showing TMVLP coating on two gold IDE fingers, with high-magnification view in the inset. Reproduced from [159].

sensor [158]. These IDEs serve as the transducer for the biosensor, with the TMVLP coating assembled on top acting as the biorecognition element. The microfluidics feature plasma skimming channels leading to that array, branching off the central blood flow channel. While the cells stay within that channel, a small fraction of plasma is intended to go into the biosensor chamber. The height of the channels is chosen in line with the 20 µm utilized in Section 3.1, with systems integration in mind. Channel width and length serve as optimization parameters for plasma skimming explored in Subsection 4.1.4.

Toward a truly portable, label-free immunoassay, important design components are moreover the flow actuation and the signal readout. Both can add significant bulk and cost to a point-of-care system. With only a single inlet and – apart from a very high upper limit for shear stress based on cell lysis – no dependencies on absolute flow rate, I choose to rely on manual pressure-based actuation. For impedance readout, I employ a board-scale LCR meter, the AD5933 [160]. With these components, the system significantly reduces equipment requirements compared to previous work on whole-blood ELISA [79].

### 4.1.3 Experimental Methods

The optimization study described here yields a number of improvements in methodologies, particularly relating to fabrication and to handling of whole blood samples. Whole blood – with acid-citrate-dextrose (ACD) anticoagulant, recommended for cell viability during storage – is obtained from a blood bank and filtered through a 50 µm mesh size cell strainer prior to experiments. Fabrication methodology broadly evolved from that described in Subsection 3.1.3 to that in Subsection 4.2.2 over the course of the optimization study. Patterning of the microfluidic molds relied on photomasks 6.5 and 6.6 shown in Appendix A: Photomasks. For plasma skimming optimization, the microfluidics are bonded to unpatterned glass slides for observation studies under an optical microscope.

For the impedimetric immunoassay, the microfluidics are bonded to borofloat chips patterned with IDEs. These electrodes are connected off-chip using spring-loaded pins to either an Agilent E4980A Precision LCR meter or an Analog Devices AD5933 impedance analyzer board. I employ an AC potential of 0.14 Vrms to conduct frequency sweeps in the range of 0.02–200 kHz or 0.5–5 kHz, respectively, and read out the impedance $Z$. The AD5933 relies on a reference resistor for its measurements, and further requires calibration to a second known resistor to provide absolute impedance values. I choose both of these resistors at 1 kΩ, broadly in line with the expected impedance magnitudes. The frequency ranges are chosen based on instrument capabilities. Data recording in the impedance studies rely on a custom graphic user interfaces developed in LabView for the LCR meter, and on as-provided software by Analog Devices for the AD5933.

The on-chip ELISA and direct measurement procedures are schematically illustrated in Figure 4.4. After device assembly, the electrodes are pre-conditioned by running frequency sweeps continuously over 5 minutes in 1× Tris-buffered saline (TBS). Subsequently, I pipette 10 µl of 0.1 M PB containing 0.2 mg/ml genetically modified TMVLP into the PDMS chambers over the IDEs. Covering the chambers with a slab of PDMS, I allow the TMVLP to self-assemble on the IDEs over 18 hours, followed by 2 hours

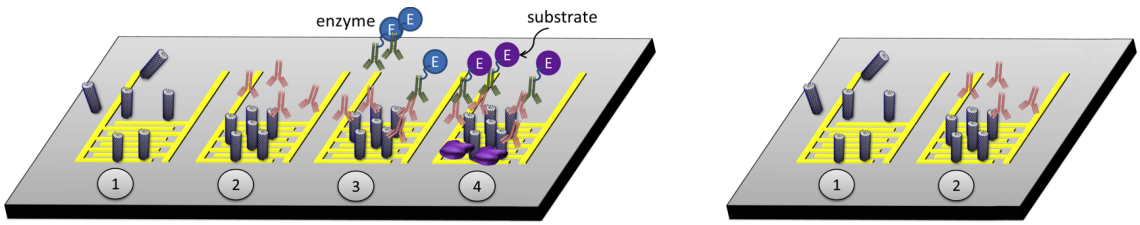


Figure 4.4: Sketch of procedures for on-chip ELISA (left) and direct, label-free detection (right). ① TMVLP assembly, measure baseline; ② Plasma skimming, target FLAG antibody binding (pink); ③ Secondary antibody introduced; ④ Enzyme substrate introduced to produce precipitate (purple). Adapted with permission from [158].

on a hotplate at 35 °C with the PDMS slab removed ①. This evaporation step serves to concentrate the TMVLP to create the very dense layer observed in Figure 4.3. Excess, unbound TMVLP is rinsed off with TBS. The microfluidics are then filled with commercial human serum along with the measurement chamber, which is now connected to a waste outlet with tubing. Subsequently, whole blood samples containing 0 (negative control) or 150 nM (positive sample) of anti-FLAG antibodies are injected through the inlet for $\sim$ 5 minutes, and plasma skimming is monitored through a microscope. For the direct, label-free experiments, measurements are obtained 2 hours later to allow for equilibration of antibody–antigen binding ②. For on-chip ELISA, the chamber is opened up again and the plasma rinsed out with TBS. I proceed to pipette in a 1:10000 dilution of the secondary, enzyme-linked goat anti-rabbit IgG (whole molecule)-alkaline phosphatase antibody and allow it to incubate for a further 2 hours ③. After another TBS rinse, the substrate (nitro-blue tetrazolium chloride and 5-bromo-4-chloro-3'-indolyphosphate *p*-toluidine salt; NBT/BCIP) is added to the chamber and allowed to react for 6 hours ④. Experiments conclude with a final TBS rinse prior to the measurement.

### 4.1.4 Plasma Skimming Optimization

As mentioned earlier, effective plasma skimming relies on designing channel geometries such that $R_{\text{cells}}/R_{\text{plasma}} \geq 7$, for a network with multiple plasma skimming channels satisfied at each node. Since the relevant $R$ at each network node is governed by all

downstream flow resistances, the equations become quite complex for the first nodes in the network, and electrical circuit simulation tools become very useful. For initial analysis, however, I will simply consider the final node, where the problem reduces to only two resistances $R_{\text{plasma}}$ and $R_{\text{cells}}$. Assuming a given uniform height $h$, the remaining four variables – width and length of each channel – leave a lot of freedom in satisfying the required flow condition. As a starting point, I consider the initial design by Yang *et al.*, for which they specify $h = 10$ µm, $L = 5$ mm, combined with $w_{\text{plasma}} = 9.6$ µm and $w_{\text{cells}} = 154$ µm [155]. Calculating $R_{\text{cells}}/R_{\text{plasma}}$ here interestingly yields a value of 38 – certainly satisfying the necessary flow condition, but far removed from their noted design target of 9.

My design optimization study thus takes two approaches: First, a purely model-based one. Second, one based mostly on variations of the published design. Given my channel height of $h = 20$ µm, I choose $L_{\text{plasma}} = 5$ mm, $w_{\text{plasma}} = 10$ µm and $L_{\text{cells}} = 37.5$ mm, $w_{\text{cells}} = 120$ µm. The widths are selected in line with Yang *et al.*'s design for the plasma channels, and with my own osmotic lysis work for the cell channel. Based on electrical network analysis, the interconnecting segments can be designed as $L_{\text{main}} = 300$ µm, $w_{\text{main}} = 25$ µm, yielding the overall geometry shown in Figure 4.3a. This design is mathematically equivalent to the design parameters given by Yang *et al.*, with $R_{\text{cells}}/R_{\text{plasma}} \geq 8.3$. The design allows for increasing this ratio further simply by shortening the cell channel (by punching the outlet closer to the skimming junction). The second design is a direct adaptation from Yang *et al.*'s design, with $L = 5$ mm, $w_{\text{plasma}} = 10$ µm, $w_{\text{cells}} = 154$ µm, and an increased height of $h = 20$ µm. This design, illustrated in Figure 4.3b, features a high resistance ratio of $R_{\text{cells}}/R_{\text{plasma}} \geq 83$. Design variations with $w_{\text{plasma}} = 13$ µm or $w_{\text{cells}} = 118$–$200$ µm allow for exploring a range of 43–110.

Initial experiments with ACD whole blood supplemented with heparin yielded an exceedingly high device failure rate. This was generally caused by white aggregates such

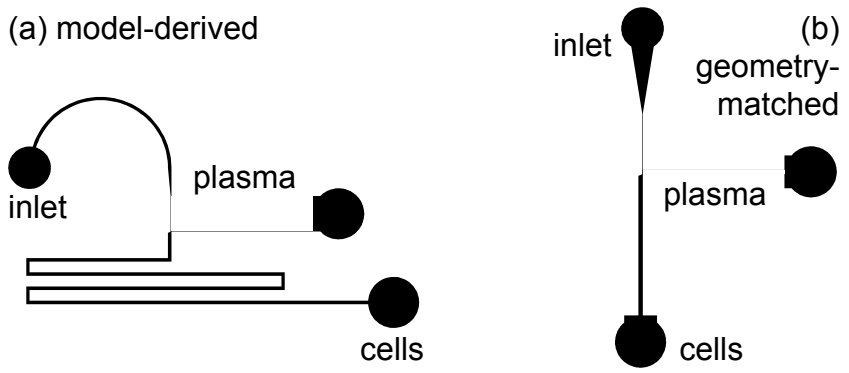


Figure 4.5: Plasma skimming designs. The geometries shown are derived (a) from the model given by [155], and (b) from their design used in experiments, as described in the text.

as those indicated in Figure 4.6 blocking the channels, particularly in the narrow region of $w_{\text{main}} = 25$ µm where the plasma skimming channels branch off. Such aggregates were previously observed also in the osmotic lysis study in Section 3.2; the wider channels and lower hematocrit, however, meant that such aggregates rarely resulted in complete device failure. As the blood samples are filtered through a 50 µm mesh prior to experiments, formation has to occur inside the device. My initial hypothesis was blood coagulation, and I thus attempted to address this by increasing the concentration of heparin, or supplementing it with another anticoagulant, ethylenediaminetetraacetic acid (EDTA). Especially the increase of the heparin concentration, however, only worsened the issue. This led me to the alternative hypothesis that the observed aggregates are not blood clots, but due to platelet aggregation. This phenomenon is a very early step in the complex coagulation cascade and is in fact enhanced by heparin (it prevents coagulation only by interfering further down in the cascade) [161]. Eliminating heparin and employing only EDTA as a supplementary anticoagulant indeed reduced the incidence of such aggregates, but did not eliminate it. Although EDTA interferes with the coagulation cascade at a much earlier stage than heparin by sequestering calcium ions, this action appears insufficient to prevent platelet aggregation in microfluidic devices.

To address platelet aggregation, a review of the literature yields two classes of

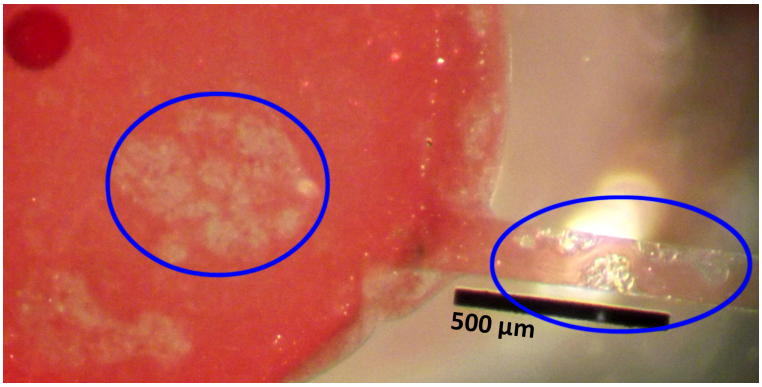


Figure 4.6: Exemplary micrograph of a device inlet showing aggregates (circled) observed for heparinized whole blood.

chemical agents: antiplatelet pharmaceuticals that aim to prevent aggregation, and thrombolytics that attempt to dissolve aggregates that have already formed [162]. The latter class is comprised of enzymes that generally activate native plasminogen by converting it to plasmin, which in turn can degrade the fibrin that is central to platelet aggregates' structural integrity. In this class, I select streptokinase due to its wide availability also for laboratory use. The class of antiplatelet drugs is significantly broader, encompassing molecules that interfere with a range of signaling pathways in platelet aggregation. The choice here is simplified as many of the available drugs are in fact prodrugs that rely on first-pass metabolism for conversion into an active form, rendering them ineffective for device use. The active forms themselves are typically unstable and/or commercially unavailable. Thus, I choose ticagrelor and tirofiban. The former acts as a P2Y purinoceptor 12 antagonist, a protein that is intimately involved with early signaling in platelet aggregation. Tirofiban, on the other hand, is an integrin αIIbβ3 antagonist, directly interfering with the structural aggregation proteins. In combination with EDTA, these compounds significantly reduce the observed platelet aggregation and enable experiments with whole blood.

The device materials themselves of course also play a role in not only platelet aggregation but more broadly whole blood handling in microfluidics. PDMS is inherently hydrophobic, and though the oxygen plasma treatment during device assembly renders

it hydrophilic for bonding, this is a temporary effect [163]. With biological fluids, this hydrophobic nature leads to non-specific surface fouling with proteins and cells (to yield an energetically preferential more hydrophilic surface in contact with the aqueous liquid). This can not only enhance aggregation and clotting problems as described above, but also sequester protein analytes out of solution before they reach the sensor. Thus, I implement pre-treatment of the PDMS channels with a 3% solution of Pluronic F-68, an amphiphilic polymer with a short central hydrophobic section that binds strongly to PDMS *via* hydrophobic interactions, and long hydrophilic tails that yield an effective hydrophilic surface. This particular polymer has been shown to be superior over other, similar treatments [164].

With these improvements in blood handling in place, I proceed to observation studies in the plasma skimming channels. From the exemplary blood flow micrographs in Figure 4.7 it becomes apparent that the model-guided design in (a) fails in preventing blood cells (red) from entering the plasma skimming channels. The situation is significantly better, though not optimal, in the geometry-matched design (b), where the first three channels remain clear (the thin red lines delineating the channels are due to optical artifacts), with cells only increasingly penetrating the ones further downstream. These results clearly highlight that the postulated condition of $R_{\text{cells}}/R_{\text{plasma}} \geq 7$ is insufficient for successful plasma skimming. Considering plasma skimming at higher resistance ratios further, I hypothesize that the evident lack of corner definition at the plasma skimming junctions is responsible. This rounding allows streamlines to penetrate further into the channels than their width would suggest, ultimately leading to a skimming breakdown. This lack of definition is likely caused by employing a transparency mask for fabrication, where the line width resolution limit of 10 μm matches the plasma channel design width.

Thus, I repeat experiments with the geometry-matched design, and variations thereof, in a fabrication process modified to employ a much higher (1.5 μm) resolution chrome mask 6.6 (Appendix A: Photomasks) to yield sharper corners. Indeed, the failure

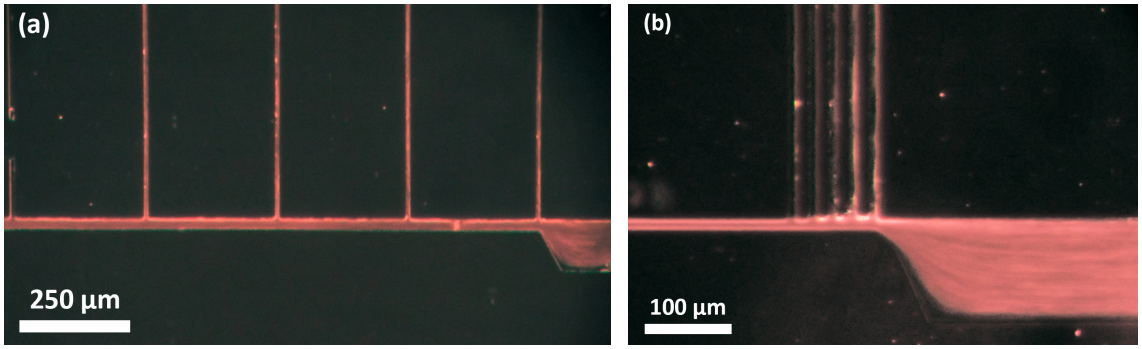


Figure 4.7: Optical plasma skimming observations with whole blood in model-derived (a) and geometry-matched (b) designs.

mode observed previously – with increasing streamline penetration into downstream nodes – is eliminated here. However, performance remains highly variable. In testing a large number of these devices with the aforementioned variations in geometry, no clear dependency of efficiency on blood channel width becomes apparent. Two modes of failure dominate: Total blockage of the device with an aggregate, a challenge that cannot entirely be overcome for extended operation even with the procedures described above, and transient passage of aggregates or cell clusters. The latter does not completely prevent the device from being utilized. However, it drastically changes the flow resistances in the device, leading to preferential flow of cells also through the plasma skimming channels. I observed that this mode of failure was significantly less likely in devices employing only three instead of five skimming channels, where the balance of resistances is less prone to disruption by such transients. While this reduces the plasma skimming efficiency, I decided this was the optimal design for subsequent use as seen in Figure 4.3a. Due to high variability in the geometry variation experiments, no definite new design guideline could be derived, except that the lower limit for $R_{\text{cells}}/R_{\text{plasma}}$ is clearly above 7, though likely below 40, matching the experimental (but not theoretical) findings by Yang *et al.*

With the selected optimal design, I still observe a device failure rate around 20% over the course of 5 minutes of plasma skimming operation, with the likelihood of failure trending toward 100% for use beyond 15 minutes. While this is shown to be acceptable for

the immunoassay below, an integrated downstream white blood cell counter will likely require operation durations toward the longer end of that range, particularly in a research setting. This makes the approach unsuitable for further integration in a cellular/acellular sensing system.

### 4.1.5 Label-free Antibody Detection in Whole Blood

With the optimized plasma skimming design, I proceed to conduct impedimetric immunoassay experiments. Initially, I simply consider the TMVLP coating step, observing an increase in impedance magnitude of 143±23% over the IDEs' respective bare impedance at 2 kHz. While I record frequency sweeps at each step of the experiment, I find this frequency to be the most sensitive. For the LCR meter, lower frequencies show even better signal-to-noise ratios. However, due to limitations of the on-board clock in the AD5933, its signal degrades severely below 2 kHz. The general frequency range agrees with previous findings that changes in ionic double-layer capacitance (dominant at this and lower frequencies) hold the most information for this format of impedimetric immunoassays [158]. The significant increase in signal specifically with TMVLP coating verifies sensor functionality as well as functionalization, and is also in line with previous experiments.

To test immunoassay capabilities, I manually inject whole blood (control), or whole blood spiked with 150 nM anti-FLAG antibody, through the blood channel, skimming off plasma into the sensing chamber. As illustrated in Figure 4.4, I follow two sets of measurement procedures: First, a traditional labeled on-chip ELISA for validation. Second, the direct, label-free measurement. As on a traditional well plate, on-chip ELISA employs a secondary antibody linked to an enzyme that produces a colorimetric signal from a substrate. The same process can also be read out impedimetrically, since the color indicator forms an insoluble deposit on the electrodes, yielding a drastic change in impedance. Due to the requisite incubation times at each step, the process takes on the order of 10 hours. Additionally, the intermediate rinsing steps require manual interaction

and pipette access to the measurement chamber. At the end, I measure the impedance again in TBS and compare to a baseline TBS measurement immediately after TMVLP assembly.

In Figure 4.8, I display this change in impedance for whole blood with and without the target antibody. To validate the portable instrumentation, I conduct the measurements both with a precision LCR meter (yellow) as well as the AD5933 (blue). The impedance drastically increases compared to the baseline for all conditions, with the highest signals observed in the presence of the target antibody. The impedance change even in the absence of antibodies is a clear indication of non-specific binding of plasma proteins and/or label antibodies. Variability in these factors, as well as in blood sample volume due to the manual injection process, likely accounts for the high standard deviations observed overall. Still, the 52% additional signal measured with the LCR meter in the presence of antibody (*versus* its absence) proves significant ($p < 0.1$). The lower +36% recorded with the AD5933 do not meet that criterion. This significantly lower signal compared to that of the LCR meter can be explained by a saturation effect. The AD5933 requires an initial choice of reference and calibration resistors in line with the expected subsequent impedance signals. The further the signal deviates from these resistor values, the less accurate the measurement becomes. The almost 2-fold change in impedance as measured by the LCR meter easily exceeds that range.

The above observations bear comparison also to the visual observations in Figure 4.9. These micrographs show exemplary IDE surfaces at the end of the ELISA procedure, with significant yet highly variable reaction product deposition (black) on the electrodes when antibody was present in the blood samples. In the absence of target antibody, non-specific deposition is still visible. These results validate the experimental procedure itself, and align with the findings based on impedimetric readout above.

For the direct, label-free measurement (*cf.* Figure 4.4) the procedure simplifies significantly compared to on-chip ELISA. With only a single requisite incubation step,

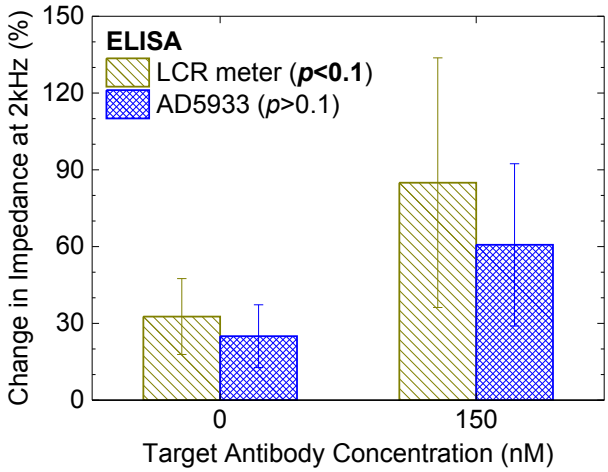


Figure 4.8: On-chip ELISA. Percentage change in impedance magnitude *versus* baseline for human whole blood samples ($n \geq 2$ each; $p$-values from ANOVA) with or without target, measured using high-precision LCR meter or AD5933 in buffer solution after ④. Adapted from [159].

the overall assay time reduces to around 2 hours. Moreover, no rinsing is required, and thus no added manual interaction. I compare the impedance measurement at the end (*i.e.*, in skimmed plasma) to one in commercial human serum conducted immediately after TMVLP assembly. Employing serum instead of TBS here as the baseline is intended to more closely mimic the electrolyte present for the final measurement.

I plot these changes in impedance for the direct measurements with the LCR meter (green) and the AD5933 (red) in Figure 4.10. Here, all measurements interestingly display a decrease in signal compared to the baseline. I attribute the overall negative magnitudes to the remaining difference in dielectric properties between the skimmed plasma and the baseline commercial serum. More importantly, however, the signal in the presence of the target antibody is 10% greater than in the controls for both instruments – a value that also is significant for both instruments ($p < 0.1$). The variance is greatly reduced compared to on-chip ELISA, in line with the hypothesis of compound variability from the many steps involved there. Looking at the difference between the two instruments, I find only a constant 2% offset from between them. The lower overall signal range here of $\sim$ 20% (compared to the 100% in on-chip ELISA) is clearly favorable for the AD5933. This

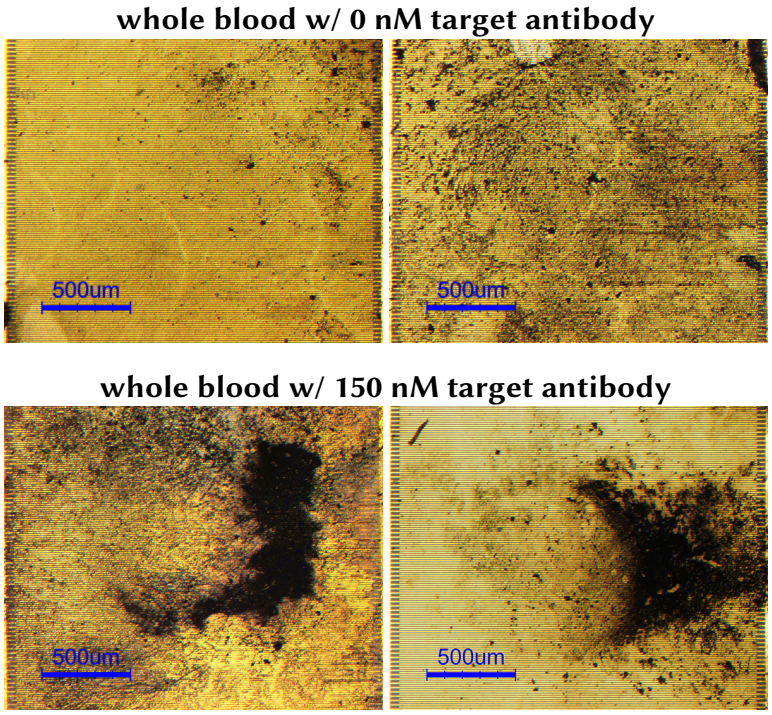


Figure 4.9: On-chip ELISA. Micrographs of two exemplary IDEs each after step ④ for blood samples without (top) or with (bottom) anti-FLAG target antibody. The label enzyme reaction product appears as a dark precipitate on the gold IDEs. Adapted from [159].

validates the feasibility of implementing a truly portable and integrated immunoassay system.

### 4.1.6 Synopsis

I explored plasma skimming as a strategy for whole blood fractionation. My work identified discrepancies between theory and experiments from previous work on the topic and revealed that model-derived guidelines for design are insufficient. I employed an optimized design to implement a proof-of-concept impedimetric immunoassay and demonstrated for the first time direct, label-free detection of antibodies in whole blood with a fully portable system. I found that plasma skimming is suitable for such short-term blood/plasma separation processes, but that high device failure rates present a barrier to longer-term use such as required for downstream cell analysis. However, in the course

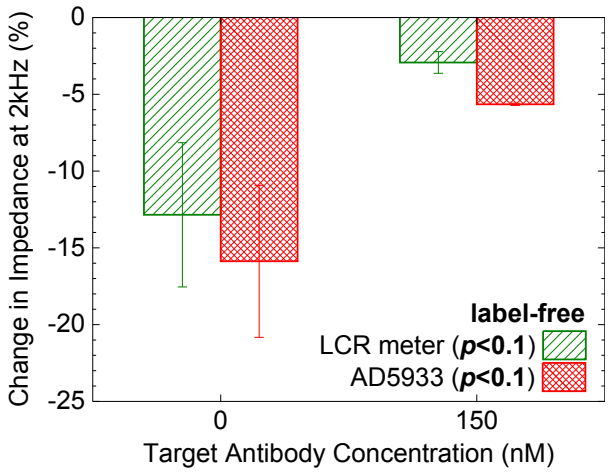


Figure 4.10: Direct, label-free detection. Percentage change in impedance magnitude *versus* serum baseline for human whole blood samples ($n \geq 2$ each; $p$-values from ANOVA) with or without target, measured using high-precision LCR meter or AD5933 after ②. Adapted from [159].

of the experiments, I developed suitable procedures for handling whole blood samples, minimizing platelet aggregation and device biofouling.

## 4.2 Concurrent Clozapine & Cell Sensing in an Integrated Device

With a parallel integration of clozapine and cell sensing through plasma skimming infeasible based on the results of the previous Section, I instead pursue a series integration approach for my system – direct measurement of clozapine in whole blood in the incoming sample stream, and downstream white blood cell detection. As discussed in Subsection 1.3.4, molecular sensors for whole blood typically employ a blood/plasma separation step due to interference concerns. Direct sensing based on redox activity, however, is one of the few transduction modalities where the presence of blood cells will not cause obvious interference issues – signals are generated by electrochemical reactions at the electrode surface, and cells are not expected to yield such, or at least no more so than serum alone. At a fundamental level, cells of course reduce the effective concentration of all analytes by a factor of 2 at typical hematocrit values around 50%, and diffusion behavior of analytes may be affected. Still, the chitosan-CNT/graphene

redox catalysis system is shown to be highly selective and sensitive in clinical serum samples in Chapter 2, sufficiently so that direct detection of clozapine in whole blood is worth investigating.

At the same time, translation of the subsystem integration findings from Chapter 3 into a functional white blood cell counter requires further refinements. The previous Section addresses some of these with regard to whole blood handling. The major one, however, is with regards to instrumentation: The low sampling rate of the LCR meter already imposed limitations on the earlier studies; the combined system would exceed them. White blood cell differentiation will require well-defined signal peaks for each cell, dual-frequency measurements as discussed in Subsection 1.3.3, and higher total flow rates (due to the multiplicative flow ratio requirements from lysis and focusing). Such rapid and highly accurate readout of electrical signals is the domain of lock-in amplifiers, which however require additional circuitry to enable impedance measurements.

Here, I present my design for an integrated microsystem for concurrent acellular/cellular marker detection, incorporating refinements from and upon all preceding Chapters. I first evaluate different instrumentation options for impedance cytometry in this device. Finally, I validate the overall concept using human whole blood samples spiked with clozapine.

### 4.2.1 Design Overview

My design, schematically illustrated in Figure 4.11, is a combination of a planar three-electrode electrochemical cell and the designs employed in Chapter 3. The sample stream (flow rate $Q_s$) passes from the clozapine detection chamber to a lysis junction, where the blood is exposed to DI water (combined flow rate $Q_l$), causing erythrocyte rupture during passage through the serpentine channels. Immediately prior to the impedance cytometry electrodes, the stream is hydrodynamically focused by additional DI water flows (combined flow rate $Q_f$).

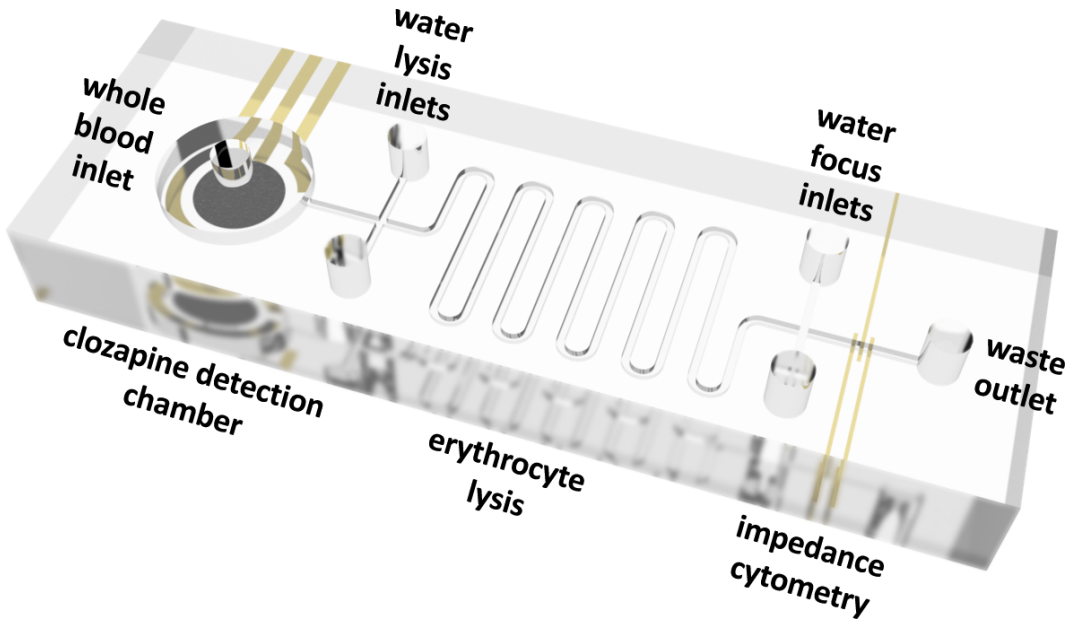


Figure 4.11: Schematic rendering of the integrated microsystem developed in this thesis.

The electrochemical cell employs a chitosan-CNT/graphene (1%/1%) working electrode, its 2 mm diameter chosen to be equivalent to that of the commercial disk electrodes. It is encircled at a distance of 300 µm by a 400 µm wide gold counter electrode over a 270° arc, and a gold pseudo-reference electrode over an arc of 30°. While such a reference is less stable than Ag/AgCl, it proves sufficient for experiments and simplifies fabrication significantly. The microfluidic dimensions match those given in Chapter 3. The impedance cytometry electrode design is changed significantly to accommodate differential measurements (*cf.* Subsection 4.2.4): Instead of a simple pair, I employ a central source (or ground, depending on the instrumentation circuitry) electrode flanked by two ground (source) electrodes, all with width and spacing of $l = g = 25$ µm. The flanking electrode traces are designed for matching length so the signal divides equally between the two conduction paths. Moreover, based on the observations in Section 3.1 on the placement distance $d$ from the focusing junction, this is minimized to 50 µm, close to the minimum achievable with manual alignment of the layers.

### 4.2.2 Device Fabrication

As with the earlier-generation devices in Chapter 3, the design is implemented in two physical layers – the coplanar electrodes on glass, and the microfluidics in PDMS. Compared to the previous devices, however, I implement a number of improvements in the fabrication process flow here, schematically illustrated in Figure 4.12. After 1 minute immersion in Piranha and dehydration for at least 5 minutes, I first spin-coat a layer of negative Futurrex NR9-1500PY photoresist (3 s ramp, 3000 rpm, 30 s hold) on a borofloat glass wafer, followed by a 60 s bake at 150 °C. The photomask 6.7 shown in Appendix A: Photomasks and printed on transparency film is used to expose the resist to 245 mJ/cm² UV light (adjusted from standard processing parameters to account for the transparent wafer), followed by a 60 s bake at 100 °C. I develop the resulting patterns for at least 25 s in RD6 developer, diluted with DI water 3:1, followed by incremental 5 s immersions guided by pattern inspection under a microscope (E1). Next, I deposit 20 nm chrome, functioning as an adhesion layer, and 200 nm gold utilizing e-beam deposition (E2). Finally, the extraneous metal is lifted off by immersion of the wafer into acetone for ~ 30 minutes, assisted by agitation and brief ultrasonication as needed (E3). Compared to the wet etching approach employed previously, lift-off yields better edge definition and eliminates residual gold sometimes left in wet etching due to photoresist scum. To protect the structures from scratches during the subsequent wafer dicing, the entire wafer is processed with Shipley 1813 photoresist as described in Subsection 3.1.3, only utilizing a flood exposure with a 3-fold higher dose and omitting development.

For the microfluidics, I repeat the Futurrex photolithography on a dehydrated Piranha-cleaned blank silicon wafer with two important changes: The exposure dose is reduced to 190 mJ/cm² for the reflective substrate, and the photomask 6.4 shown in Appendix A: Photomasks (again on transparency film) is utilized (M1). After development, I transfer the pattern into the silicon by deep reactive ion etching (DRIE; M2). The process is monitored by profilometry to achieve a final etch depth of ~ 20 µm. Finally, I strip the

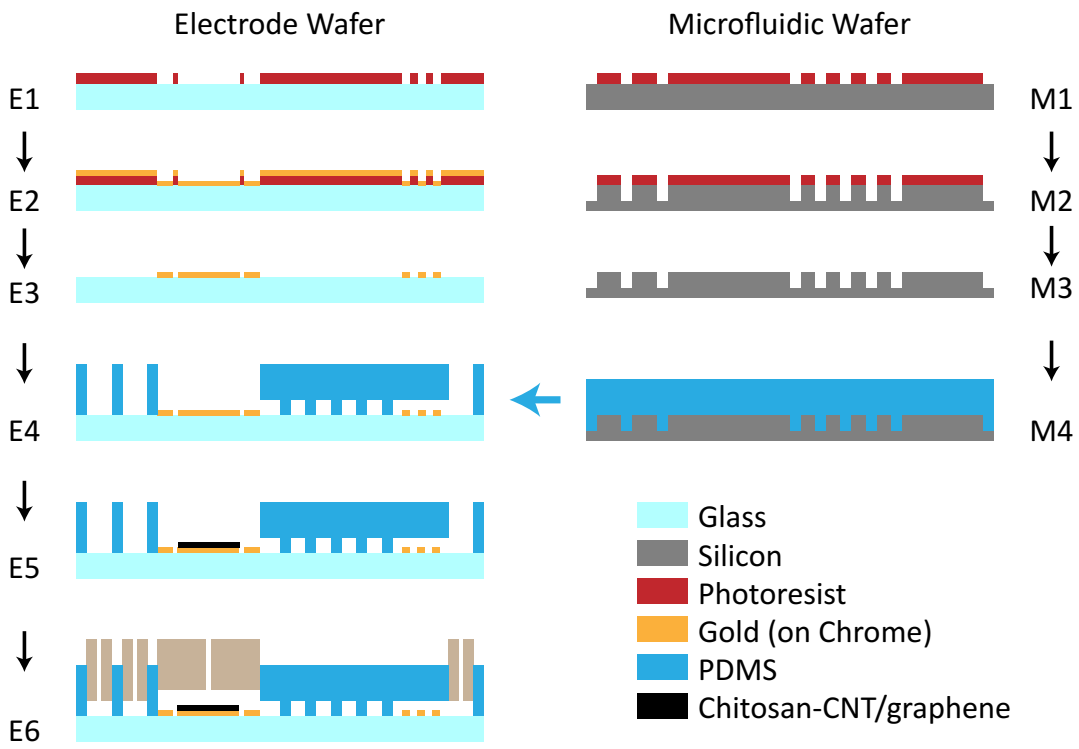


Figure 4.12: Abbreviated fabrication process flow for the final-generation devices described in the text.

photoresist by successive rinsing with acetone, isopropanol, and methanol (M3). The advantages here over an SU-8 process are the shorter duration (due to the long bake times for SU-8) as well as improved corner definition (due to the thinner resist) and increased resilience of the features.

Subsequent preparation of the wafer with alconox, PDMS molding, and device assembly follow the previously described procedures in Subsection 3.1.3 (M4 & E4). The one process alteration is that I employ a 5 mm diameter biopsy punch to create the electrochemical measurement chamber. This necessitates a thicker PDMS layer to later provide a sufficiently good friction fit seal, thus I increase the total PDMS mass to 38.5 g per wafer.

### 4.2.3 Experimental Methods

Off-chip connections are implemented using spring-loaded pins to a Bio-logic VSP-300 potentiostat for electrochemistry as well as to the impedance readout instrumentation described in Subsection 4.2.4. For the working electrode modification (E5), I disperse carbon nanotubes and graphene at 1% w/v each in chitosan solution by ultrasonication for 45 minutes, preceded and followed by brief vortex mixing. Immediately thereafter, solution is pipetted into the 5 mm diameter chamber, and a constant cathodic current of 32 A/m$^2$ applied for 90 s between the on-chip working electrode and a coiled platinum wire electrode immersed in solution. Excess material is allowed to diffuse away with the electrode immersed in DI water, followed by PB prior to experiments. The measurement chamber is sealed off prior to experiments using a short piece of large-diameter Tygon tubing (1.6 mm inner and 4.8 mm outer diameter), which creates a microfluidic inlet port with dimensions similar to those at the others directly punched into the PDMS.

For experiments, the device is mounted in a custom-built Faraday cage on spring-loaded pins with the requisite external connections as pictured in Figure 4.13. The fluidic inlets are connected to New Era syringe pumps (NE-1002X, or NE-300 for the flow focusing inlet) holding 1 ml syringes using Tygon tubing (0.19 mm inner and 2.03 mm outer diameter; E6). The device is primed with a solution of 3% Pluronic F-68 in water, followed by a rinse with PBS. The actual sample stream consists of whole human blood samples with ACD anticoagulant obtained from a blood bank and pre-treated according to the procedures in Subsection 4.1.4. The lysis and focus flows consist of DI water with resistivity $> 17$ MΩ cm.

I control flows and record data with custom graphic user interfaces developed in LabView. For each flow condition, the experiments run for approximately 30 minutes. I analyze the data in MATLAB, employing the code reproduced in Appendix C: MATLAB Code. Here, the data is drastically different from that obtained by the LCR meter in previous studies, due to both the higher sampling rate and the generally differential

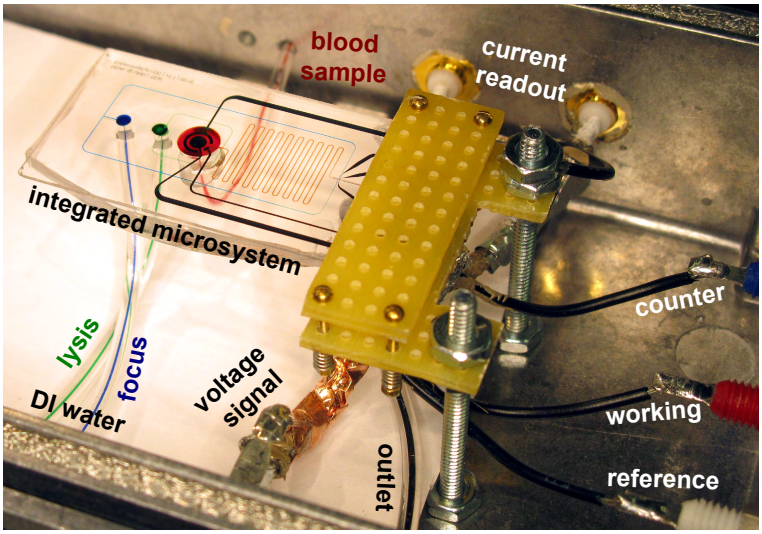


Figure 4.13: Photograph of the experimental setup. The fully integrated microsystem is mounted on spring-loaded pins inside a custom Faraday cage. Shielded cables connect to the voltage signal input and the differential current readouts. Unshielded wires provide connections to the electrochemical working, reference, and counter electrodes. Fluidic tubing is routed to three pump-mounted syringes (food coloring to highlight flows: sample – red; osmotic lysis – green; hydrodynamic focusing – blue) and a waste reservoir (black).

nature of the measurements. The algorithm first translates the measured currents into differential impedance signals $\Delta Z$ using the respective input voltages. The background signal – for differential measurements devoid of information and only indicative of parasitic effects in the wiring – is determined by applying 40 Hz moving average and 20 Hz low-pass filters and is subtracted out. Downsampling to 25 kHz removes signal fluctuations and reduces storage and memory requirements. True peaks in the cleaned-up $\Delta Z$ signal are detected using a wavelet-based algorithm adapted from Caselli *et al.* and Evander *et al.* [124,165]. The high-frequency signals are corrected for size-based effects with simple division by the low-frequency signals [54].

### 4.2.4 Impedance Instrumentation

A lock-in amplifier, as mentioned earlier, is the ideal instrument for high-sampling-rate measurements of AC signals – specifically, of voltages. With AC signal sources

also generally being voltage sources ($V_{\text{stim}}$), current-to-voltage conversion is needed to measure an impedance $Z$ with a lock-in amplifier. Three approaches, illustrated in Figure 4.14, are broadly available for that purpose. First, a simple ratiometric one, wherein a known, fixed impedance $Z_1$ is introduced into the circuit to yield $V_{\text{out}} = V_{\text{stim}} \frac{Z}{Z_1+Z}$. The sensitivity to small impedance signals $\Delta Z \ll Z$ – the true parameter of interest for an impedance cytometer – is greatest when $Z \approx Z_1$. This presents an obvious limitation with regard to dynamic range. The second approach retains this limitation, but still presents a notable refinement. In the Wheatstone bridge circuit, the output voltage is:

$$V_{\text{out}} = V_{\text{stim}} \left( \frac{Z}{Z_1 + Z_{\text{X}}} - \frac{Z_{\text{R}}}{Z_1 + Z_{\text{R}}} \right) \tag{4.2}$$

Thus, it yields a differential measurement between $Z$ and a reference impedance $Z_{\text{R}}$. The usefulness for an impedance cytometer becomes apparent if $Z_{\text{R}}$ is another pair of electrodes in the cytometer – assuming that only one set of electrodes is occupied by a cell at any given time, this circuit gives practically direct access to $\Delta Z$. It eliminates background impedance noise, *e.g.* due to fluctuations in the environment, and allows for more sensitive measurements due to the limited dynamic range of the lock-in amplifier. With a ratiometric approach, a large voltage measurement range is needed to detect a small superimposed signal; with a Wheatstone bridge, a more sensitive range matching the actual signal magnitude can be applied. As mentioned in Subsection 1.3.3, this is at the heart of the approach taken by Gawad *et al.* [54].

The third technique addresses the dynamic range limitation of both of the above. The transimpedance approach employs an operational amplifier and a feedback impedance $Z_{\text{F}}$ to convert the current $I_{\text{Z}}$ into $V_{\text{out}} = V_{\text{stim}} \times Z_{\text{F}}/Z$. At least in theory, this circuit is purely "linear" with respect to its response to additional impedance signals $\Delta Z$, *i.e.* the reference impedance can be chosen for maximum gain independent of $Z$. The concept can be expanded to differential measurements by simply employing two

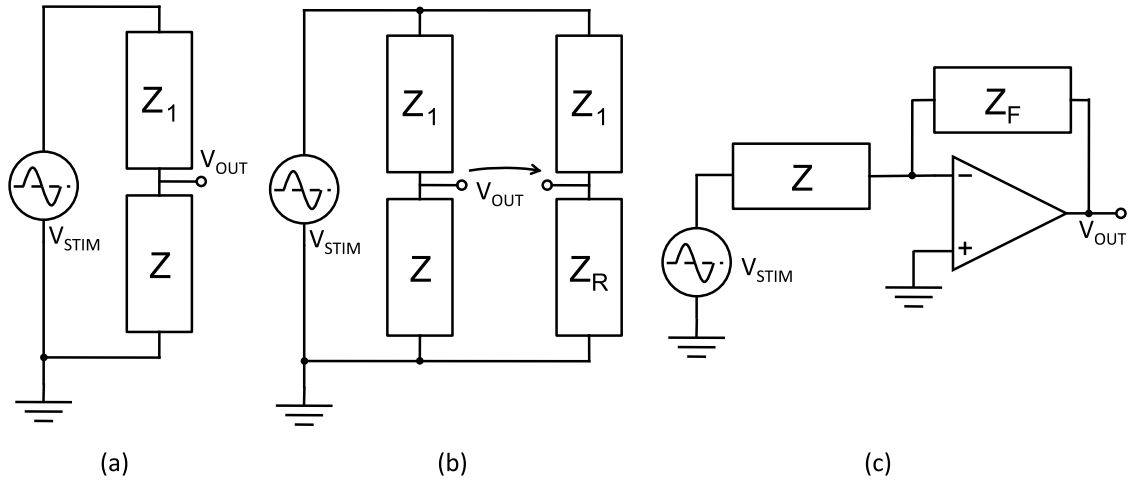


Figure 4.14: Three circuits to measure changes in impedance as a voltage. (a) Ratiometric circuit, (b) Wheatstone bridge circuit, (c) transimpedance amplification circuit. Adapted from [166].

transimpedance amplifiers for two electrode pairs, and connecting them to the differential inputs of the lock-in amplifier. This is the route taken by Holmes *et al.* [54].

For my own work, I employ a Signal Recovery 7280 lock-in amplifier that distinguishes itself by its dual-frequency measurement capabilities. As it lacks a fast, built-in computer interface, I utilize a National Instruments PCI-6221 data acquisition card to record signals from its analog outputs at a sampling rate of 125 kHz. One signal source is built into the lock-in amplifier; the second frequency is provided by an Agilent 33220A function generator connected in series. In line with Figure 3.6, I choose the signal frequencies of 90 kHz and 900 kHz to assess cell size and membrane properties. The output voltage levels and lock-in input ranges are chosen to maximize signals, limited by constraints of avoiding source signals greater than 0.8 Vrms due to hydrolysis, the 1 V input limit of the lock-in, and the need for matched voltage ranges at both frequencies. The lock-in amplifier time constants are selected as short as possible – at 90 kHz, a single period equates 11 µs, and at least a few periods are required for measurement, yielding a limit of 50–100 µs. While the discussion here referred to two electrode pairs for differential measurements – one for the signal, one for the background – only three electrodes with equal width and spacing are required in practice. For the bridge circuit, the

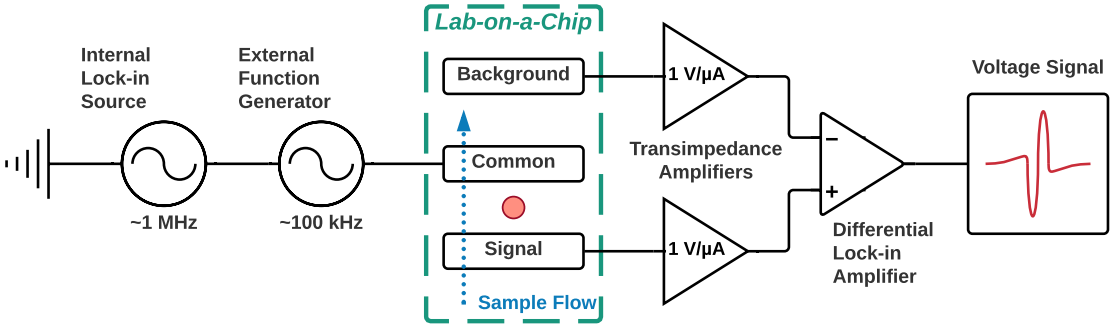


Figure 4.15: Circuit employed for impedance measurements in this work and described in the text.

central electrode can serve as a common ground, with the flanking electrodes providing the two source legs of the bridge. For the differential transimpedance circuit, the central electrode can serve as the source, with the flanking electrodes providing two equal ground connections.

The bridge circuit is initially very appealing due to its implementation simplicity, requiring only an additional voltage divider. Ideally it should be chosen with at least 50 kΩ, around the magnitude of the empty channel impedance without flow focusing. However, I experimentally find that a divider of 1 kΩ provides better signal-to-noise ratio – as previously noted by Gawad *et al.*, this is due to parasitic capacitance effects in the chip connections and traces [54]. This indeed allows for highly accurate $\Delta Z$ measurements and particle analysis. The major limitation of this approach only becomes clear when considering hydrodynamic focusing. The added DI water sheath flows will increase not only the inherent impedance signals $\Delta Z$ but also the empty channel impedance, increasing the mismatch with the voltage divider. Adding the Wheatstone bridge Equation 4.2 into the (conservative) analytical model in 6.1 shows that the gain in $\Delta Z$ is more than canceled out by this dynamic range limitation of the circuit. As expected, experiments reveal an even more pronounced loss in sensitivity around 20% at a flow ratio of $FR = 0.5$, in line with the experimental trend lagging behind the analytical one in Section 3.1.

Thus, I implement the differential transimpedance circuit as shown in Figure 4.15, with two Femto HCA-2M-1M low-noise transimpedance amplifiers featuring a gain

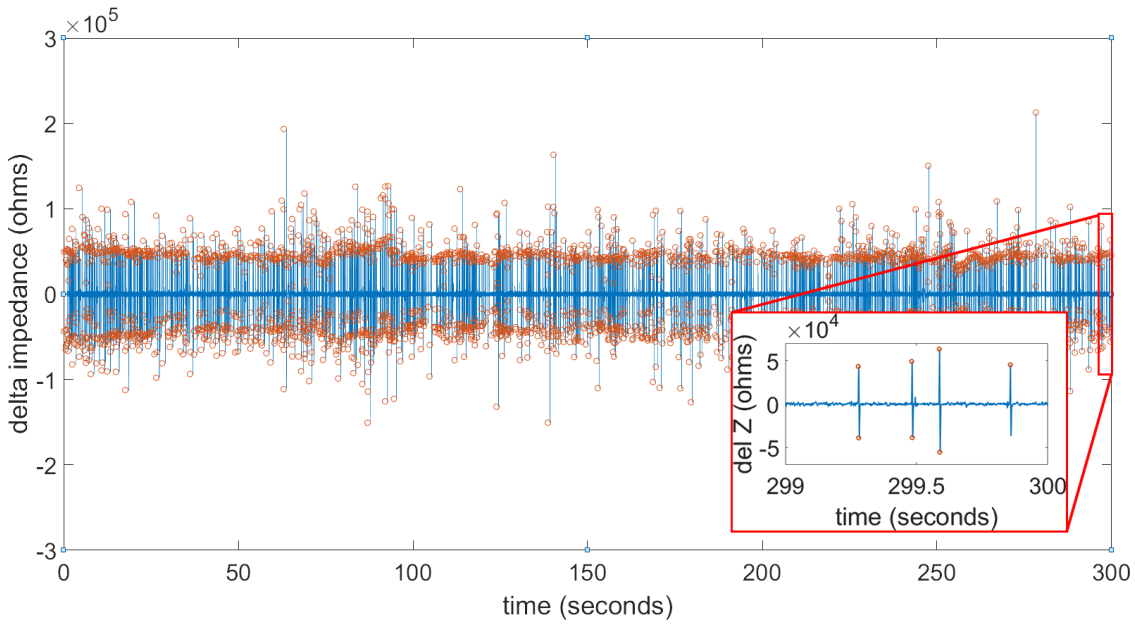


Figure 4.16: Representative processed experimental impedance cytometry signals $\Delta Z$ from $\phi = 6$ μm diameter particles.

of $Z_F = 1$ MΩ. The linear response characteristics indeed predict that the gain in sensitivity from hydrodynamic focusing is conserved with the readout. The exemplary bead experiment recording in Figure 4.16 (after the MATLAB processing described in Subsection 4.2.3) highlights the stable and low-noise nature of the set-up, with each bead producing a distinct, roughly symmetric pair of peaks as it passes over the "signal" and "background" electrodes. The MATLAB processing mainly serves to eliminate the offset from zero that is present in the raw data, caused in large part by source signal leakage *via* capacitive and inductive coupling into the readout channels. As the wiring for the two readout channels features slightly different geometrical orientation with respect to the input wire, this is not entirely compensated for by the differential nature of the measurement. Improved wire shielding serves to minimize these contributions, but cannot entirely eliminate them.

### 4.2.5 Results and Discussion

First, I evaluate the clozapine sensing capabilities in the integrated device. Figure 4.17 shows the DPV signals obtained from whole blood (negative control) or from blood spiked with 100 µM clozapine flowing through the device. I start the measurements immediately after the chamber is completely filled with blood, after which I reduce the flow rate to around 1–10 µl/h. Both samples show a pronounced peak around +0.2 V, corresponding to the background signals previously observed with serum samples or uric acid (*cf.* Subsection 2.3.2 and Subsection 2.1.6). It is worth noting that, due to the lack of a true reference electrode in this system, the peak positions shift compared to measurements taken with an Ag/AgCl reference electrode, including between devices and measurements. For this, the background peak actually becomes beneficial, providing a built-in reference that the potential scale can be adjusted to. In the presence of clozapine, a second peak appears around its expected potential of +0.37 V, well removed from the purported uric acid peak. Overall, the characteristic signals are very similar to those obtained in clinical serum samples; whole blood does not appear to have a direct impact on electrochemical measurements. Only the clozapine peak signal magnitude is reduced compared to serum observations – 4.38 µA here, compared to an expected 3.37 µA (calculated from the average of the chitosan-CNT and chitosan-graphene serum calibration curves in Figure 2.22). I propose two hypotheses: First, the chitosan-CNT/graphene fabrication process clearly proceeds differently in the more constrained environment present here, as evidenced by the higher current density required to form stable films. The film deposition parameters may thus require further optimization to achieve sensitivity closer to that of the macro-scale electrodes. However, this is proven less likely by the similar signals I observe for Fc in both micro- and macro-scale settings. The second hypothesis relates to blood as a matrix, where the added volume of the blood cells may restrict diffusion. Perhaps more importantly, approximately 30% of clozapine also partitions into red blood cells, which – akin to protein binding – reduces the available concentration for electrochemical

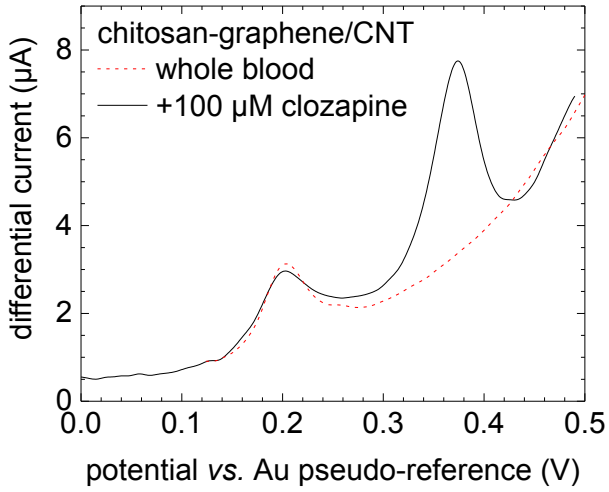


Figure 4.17: Clozapine detection in whole blood. Differential pulse voltammograms from human whole blood (red dash), and blood spiked with 50 µM clozapine (black solid), flowing over chitosan-graphene/CNT electrodes inside the microsystem.

detection [18]. This magnitude closely matches the ~25% reduction in current compared to serum-based calibration curves, suggesting the volume taken up by the red blood cells does not play a significant role, at least in a micro-environment. Accounting also for protein binding, while 100 µM clozapine were spiked into the blood and ~ 70 µM remain in the liquid fraction, only approximately 4 µM are available for sensing (not bound to proteins). After blood/plasma separation, these values would all increase by an additional factor of approximately 2. While the exact total serum concentrations (sum of protein-bound and free; reported by gold standard HPLC/MS/MS) is thus not known for my experiments here, it still appears that the sensitivity of chitosan-CNT/graphene electrodes is generally compatible with the clinical range even with whole blood samples inside my integrated microsystem.

For the impedance cytometer, I show two important control experiments in Figure 4.18. I plot differential signal magnitudes $\Delta Z$ as a two-dimensional scatterplot, with the 90 kHz low-frequency, size-sensitive signal on the $x$-axis, and the 900 kHz high-frequency, membrane-sensitive signal on the $y$-axis (normalized by the low-frequency signals to eliminate the cross-sensitivity seen in Figure 3.6). The colors correspond to the

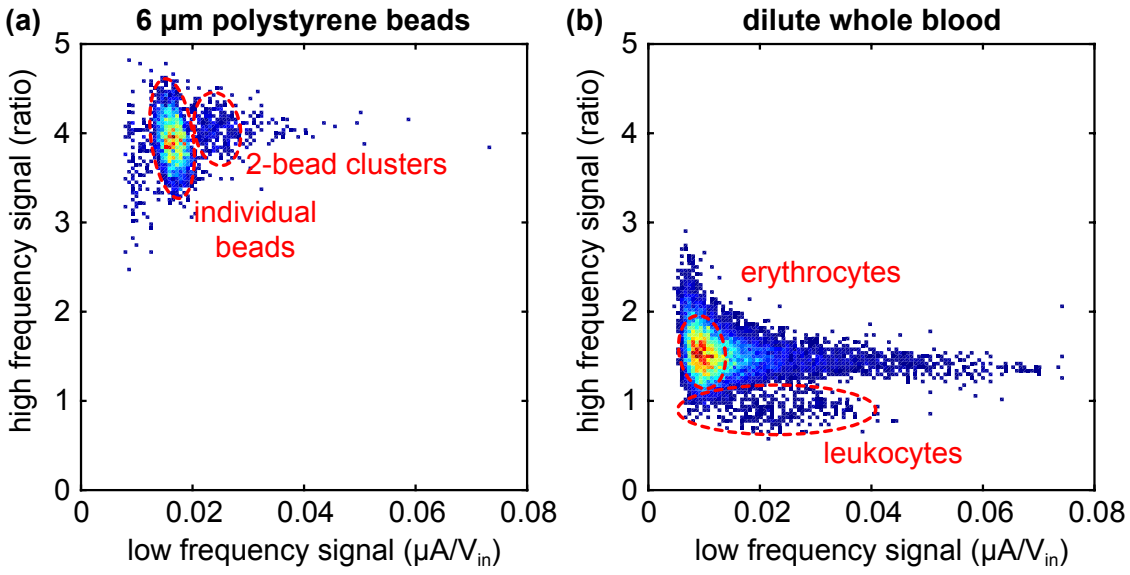


Figure 4.18: Impedance cytometry controls. Scatterplots of impedance signals $\Delta Z$ at 90 kHz ($x$-axis; size-sensitive) and 900 kHz ($y$-axis; membrane-sensitive; corrected for size-based effects), with colors corresponding to the local event density from low (blue) to red (high), for (a) $\phi = 6$ µm polystyrene particles or (b) 2,000-fold diluted whole blood. Both samples are in buffer solution, with the lysis solution also switched to PBS (no lysis).

density of events in a given area of the plot, from low (blue) to high (red). In Figure 4.18a, I present data collected from a sample containing 6 µm diameter polystyrene beads in electrolyte (with a lysis flow also consisting of PBS) making this the two-dimensional equivalent of Figure 3.8. The high density population around {0.015, 4} can easily be attributed to the beads, and the smaller population around {0.025, 4} agrees well with the expected signal from clusters of two beads. Compared to the analogous experiment in the previous Chapter, the populations here are much more clearly delineated, reflecting the impedance readout improvements described in Subsection 4.2.4.

The differential capabilities of the integrated microsystem are illustrated by comparing the bead signals to Figure 4.18b, where I show signals recorded from a whole blood sample diluted 2,000-fold in buffer (again with a PBS lysis flow). Thus, erythrocytes remain intact, and are diluted to a sufficiently low level to measure individually. In this scatterplot, a dominant population is obvious around {0.01, 1.5} corresponding to the highly abundant red blood cells. This assignment is based on erythrocytes being the main

component in this sample, and by comparing the size-sensitive low-frequency component to that from the $\phi = 6$ µm particles (which are expected to have a slightly lower volume) in (a). The significantly lower membrane-sensitive signal component is also expected for cells due to their core-shell nature, and clearly differentiates them from the solid-core beads. The long tail at {..., 1.5} is likely due to erythrocyte clustering and coincidence – akin to the particle observations, such events only increase the measured low-frequency component compared to single cell/particle detection. The final interesting feature in this plot is the low-density yet distinguishable cluster of signals around {0.02, 1}. This is attributable to leukocyte signals, which are 1,000-fold less abundant compared to the erythrocytes, roughly matching the ratio in event counts here, and are expected to present lower signals in the high-frequency component. I should note that certainty of such assignments would require independent optical validation of the respective cell passage events, which my experimental design does not allow for. However, the existing bodies of literature on hematology and impedance cytometry provide a solid foundation to analyze my data.

In Figure 4.19, I finally consider the same whole blood sample from the clozapine measurement in Figure 4.17, further analyzed in the impedance cytometer for white blood cells after undergoing on-chip osmotic lysis. The marked difference in signal distribution compared to both control experiments is immediately obvious. Three populations (I-III) can easily be identified. Based on a comparison with the dilute whole blood control in Figure 4.18, I attribute cluster (I) to surviving erythrocytes and associated debris, with the latter presumably also accounting for the tail of signals toward the upper left quadrant. The clusters (II) and (III) with smaller high-frequency signals in turn most likely correspond to leukocytes. Unlike the control experiment, however, most red blood cells have been lysed, more clearly revealing the putative white blood cell signals. I should note that the comparison with the dilute whole blood sample has to remain qualitative; the quantitative values on both axes depend on the conductivity of the electrolyte (which does

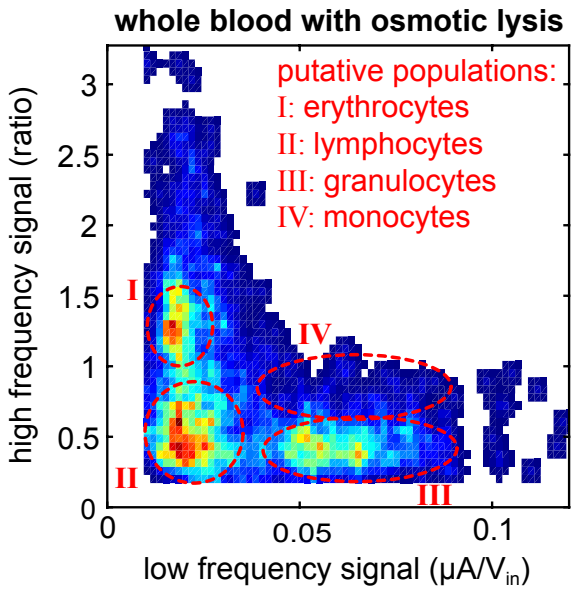


Figure 4.19: White blood cell monitoring. Scatterplots of impedance signals $\Delta Z$ at 90 kHz ($x$-axis; size-sensitive) and 900 kHz ($y$-axis; membrane-sensitive; corrected for size-based effects), with colors corresponding to the local event density from low (blue) to red (high), for a whole blood sample with on-chip, reagent-free DI water lysis. Due to the complexity of the plot, mild data smoothing was applied for better visualization.

not cancel out for the $\Delta Z$ measured here as opposed to the $|\Delta Z|$ analyzed in the previous Chapter). This is altered drastically with osmotic lysis from DI water, as compared to buffer solution in the control.

Looking more closely at the leukocytes, cell populations likely corresponding to white blood cell sub-types can be distinguished. Cluster (II), just slightly higher on the size-sensitive $x$-axis than the red blood cells, matches well with the expectations for lymphocytes. Cluster (III) corresponds to much larger cells, and therefore matches well with granulocytes. Finally, the less numerous population (IV) with similar sizes to those in (III), but larger high-frequency component, can tentatively be assigned to monocytes. While the overall distribution largely agrees with that observed by Holmes *et al.* for purified cell populations and without hydrodynamic focusing, the population (IV) is notably absent in their experiments [55]. Interestingly, Han *et al.*, do observe such a low-density tail when employing reagent-based lysis (albeit at smaller, instead of larger, high-frequency ratios compared to granulocytes) [56]. Therefore, it appears that DI water-

based osmotic lysis combined with hydrodynamic focusing is capable of yielding enhanced population differentiation akin to reagent-based approaches. In combination with the upstream electrochemical clozapine detection, the results here clearly demonstrate the concurrent cellular/acellular monitoring capabilities of my system.

### 4.2.6 Synopsis

I presented the first integrated microsystem for concurrent cellular/acellular sensing in whole blood samples. This was enabled by series integration of the highly sensitive electrochemical chitosan-CNT/graphene clozapine sensor and the impedance cytometer with osmotic lysis and hydrodynamic focusing. For the redox catalysis system, I demonstrated that utilization directly in whole blood samples is feasible, and performance does not degrade significantly compared to serum samples, with signal losses fully explained by the lower available clozapine concentration in identical volumes of blood and serum. For impedance cytometry, I evaluated readout and measurement circuitry to enable differential blood cell characterization. The overall performance of the system was validated with whole blood samples spiked with clozapine, showing data for both analytes from the same lab-on-a-chip.

## 4.3 Chapter Summary

In this Chapter, I have explored the microsystems integration for concurrent cellular/acellular sensing in parallel and in series. For the former, I have investigated plasma skimming in a proof-of-concept immunoassay with impedimetric readout. I have employed this fully portable microsystem for the direct, label-free detection of 150 nM antibodies from whole blood samples, a first in the literature. My preceding plasma skimming optimization study has revealed discrepancies in the existing literature on the topic, and has shown that long-term operation is infeasible with the pursued

design approach. In the process, I have also derived proper strategies for handling whole blood samples in glass/PDMS microfluidic devices. Based on these results, I have pursued series integration of the sensing modalities. In this fully integrated microdevice, I have demonstrated direct electrochemical detection of clozapine followed by impedance cytometry to obtain white blood cell counts from the same blood samples. With these results, I have confirmed the feasibility of concurrent cellular/acellular monitoring with lab-on-a-chip technology, particularly with regard to clozapine treatment monitoring.

# Chapter 5

# Conclusion

## 5.1 Highlights

- Novel chitosan-enabled approaches to detect clozapine
  - Suitable for miniaturization
  - Thorough understanding of material & electrochemical parameter space
    - Reusability, storage, diffusion, reaction kinetics, alternative electrode materials, …
  - Detection limits compatible with clinical requirements
  - First example of direct redox detection in serum
  - Selectivity studies reveal advantages and drawbacks of both chitosan-catechol and chitosan-CNT/graphene
- First systems integration studies of hydrodynamic focusing and osmotic lysis with impedance cytometry
  - Focusing increases sensitivity up to 5-fold
    - Integrated models developed
    - Geometry variations investigated
    - Importance of diffusion highlighted
  - Osmotic lysis compatible and 99.92% efficient
    - Various failure regimes identified from online detection capabilities

  - Enables label and chemical-free impedance cytometry towards point-of-care white blood cell counting
- First system for label-free concurrent cellular/acellular monitoring in whole blood
  - Found plasma skimming unreliable for continuous operation
  - Developed protocols for whole blood sample handling
  - Performance of redox catalysis system is conserved at the micro-scale and for whole blood samples
  - Impedance cytometer with osmotic lysis and flow focusing capable of differential white blood cell analysis
- Integrated system demonstrates feasibility of point-of-care monitoring for clozapine adherence, efficacy, and safety

## 5.2 Summary

My dissertation has presented a study of microsystems integration towards point-of-care monitoring of clozapine treatment for adherence, efficacy, and safety. I have initially investigated distinct novel electrochemical techniques to measure clozapine in complex biological samples by leveraging biomaterials to enhance selectivity and sensitivity. I have further studied the systems interplay between key components in label- and reagent-free white blood cell counters – impedance cytometry, hydrodynamic focusing, and osmotic lysis – in depth. Furthermore, I have evaluated integration approaches for concurrent detection of both these cellular and acellular biomarkers. Leveraging the knowledge gained from these efforts, I have implemented and validated the series-type integration approach shown in Figure 5.1 to for the first time concurrently monitor clozapine and white blood cells in whole blood samples.

For clozapine detection, I have employed the biopolymer chitosan as a facile matrix to confer sensing functionalities. I have demonstrated that the redox cycling system, where catechol is grafted to the chitosan to allow for repeated oxidation and reduction of clozapine, yields significant gains in sensitivity and detection limit. These advantages

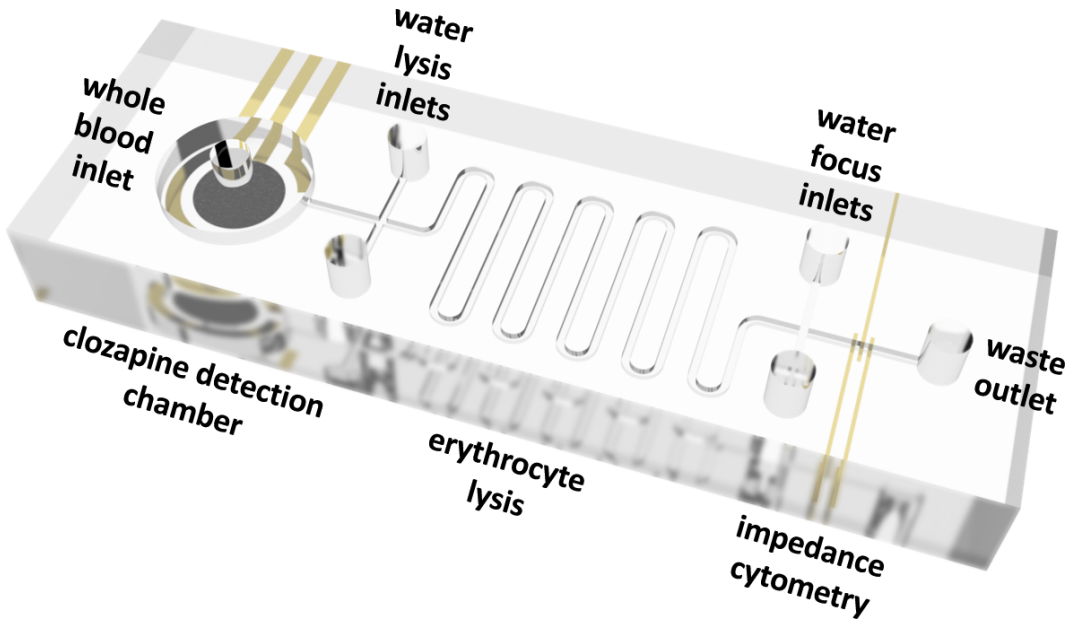


Figure 5.1: Schematic rendering of the integrated microsystem developed in this thesis.

are conserved even in complex biological samples like human serum, with an LOD below the lower therapeutically relevant limit of 1 µM. By investigating diffusion and electron transfer mechanisms, I have shown that the films further confer selectivity between clozapine and its highly analogous metabolite norclozapine due to electrostatic interactions. Other aspects relevant to lab-on-a-chip integration, such as the impact of film storage and the electrode material, have also been assessed. As an alternative approach, I have presented chitosan composite films with CNTs and/or graphene. This redox catalysis system has been shown to drastically enhance the sensitivity and detection limit of clozapine, again to below 1 µM in clinical samples, as well as the selectivity with respect to the dominant endogenous interferent uric acid.

Regarding white blood cell counting, I have explored the systems interplay between impedance cytometry and hydrodynamic focusing. The extensive study in models as well as particle experiments has validated the approach to provide an up to 5-fold gain in sensitivity due to the virtual aperture from non-conductive sheath flows. Compared to a physically smaller channel, this significantly reduces the risk of channel clogging from larger cells or aggregates. Furthermore, diffusion has been shown to play an important

role in the performance of this integrated system, in spite of a high Péclet number. Focus channel geometries, on the other hand, have been shown to only be of secondary importance. I have also explored integration of impedance cytometry and osmotic lysis. I have assessed the conditions necessary and sufficient for lysis of erythrocytes with DI water, and found it up to 99.9% effective. Overall, the approach has been shown to enable white blood cell analysis without the need for either labels or reagents.

For a fully integrated microsystem solution, I have considered two approaches for concurrent cellular and acellular whole blood monitoring. I have studied parallel integration employing plasma skimming – exploiting purely hydrodynamic phenomena for blood/plasma separation – in a proof-of-concept label-free impedimetric immunoassay. For a manually actuated lab-on-a-chip with portable readout electronics, detection of 150 nM antibodies in whole human blood has been demonstrated for the first time. I have further derived procedures to minimize blood clotting and platelet aggregation inside traditional microdevices for extended research use. However, plasma skimming has been found to have a brief functional lifetime even under optimized conditions. I have thus implemented series integration, where whole blood enters a clozapine sensing chamber and continues into the white blood cell analyzer. For the latter, I have evaluated instrumentation options with regards to system compatibility, particularly concerning the decreasing conductivity from hydrodynamic focusing. In the integrated microsystem, detection of clozapine spiked into whole blood samples flowing through the device has been demonstrated employing the redox catalysis system. Moreover, white blood cell differentiation capabilities have been shown, validating the feasibility of concurrent cellular/acellular biomarker monitoring in clozapine treatment with lab-on-a-chip microsystems.

## 5.3 Future Work

The research presented in this dissertation serves as a significant step toward point-of-care monitoring of clozapine treatment. However, further work is called for to advance and refine components, as well as to fully translate the microsystem into clinical practice.

Clozapine Detection

As discussed in Chapter 2, chitosan-catechol, platinum black, and chitosan-CNT/graphene all offer unique advantages (and drawbacks) for clozapine detection. I chose the latter for my demonstration of concurrent acellular/cellular monitoring system due to its high sensitivity. To realize the full potential of these sensors and overcome their limitations, future work should pursue a multi-sensor chemometrics approach. This involves combining the signals from two or more orthogonal sensing modalities – *i.e.* ones based on different mechanisms and thus providing independent information – utilizing techniques such as partial least squares regression or artificial neural networks. It is similar in concept to how the human tongue or nose are able to differentiate thousands to millions of tastes and smells with only a very limited set of receptors. As part of the MiND project, my collaborators – particularly Sheryl Chocron – and I already noted the need for this and pursued initial work in this direction [99,100]. We demonstrated that even with a single sensor, these chemometric techniques could enhance performance by utilizing all available information (instead of simply peak current and potential). Integrating the chitosan-catechol and chitosan-CNT/graphene composite films as shown in Figure 5.2 should ultimately enable sensitive detection of clozapine as well as selectivity with respect to norclozapine. Through further extension of the array, our understanding of a patient's status can be enhanced even further, something that may be especially important when a disease is complex and incompletely understood.

My results also suggest some immediate avenues for developing new sensing modalities for such arrays from the ones investigated. While I only employ homogeneous

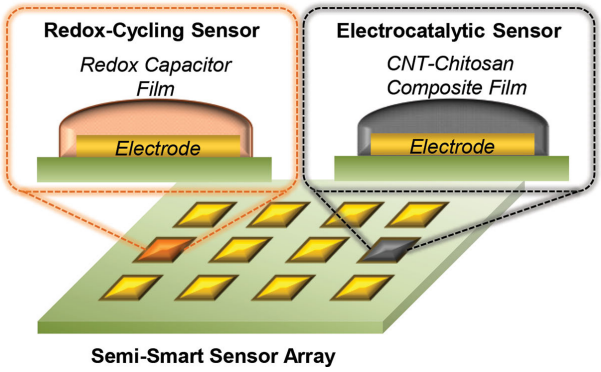


Figure 5.2: Schematic of the arrayed sensing concept to achieve synergistic clozapine detection performance. Reproduced with permission from [99].

chitosan films in my work, my collaborators have previously shown facile fabrication of heterogeneous multilayer structures [85]. Since I found that diffusion through chitosan allows for differentiation of clozapine and norclozapine, coating a chitosan-CNT/graphene film with a further layer of unmodified chitosan may confer such selectivity to the redox catalysis system. Further modification with catechol may add additional signal amplification in a combined catalysis/cycling system, although the experiments with platinum electrodes suggest that there is a trade-off between these mechanisms.

Lastly, a single-purpose clozapine test as shown in Figure 5.3 may offer additional benefits worth pursuing over the short term. With clozapine detection in whole blood samples established, a concept directly mirroring that of a glucose meter could be implemented, where a drop of blood is applied directly to the sensor or sensor array. Such an approach eliminates the need for microfluidics, and thus also microfabrication and assembly – with only an open, planar electrochemical cell, low-cost screen-printing becomes feasible. The similarity to the glucose meter concept may also simplify regulatory approval and thus provide a bridge solution until a fully integrated system becomes available [1].

### Systems Integration

Toward a true point-of-care device, notable further systems integration needs

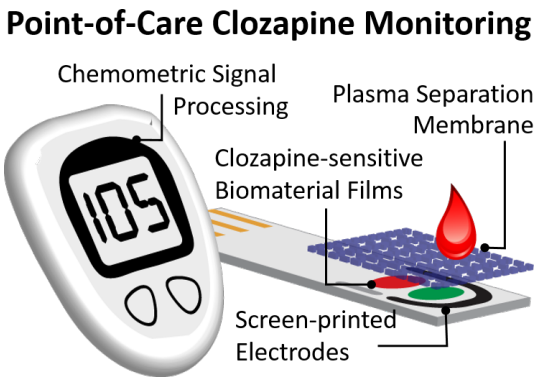


Figure 5.3: Schematic of a single-purpose at-home clozapine monitoring concept.

involve the fluid handling and actuation as well as the signal readout [52]. The latter presents challenges, but not necessarily systems integration challenges – the precise nature of the electronics will not affect other aspects of a device, though the device requirements certainly have to inform the specifications as observed in Subsection 4.2.4. For impedance cytometry, this has been realized with custom-made CMOS [167] or with off-the-shelf components [168,169]. While designed for frequency sweeps and thus limited in data acquisition speed, the commercial AD5933 impedance analyzer is available for less than $10 and can be sufficient for cytometry in certain (slow flow, single frequency) cases [160]. Analog Devices further offers the newer, similarly priced ADuCM350, which offers both impedance measurement capabilities as well as potentiostat functionality for electrochemical measurements [170]. For electrochemistry alone, the somewhat less stringent electronics requirements and the broader applicability has further lead to wide availability of commercial handheld potentiostats, illustrating the relative ease of miniaturization.

A primary concern regarding fluid handling is preventing a fingerstick blood sample from coagulating or aggregating. While I have successfully avoided other reagents in my research this particular challenge requires a chemical solution. As above, this can be investigated independently of other components. One possibility is to adopt a persistent surface coating that reduces platelet activation, akin to the Pluronic F-68 coating to inhibit

surface fouling. PDMS microfluidics modified with polybetaine, for instance, have been shown to inhibit coagulation [171]; heparin has been similarly employed [172]. Another possibility is to coat the surface of the blood sample receptacle – a necessary component in an eventual point-of-care device – with a dry form of the requisite chemicals. The reagents would dissolve in the sample upon contact, much like in standard blood collection tubes.

Fluid actuation, on the other hand, does have the potential for interactions with other aspects of the device – even in traditional benchtop syringe pumps, motor stepping and the resulting pulsatile flow are well-established factors in flow control. Current trends in microfluidics favor capillary flow-driven devices for the point of care as they eliminate the need for additional components [173]. For my system, they also offer the greatest systems integration challenges due to the need for multiple well-controlled flows. Akin to the plasma skimming design challenge in Section 4.1 in reverse, the channel dimensions would require careful design to achieve the necessary flow ratios in all branches of the network toward the shared outlet. While theoretically possible, in practice this approach would likely be too sensitive to disruption. The same arguments apply to the other available passive approach, gravity-driven flow [52]. Capillary force could still be useful for sample loading akin to what is employed in the Chempaq XBC cartridge [69]. For actuation, however, active approaches will likely be more promising. The literature offers numerous examples for integration of such into microfluidic lab-on-a-chip systems [52,174,175]. The main strategies are either mechanical or electrical. A classic example of the former are peristaltic pumps implemented in multi-layer PDMS systems through successive valves that close and open to yield a net positive flow. Many other mechanisms have been presented; their main shared drawback is the added fabrication complexity, and – akin to syringe pumps – their not perfectly continuous flow. Electrical pumps rely on electroosmotic flow and are significantly more robust due to the lack of moving parts, with fabrication processes also only requiring the comparatively simple addition

of electrodes. However, complexities in the resulting flow profiles – which depend on the zeta potentials of all materials involved – need to be kept in mind. In either case, having pumps integrated into the microsystem allows for employing them not just for flow actuation, but also for drawing a drop of blood into the device. Integrating these components with batteries and requisite control electronics will ultimately yield a device suitable for point-of-care use at the pharmacy or doctor's office to monitor clozapine treatment.

## 5.4 Conclusion

My dissertation research has yielded notable contributions to relevant fields across the three main Chapters. The understanding of biomaterial application toward electrochemical sensing may enable detection of other compounds lacking specific biorecognition elements using similar approaches. The knowledge on the molecular properties of clozapine such as diffusion, electron transfer and electrophoretic transport can open up additional avenues for its detection. Elucidating the systems interplay between impedance cytometry, hydrodynamic focusing, and red blood cell lysis is critical toward designing highly sensitive label-free cell- or particle counters. The studies further serve as a showcase of how typically neglected phenomena, such as diffusion, can have outsize effects in these integrated microfluidic systems, highlighting the need for in-depth theoretical and experimental investigations of this type in designing them. Moreover, this research clarifies fundamental compatibility and testing aspects towards analysis of human blood samples using microfluidic approaches.

My lab-on-a-chip platform, which successfully integrates clozapine and white blood cell detection abilities in a microsystem while employing simple fabrication techniques and limiting the use of chemical reagents, represents a considerable technological advance. The final integrated microsystem paves the way toward revolutionizing care of millions of patients with treatment-resistant schizophrenia, including many not currently receiving

clozapine. Monitoring capabilities for safety, efficacy, and adherence in a single, small package make it an attractive use case for the point of care, decreasing costs and patient burden and changing the paradigm of how we currently monitor clozapine treatment. From its intended purpose of lowering the barriers to the use of clozapine, this system can further be adapted to other applications that require simultaneous monitoring of both cellular and acellular blood biomarkers, extending its impact. Ultimately, this initial application of real-time monitoring of psychiatric drug treatment provides a systems-oriented model for further development of next generation personalized medical care devices.

# Chapter 6

# Appendices

## 6.1 Appendix A: Photomasks

All photomasks are reproduced at a 1:1 scale here, and were generally printed at 25,400 dpi on transparency foil unless noted otherwise. Some of the extremely fine feature are unlikely to be reproduced correctly herein when printed.

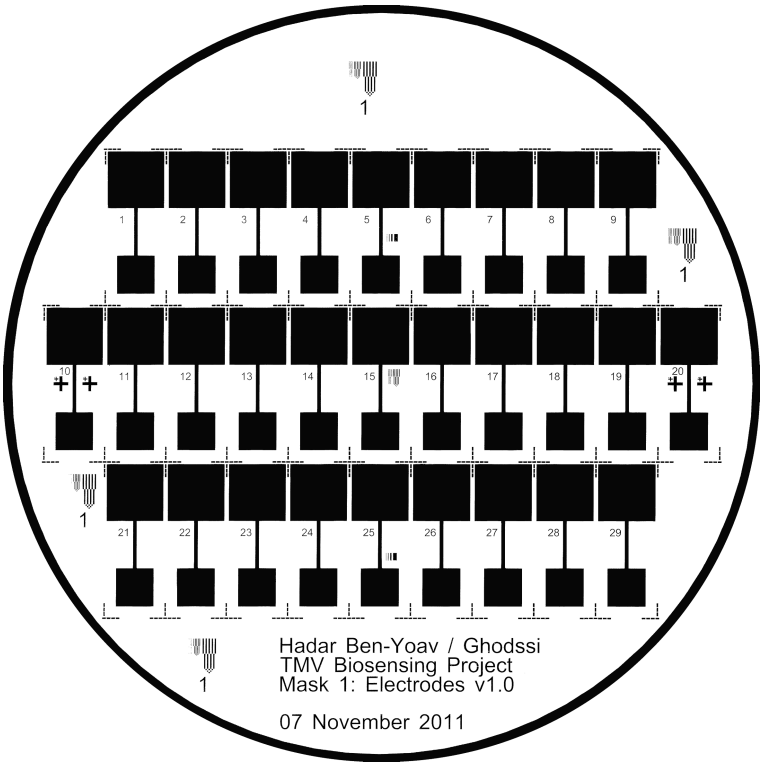


Figure 6.1: Photomask for 29 planar electrochemistry working electrodes with a surface area of $7.5 \times 7.5$ mm² or $5 \times 5$ mm², depending on the orientation utilized.

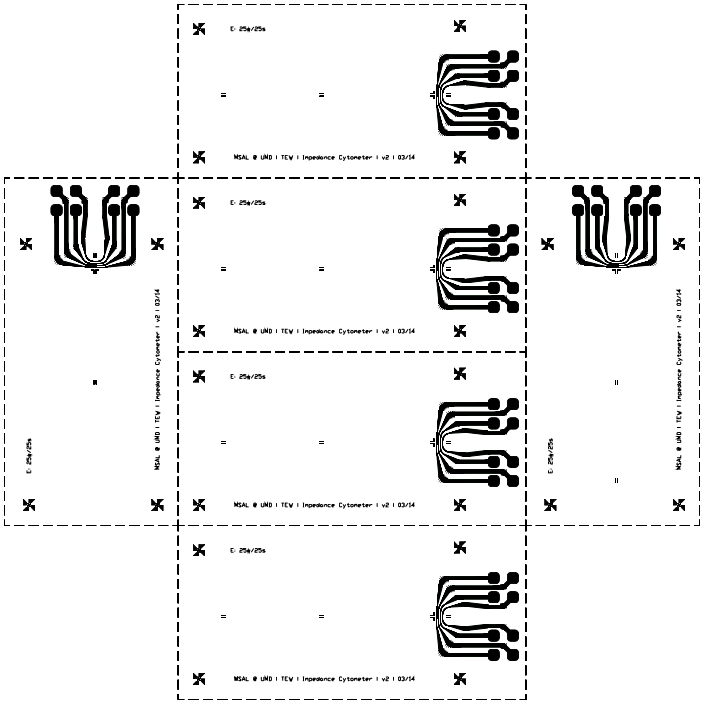


Figure 6.2: Photomask for six chips with co-planar impedance cytometry electrodes of 25 µm length and gap.

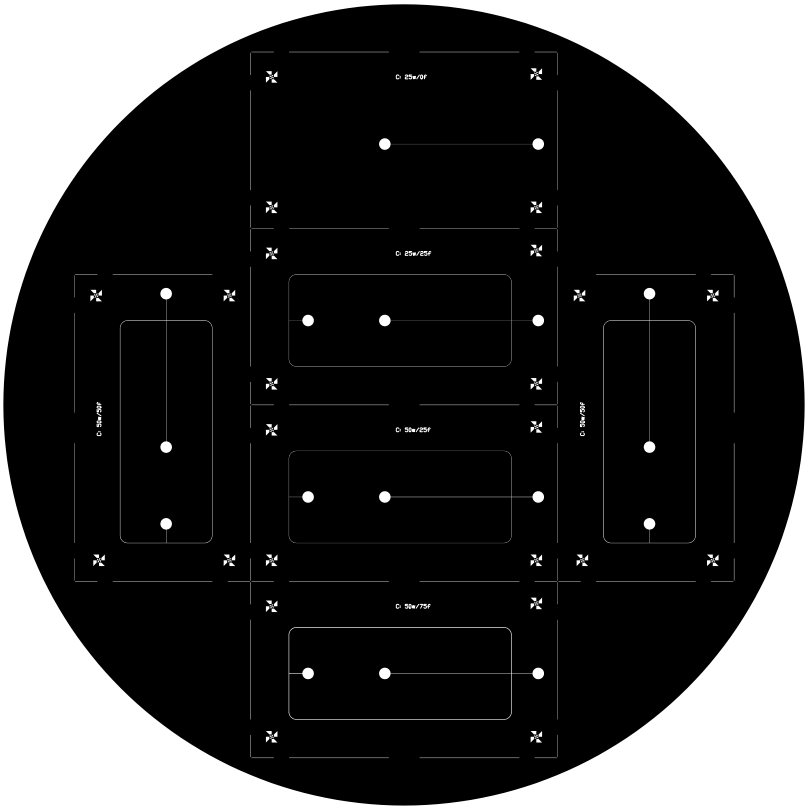


Figure 6.3: Photomask for microfluidic mold to yield six chips for hydrodynamic focusing with 25 μm (ultimately not utilized in this work) or 50 μm wide center channels and 25 μm, 50 μm, or 75 μm wide focus channels.

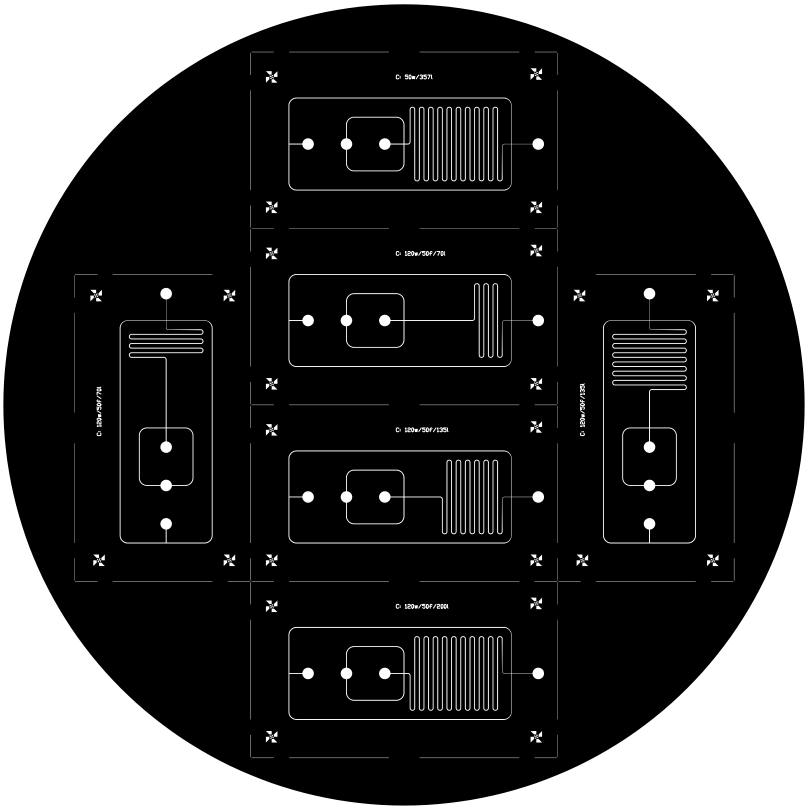

Figure 6.4: Photomask for microfluidic mold to yield six chips for osmotic lysis with 120 µm wide channels (50 µm in measurement region close to outlet) with serpentine channel lengths of 70 mm, 135 mm, or 200 mm. Hydrodynamic focusing channels of 25 µm width are included as well, but not opened up in the osmotic lysis study.

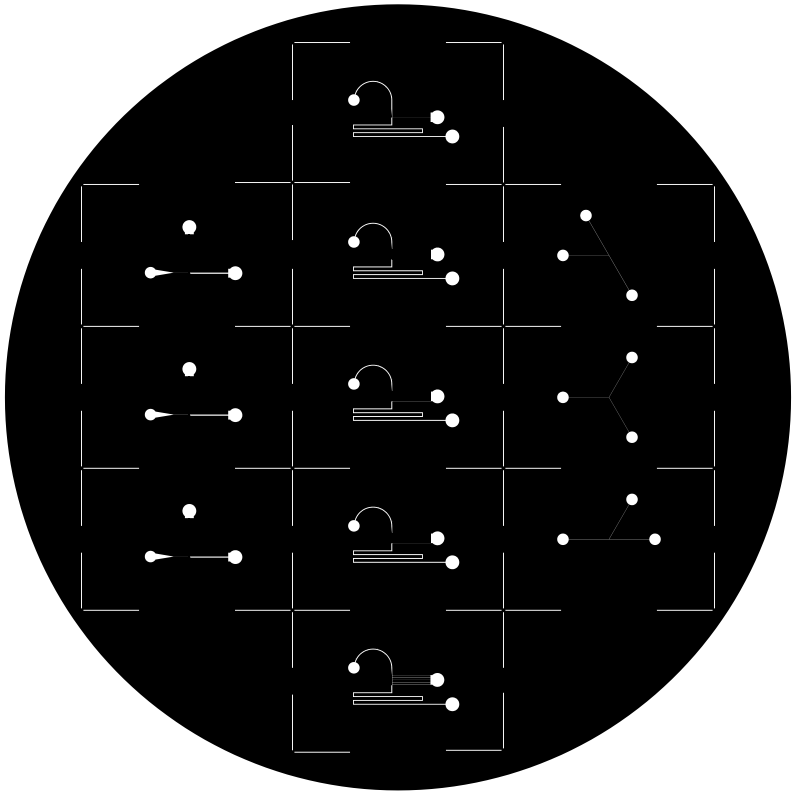

Figure 6.5: Photomask for microfluidic mold to yield plasma skimming channels as per the design published by Yang *et al.* (left 3 chips) and as per the theoretical design rules from the same paper (center 5 chips). The rightmost designs were intended as test structures.

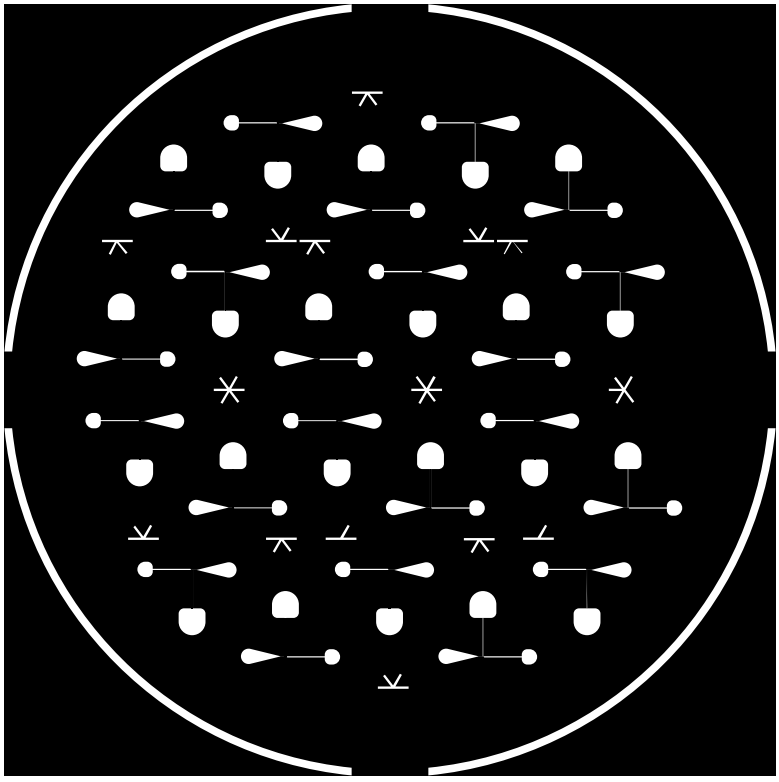

Figure 6.6: Photomask for microfluidic mold to yield plasma skimming channels as per the design published by Yang *et al.* with small variations in cell outlet channel geometries and number of plasma skimming channels. This mask was implemented as chrome-on-glass with a 1.5 μm resolution.

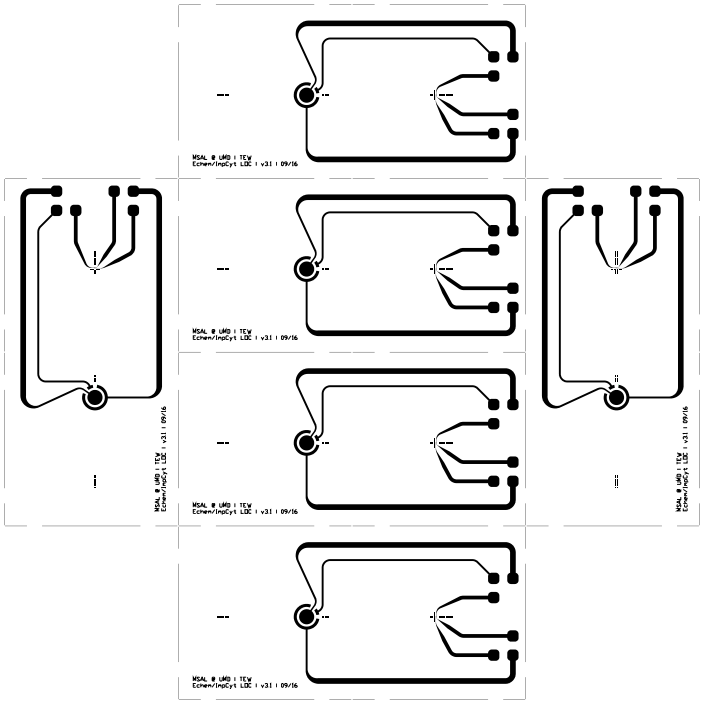

Figure 6.7: Photomask for six chips with co-planar impedance cytometry electrodes of 25 µm length and gap, integrated with 3-electrode electrochemical cells (2 mm diameter working electrode).

# Appendix B: Analytical Model for Impedance Cytometry with Hydrodynamic Focusing

Reproduced with permission from T. E. Winkler et al., Microfluid. Nanofluidics 2016, 20, 134.

## Definitions

***Note: All values are in SI units***

```
Needs["Notation`"];
Symbolize[ __ ];
```

### Physical Constants

```
ε₀ = QuantityMagnitude[UnitConvert[1 ε₀]];
k_B = QuantityMagnitude[UnitConvert[1 k]];
N_A = QuantityMagnitude[UnitConvert[1 N_A]];
q_e = QuantityMagnitude[UnitConvert[1 e]];
```

### Define parameter list for array to hold cellular information, and define exemplary array "cell"

```
ϕ = 1; t = 2; σ_mem = 3; ε_mem = 4; σ_cyt = 5; ε_cyt = 6;
cell = {10 * 10^-6, 5 * 10^-9, 10^-8, 11.3 ε₀, 0.6, 60 ε₀};
```

### Define parameter list for array to hold channel and electrode geometry information, and define exemplary array "geom"

```
w = 1; h = 2; l = 3; g = 4;
geom = {50 * 10^-6, 20 * 10^-6, 25 * 10^-6, 25 * 10^-6};
```

### Define parameter list for array to hold liquid medium information, and define exemplary arrays "sample" and "sheath";
### "wflow" defines the width that a particular fluid occupies in the channel, and "type" whether it is the central sample or side sheath flow

```
wflow = 1; Q = 2; σ_med = 3; ε_med = 4; IS = 5; type = 6;
sample = {VA, 20 / 3.6 * 10^-12, 1.6, 78 ε₀, 160, "sample"};
sheath = {geom[[w]] - VA, 20 / 3.6 * 10^-12, 0.055 * 10^-6, 78 ε₀, 10^-4, "sheath"};
```

### Define measurement and environmental parameters

```
f = 100 000;
ω = 2 π f;
Temperature = 298.15;
```

## Analytical Hydrodynamic Focusing Model

### Relates flow ratio *FR* to virtual aperture width *VA*

### Adapted from Ref. [1]

$$FR = \frac{\text{sample}[[Q]]}{\text{sample}[[Q]] + \text{sheath}[[Q]]};$$

$$\gamma[VA\_?\text{NumberQ}] := \left(1 - \left(\frac{192\,\text{geom}[[h]]}{VA\,\pi^5}\right)\right.$$
$$\left.\text{NSum}\left[\left(\frac{\text{Sinh}\left[(2n+1)\,\pi\,VA \,/\, (2\,\text{geom}[[h]])\right]}{(2n+1)^5\,\text{Cosh}\left[(2n+1)\,\pi\,\text{geom}[[w]] \,/\, (2\,\text{geom}[[h]])\right]}\right),\ \{n,\ 0,\ \infty\}\right]\right) \Big/$$
$$\left(1 - \left(\frac{192\,\text{geom}[[h]]}{\text{geom}[[w]]\,\pi^5}\right)\text{NSum}\left[\left(\frac{\text{Tanh}\left[(2n+1)\,\pi\,\text{geom}[[w]] \,/\, (2\,\text{geom}[[h]])\right]}{(2n+1)^5}\right),\ \{n,\ 0,\ \infty\}\right]\right);$$

$$VA = x\ /.\ \text{FindRoot}\left[FR == \frac{x}{\text{geom}[[w]]}\,\gamma[x],\ \{x,\ \text{geom}[[w]]\,/\,2\}\right];$$

## Analytical Electrodynamic Model

### Schwarz–Christoffel Mapping to account for co-planar arrangement of the electrodes

### Adapted from Ref. [2]

$$T_{Ac}[\text{geom}\_] := \text{Cosh}\left[\frac{\pi\,(\text{geom}[[g]] + 2\,\text{geom}[[l]])}{4\,\text{geom}[[h]]}\right]^2;$$

$$T_{Bc}[c\_] := \text{Cosh}\left[\frac{\text{geom}[[g]]\,\pi}{4\,\text{geom}[[h]]}\right]^2;$$

$$T_{Cc} = 1;$$

$$T_{Dc} = 0;$$

$$m_c[\text{geom}\_] := \frac{(T_{Bc}[\text{geom}] - T_{Cc})\,(T_{Ac}[\text{geom}] - T_{Dc})}{(T_{Ac}[\text{geom}] - T_{Cc})\,(T_{Bc}[\text{geom}] - T_{Dc})};$$

$$\varkappa[\text{geom}\_, \text{med}\_] := \text{med}[[\text{wflow}]]\,\frac{\text{EllipticK}[1 - m_c[\text{geom}]]}{2 * \text{EllipticK}[m_c[\text{geom}]]};$$

$$V[\text{geom}\_, \text{med}\_] := \varkappa[\text{geom}, \text{med}]\,(\text{geom}[[g]] + 2\,\text{geom}[[l]])\,\text{geom}[[h]];$$

### Volume & Volume Fraction of the particle

## When considering the sample phase, use spherical segment delineated by *VA;* when considering sheath phase, use corresponding spherical caps

```
P[cell_, med_] := Switch[med[[type]], "sample",
    1/12 π Min[VA, cell[[ø]]] (3 cell[[ø]]^2 - Min[VA, cell[[ø]]]^2), "sheath",
    1/6 π cell[[ø]]^3 - 1/12 π Min[VA, cell[[ø]]] (3 cell[[ø]]^2 - Min[VA, cell[[ø]]]^2)
  ] ;
Φ[cell_, geom_, med_] := P[cell, med] / V[geom, med];
```

## Calculation of Electrodynamic Parameters for Equivalent Circuit Adapted from Ref. [3] and Ref. [4]

```
γcell[cell_] := cell[[ø]] / (cell[[ø]] - 2 cell[[t]]);
a1[cell_, geom_, med_] :=
  γcell[cell]^3 (cell[[εcyt]] + 2 cell[[εmem]]) ((cell[[εmem]] + 2 med[[εmed]]) +
      2 Φ[cell, geom, med] (cell[[εmem]] - med[[εmed]])) + 2 (cell[[εcyt]] - cell[[εmem]])
    ((cell[[εmem]] - med[[εmed]]) + Φ[cell, geom, med] (2 cell[[εmem]] + med[[εmed]]));
a2[cell_, geom_, med_] := γcell[cell]^3 (cell[[εcyt]] + 2 cell[[εmem]])
    ((cell[[σmem]] + 2 med[[σmed]]) + 2 Φ[cell, geom, med] (cell[[σmem]] - med[[σmed]])) +
  γcell[cell]^3 (cell[[σcyt]] + 2 cell[[σmem]])
    ((cell[[εmem]] + 2 med[[εmed]]) + 2 Φ[cell, geom, med] (cell[[εmem]] - med[[εmed]])) +
  2 (cell[[εcyt]] - cell[[εmem]]) ((cell[[σmem]] - med[[σmed]]) +
      Φ[cell, geom, med] (2 cell[[σmem]] + med[[σmed]])) + 2 (cell[[σcyt]] - cell[[σmem]])
    ((cell[[εmem]] - med[[εmed]]) + Φ[cell, geom, med] (2 cell[[εmem]] + med[[εmed]]));
a3[cell_, geom_, med_] := γcell[cell]^3 (cell[[σcyt]] + 2 cell[[σmem]])
    (cell[[σmem]] (1 + 2 Φ[cell, geom, med]) + 2 med[[σmed]] (1 - Φ[cell, geom, med])) +
  2 (cell[[σcyt]] - cell[[σmem]])
    (cell[[σmem]] (1 + 2 Φ[cell, geom, med]) - med[[σmed]] (1 - Φ[cell, geom, med]));
b1[cell_, geom_, med_] := γcell[cell]^3 (cell[[εcyt]] + 2 cell[[εmem]])
    ((cell[[εmem]] + 2 med[[εmed]]) - Φ[cell, geom, med] (cell[[εmem]] - med[[εmed]])) +
  (cell[[εcyt]] - cell[[εmem]])
    (2 (cell[[εmem]] - med[[εmed]]) - Φ[cell, geom, med] (2 cell[[εmem]] + med[[εmed]]));
b2[cell_, geom_, med_] := γcell[cell]^3 (cell[[εcyt]] + 2 cell[[εmem]])
    ((cell[[σmem]] + 2 med[[σmed]]) - Φ[cell, geom, med] (cell[[σmem]] - med[[σmed]])) +
  γcell[cell]^3 (cell[[σcyt]] + 2 cell[[σmem]])
    ((cell[[εmem]] + 2 med[[εmed]]) - Φ[cell, geom, med] (cell[[εmem]] - med[[εmed]])) +
  (cell[[εcyt]] - cell[[εmem]]) (2 (cell[[σmem]] - med[[σmed]]) -
      Φ[cell, geom, med] (2 cell[[σmem]] + med[[σmed]])) + (cell[[σcyt]] - cell[[σmem]])
    (2 (cell[[εmem]] - med[[εmed]]) - Φ[cell, geom, med] (2 cell[[εmem]] + med[[εmed]]));
b3[cell_, geom_, med_] := γcell[cell]^3 (cell[[σcyt]] + 2 cell[[σmem]])
    (cell[[σmem]] (1 - Φ[cell, geom, med]) + med[[σmed]] (2 + Φ[cell, geom, med])) +
  (cell[[σcyt]] - cell[[σmem]])
    (2 cell[[σmem]] (1 - Φ[cell, geom, med]) - med[[σmed]] (2 + Φ[cell, geom, med]));
```

```
c1[cell_, geom_, med_] := med[[εmed]] a2[cell, geom, med] + med[[σmed]] a1[cell, geom, med] -
    med[[εmed]] a1[cell, geom, med] b2[cell, geom, med] / b1[cell, geom, med];
c2[cell_, geom_, med_] := med[[εmed]] a3[cell, geom, med] + med[[σmed]] a2[cell, geom, med] -
    med[[εmed]] a1[cell, geom, med] b3[cell, geom, med] / b1[cell, geom, med];
c3[cell_, geom_, med_] := med[[σmed]] a3[cell, geom, med];
s3[cell_, geom_, med_] := 1 / (2 b1[cell, geom, med]) (-b2[cell, geom, med] +
      √(b2[cell, geom, med]^2 - 4 b1[cell, geom, med] b3[cell, geom, med]));
s4[cell_, geom_, med_] := 1 / (2 b1[cell, geom, med]) (-b2[cell, geom, med] -
      √(b2[cell, geom, med]^2 - 4 b1[cell, geom, med] b3[cell, geom, med]));
s5[cell_, geom_, med_] := 1 / (2 c1[cell, geom, med]) (-c2[cell, geom, med] +
      √(c2[cell, geom, med]^2 - 4 c1[cell, geom, med] c3[cell, geom, med]));
s6[cell_, geom_, med_] := 1 / (2 c1[cell, geom, med]) (-c2[cell, geom, med] -
      √(c2[cell, geom, med]^2 - 4 c1[cell, geom, med] c3[cell, geom, med]));
k1[cell_, geom_, med_] := c1[cell, geom, med] s5[cell, geom, med] s6[cell, geom, med] /
    (b1[cell, geom, med] s3[cell, geom, med] s4[cell, geom, med]);
k2[cell_, geom_, med_] :=
  (1 / (b1[cell, geom, med] s3[cell, geom, med] (s3[cell, geom, med] - s4[cell, geom, med])))
   c1[cell, geom, med] (s3[cell, geom, med] - s5[cell, geom, med])
    (s3[cell, geom, med] - s6[cell, geom, med]);
k3[cell_, geom_, med_] := (1 / (b1[cell, geom, med] s4[cell, geom, med]
       (s4[cell, geom, med] - s3[cell, geom, med]))) c1[cell, geom, med]
    (s4[cell, geom, med] - s5[cell, geom, med]) (s4[cell, geom, med] - s6[cell, geom, med]);
τ1[cell_, geom_, med_] := -1 / s3[cell, geom, med];
τ2[cell_, geom_, med_] := -1 / s4[cell, geom, med];

Δε1[cell_, geom_, med_] := k2[cell, geom, med] τ1[cell, geom, med];
Δε2[cell_, geom_, med_] := k3[cell, geom, med] τ2[cell, geom, med];
σ0[cell_, geom_, med_] := k1[cell, geom, med];
ε∞[cell_, geom_, med_] := med[[εmed]] a1[cell, geom, med] / b1[cell, geom, med];
```

## Equivalent Circuit Elements

## Adapted from Ref. [4]

$$R_{mem}[cell\_, geom\_, med\_] := \frac{1}{\kappa[geom, med]}$$
$$\left(\frac{\tau_1[cell, geom, med] + \tau_2[cell, geom, med]}{\Delta\varepsilon_1[cell, geom, med] + \Delta\varepsilon_2[cell, geom, med]} - \frac{1}{k_2[cell, geom, med] + k_3[cell, geom, med]} - \right.$$
$$\left.\left(\tau_1[cell, geom, med]\ \tau_2[cell, geom, med]\ \left(k_2[cell, geom, med] + k_3[cell, geom, med]\right)\right) / \left(\Delta\varepsilon_1[cell, geom, med] + \Delta\varepsilon_2[cell, geom, med]\right)^2\right);$$

$$C_{mem}[cell\_, geom\_, med\_] := \left(\tau_1[cell, geom, med]\ \tau_2[cell, geom, med]\ \left(k_2[cell, geom, med] + k_3[cell, geom, med]\right)\right) /$$
$$\left(\left(\Delta\varepsilon_1[cell, geom, med] + \Delta\varepsilon_2[cell, geom, med]\right) R_{mem}[cell, geom, med]\right);$$

$$R_{cyt}[cell\_, geom\_, med\_] := \frac{1}{\left(k_2[cell, geom, med] + k_3[cell, geom, med]\right) \kappa[geom, med]};$$

$$C_{cyt}[cell\_, geom\_, med\_] := \left(\Delta\varepsilon_1[cell, geom, med] + \Delta\varepsilon_2[cell, geom, med]\right) \kappa[geom, med];$$

$$R_{med}[cell\_, geom\_, med\_] := \frac{1}{\sigma_0[cell, geom, med]\ \kappa[geom, med]};$$

$$C_{med}[cell\_, geom\_, med\_] := \varepsilon_\infty[cell, geom, med]\ \kappa[geom, med];$$

## Ionic Double Layer Capacitor (Helmholtz Model)

$$\lambda_D[med\_] := \sqrt{\frac{med[[\varepsilon_{med}]] * k_B * Temperature}{2\ N_A * q_e^2 * med[[IS]]}};$$

$$C_{DL}[geom\_, med\_] := med[[wflow]] * geom[[l]]\ \frac{med[[\varepsilon_{med}]]}{\lambda_D[med]};$$

## Impedance for single liquid medium phase

## Adapted from Ref. [4] and Ref. [5]

$$Z_{mix}[cell\_, geom\_, med\_] :=$$
$$1 \Big/ \left(i\,\omega \left(\varepsilon_\infty[cell, geom, med] + \frac{\sigma_0[cell, geom, med]}{i\,\omega} + \frac{\Delta\varepsilon_1[cell, geom, med]}{1 + i\,\omega\,\tau_1[cell, geom, med]} + \right.\right.$$
$$\left.\left.\frac{\Delta\varepsilon_2[cell, geom, med]}{1 + i\,\omega\,\tau_2[cell, geom, med]}\right) \kappa[geom, med]\right) + \frac{2}{i\,\omega\,C_{DL}[geom, med]};$$

$$Z_{null}[cell\_, geom\_, med\_] := \frac{1}{i\,\omega\,med[[\varepsilon_{med}]]\,\kappa[geom, med] + med[[\sigma_{med}]]\,\kappa[geom, med]} +$$
$$\frac{2}{i\,\omega\,C_{DL}[geom, med]};$$

## Total and Relative Impedance with Hydrodynamic Focusing

$$Z[cell\_, geom\_] := \left(\frac{1}{Z_{mix}[cell, geom, sample]} + \frac{1}{Z_{mix}[cell, geom, sheath]}\right)^{-1};$$

$$Z_{empty}[cell\_, geom\_] := \left(\frac{1}{Z_{null}[cell, geom, sample]} + \frac{1}{Z_{null}[cell, geom, sheath]}\right)^{-1};$$

$$|\Delta Z|[cell\_, geom\_] := Abs\left[\frac{Z[cell, geom] - Z_{empty}[cell, geom]}{Z_{empty}[cell, geom]}\right];$$

## Sample Numerical Results

```
Z_empty[cell, geom]
Z[cell, geom] // N
|ΔZ|[cell, geom] // N
```

```
67528. - 7095.48 i
```

```
71467.6 - 7338.83 i
```

```
0.0581316
```

# References


[1] G.-B. Lee, C.-C. Chang, S.-B. Huang, R.-J. Yang, J. Micromechanics Microengineering 2006, 16, 1024.

[2] T. Sun, N. G. Green, S. Gawad, H. Morgan, IET Nanobiotechnol. 2007, 1, 69.

[3] T. Sun, S. Gawad, N. G. Green, H. Morgan, J. Phys. Appl. Phys. 2007, 40, 1.

[4] T. Sun, C. Bernabini, H. Morgan, Langmuir 2010, 26, 3821.

[5] H. Morgan, T. Sun, D. Holmes, S. Gawad, N. G. Green, J. Phys. Appl. Phys. 2007, 40, 61.

# Appendix C: MATLAB code

## Sparse impedance signals from LCR meter

This code served to analyze data from the particle-based experiments in elucidating the interplay between hydrodynamic focusing and impedance cytometry

### Data import

Read in raw timestamps *t*, impedance magnitudes *Z*, and phase values *d*

```
import = csvread(filename);
t = import(:,1);
z = import(:,2);
d = import(:,3);
```

### Signal background - Step 1

Remove obvious peaks from *Z* based on a threshold (of one standard deviation) in its second derivative, then extrapolate smoothed points inbetween as initial approximation of background signal

```
ddz = abs(vertcat(0,diff(diff(z)),0));
temptable = table(t,z,d,ddz,'VariableNames',{'t','z','d','ddz'});
temptable = temptable(temptable.ddz < std(ddz),:);
zbackground = interp1(temptable.t,temptable.z,t,'pchip');
dbackground = interp1(temptable.t,temptable.d,t,'pchip');
```

### Signal background - Step 2

Construct 9 Hz maximally flat low-pass filter and apply to the previously approximated background

```
Nb   = 8;   % Numerator Order
Na   = 8;   % Denominator Order
F3dB = 9;   % 3-dB Frequency
Fs   = 180; % Sampling Frequency
h = fdesign.lowpass('nb,na,f3db', Nb, Na, F3dB, Fs);
f = design(h, 'butter');
zbackground = filtfilt(f.sosMatrix,f.ScaleValues,zbackground);
dbackground = filtfilt(f.sosMatrix,f.ScaleValues,dbackground);
```

### Parameter calculation

Calculate impedance signal by subtracting the background from the raw data and also express as percentage value; use simple local peak finding algorithm for final data processing

```
zclean = z - zbackground;
dclean = d - dbackground;
zpercent = zclean./zbackground;
dpercent = dclean./dbackground;
[~,zpeak] = findpeaks(zclean);
[~,dpeak] = findpeaks(dclean);
```

### Output

```
output = struct(...
    't',t,...
    'raw',struct('z',z,'d',d),...
    'background',struct('z',zbackground,'d',dbackground),...
    'clean',struct('z',zclean,'d',dclean),...
    'percent',struct('z',zpercent,'d',dpercent),...
    'peaks',struct('z',zpeak,'d',dpeak)...
    );
```

## Near-saturation impedance signals from LCR meter

This code served to analyze data from the blood-based experiments in elucidating the interplay between osmotic lysis and impedance cytometry

### Data import

Read in raw timestamps *t*, impedance magnitudes *Z*, and phase values *d*

```
import = csvread(filename);
t = import(:,1);
z = import(:,2);
d = import(:,3);
```

### Signal background

Use image erosion algorithm to determine signal floor, and apply smoothing

```
zbackground = imerode(z', true(1, 10))';
dbackground = imerode(d', true(1, 10))';
zbackground = smooth(zbackground,50*1/length(zbackground),'moving');
dbackground = smooth(dbackground,50*1/length(dbackground),'moving');
```

### Parameter calculation

Calculate impedance signal by subtracting the background from the raw data and also express as percentage value; use simple local peak finding algorithm for final data processing

```
zclean = z - zbackground;
dclean = d - dbackground;
zpercent = zclean./zbackground;
dpercent = dclean./dbackground;
[~,zpeak] = findpeaks(zclean);
[~,dpeak] = findpeaks(dclean);
```

### Output parameters

```
output = struct(...
    't',t,...
    'raw',struct('z',z,'d',d),...
    'background',struct('z',zbackground,'d',dbackground),...
    'clean',struct('z',zclean,'d',dclean),...
    'percent',struct('z',zpercent,'d',dpercent),...
    'peaks',struct('z',zpeak,'d',dpeak)...
    );
```

### Histogram construction - Step 1

Numerical model-derived function to transform cell radius into impedance signal, where *p* is the set of appropriate model fit parameters for the given experimental conditions

```
syms x
f = symfun(p(2).*(abs(x-p(1))).^p(3)), [x]);
```

### Histogram construction - Step 2

Translate linear range of cell radii into range of impedance signals, and perform histogram binning on this non-linear impedance axis to yield linear-binned histogram on cell radius axis

```
xh = linspace(-0.005,12.005,1202)';
xh = double(f(xh));
h = histcounts(zpercent(zpeak),xh)';
```

## Sparse impedance signals from differential transimpedance/lock-in circuit

This code served to analyze impedance data from the experiments in the fully integrated microsystem

### Data import

Load LabView-generated Matlab file containing raw DAQ voltages at *low* and *high* frequencies

```
disp(filename);
load(filename);
```

Extract applied voltage signal levels and lock-in amplifier range settings for both frequencies from filename, and use them to convert raw DAQ voltages to μA current values (for theoretical 1V signal)

```
Vin = regexp(filename,'(?<= )[.\d]+-[.\d]+(?=V )','match','once');
Vin = strsplit(Vin,'-');
lowVin = str2double(Vin{1});
highVin = str2double(Vin{2});
Vrange = regexp(filename,'(?<= )[.\d]+-[.\d]+(?=mV )','match','once');
Vrange = strsplit(Vrange,'-');
lowrange = 0.001*str2double(Vrange{1});
highrange = 0.001*str2double(Vrange{2});
low=0.4*low*lowrange/lowVin;
high=1.6*high*highrange/highVin;
```

### Background signal

Construct 20 Hz low-pass filter

```
Fs = 125000; % Sampling Frequency
Fpass = 20; % Passband Frequency
Fstop = 30; % Stopband Frequency
Apass = 0.001; % Passband Ripple (dB)
Astop = 80; % Stopband Attenuation (dB)
match = 'passband'; % Band to match exactly
h  = fdesign.lowpass(Fpass, Fstop, Apass, Astop, Fs);
Hd = design(h, 'cheby2', 'MatchExactly', match);
```

Extract background signal by first applying a moving average algorithm, and then applying the above filter

```
lowbkg=movavg(3001,low);
lowbkg=filtfilt(Hd.sosMatrix,Hd.ScaleValues,lowbkg);
highbkg=movavg(3001,high);
highbkg=filtfilt(Hd.sosMatrix,Hd.ScaleValues,highbkg);
```

### Differential current signal

Remove background from original data, and downsample by a factor of 5 to reduce file size

```
low=low-lowbkg;
low=sample(5,low);
high=high-highbkg;
high=sample(5,high);
```

### Wavelet analysis

Loosely based off the methods described by Caselli et al. (2016) and Evander et al. (2013)

Determine 7 timescales for wavelet analysis based on the maximum linear flow velocity (~1.9x of the average) for the fixed channel geometry and the experimental *flowrate*

```
scales = ((50*20*125)/(1.9*flowrate*277778))/(4e-5) * [1,1.1,1.2,1.5,1.9,2.4,3];
slen = length(scales);
```

Calculate Continuous Wavelet Analysis with anti-symmetric wavelet, and determine the absolute squared coefficients

```
coefs=cwt(low,1.7230*scales/5,'gaus1');
coefs=abs(coefs.*coefs);
```

Apply cross-correlation with Gaussian peak function to the wavelet coefficient matrix to yield single peak per signal

```
llow=length(low);
xcoefs=zeros(llow,slen);
parfor i=1:slen
    disp(['Crosscorrelating Wavelet Scale ',num2str(i),' ...']);
    v=round(scales(i)/2);
    temp=xcorr(coefs(i,:)',gausswin(round(scales(i)),1));
    xcoefs(:,i)=temp(llow-v:end-v);
end
```

Find peaks in the cross-correlation matrix using Matlab's simple algorithm and apply a suitable threshold *thresh*

```
len = round(llow/(2*max(scales)));
pos = zeros(len,slen);
parfor i=1:slen
    disp(['Finding Peaks Scale ',num2str(i),' ...']);
    w=round(scales(i));
    [~,temp]=findpeaks(xcoefs(:,i),'MinPeakDistance',w,'MinPeakHeight',thresh);
    temp(length(temp)+1:len)=0;
    pos(:,i)=temp;
end
```

### Signal extraction

Employ the peak positions in the cross-correlation matrix to identify peaks in the current signal, and extract the relevant maxima and minima as well as the *e2o* norm defined by Caselli et al.

```
pos=unique(pos,'rows','stable');
len=length(pos);
array = zeros(slen,len,6);
for i=1:slen
    v=round(scales(i)/2);
    for j = 1:len
        x = pos(j,i);
        if x
            if (x+v)<llow+1 && (x-v)>0
                eplus=low(x:x+v);
                eminus=low(x-v:x);
                e2o=norm((eplus+eminus)/2)/norm((eplus-eminus)/2);
                [maglow1,indlow1]=max(low(x-v:x+v));
                [maglow2,indlow2]=min(low(x-v:x+v));
                maghigh2=max(high(x-v:x+v));
                maghigh3=min(high(x-v:x+v));
                loc=x-v+(indlow1+indlow2)/2;
                array(i,j,:)=[loc,maglow1,maglow2,maghigh2,maghigh3,e2o];
            end
        end
    end
end
```

### Peak matching

Eliminate duplicates form the multiple timescales employed in the analysis based on a window around each identified peak, and keep only the "best" values for each parameter stored

```
flatarray = zeros(len*5,6);
for i=1:slen
    flatarray(((i-1)*len)+1:i*len,:)=array(i,:,:);
end
array=unique(abs(flatarray),'rows');
i=size(array,1);
v=round(max(scales)/2);
tempoutput=[];
while i > 1
    condition=(array(:,1)>array(i,1)-v);
    line=cat(2,mean(array(condition,1))*4e-5,max(array(condition,2:5),[],1),min(a
rray(condition,6),[],1));
    tempoutput=cat(1,line,tempoutput);
    array(condition,:)=[];
```

```
    i=i-sum(condition);
end
```

### Output parameter calculation

Apply threshold of 0.5 for *e2o* norm to the data; for each event, output time index *ztime*, low-frequency signal *xsize*, and the ratio of high- to low-frequency signals *yopacity*

```
tempoutput = tempoutput(tempoutput(:,6)<0.5,:);
output.ztime = tempoutput(:,1);
output.xsize = tempoutput(:,2)+tempoutput(:,3);
output.yopacity = (tempoutput(:,4)+tempoutput(:,5))./output.xsize;
output.xsize = output.xsize./2;
```

### Custom functions

adapted from stackoverflow.com/questions/26981478

**`function y = movavg(w,x)`**

```
    w = 2*floor(w/2)+1;
    i = floor(w/2)+1;
    cs = cumsum(x)/w;
    y = zeros(numel(x),1);
    y(1:i)=cs(w);
    y(end-(i-2):end) = cs(end) - cs(end-w);
    y(i+1:end-(i-1))=cs(w+1:end)-cs(1:end-w);
```

**`function y = sample(w,x)`**

```
    w = 2*floor(w/2)+1;
    i = floor(w/2);
    cv = conv(x, ones(1, w), 'valid')/w;
    y = zeros(numel(x),1);
    y(1:i) = cv(1);
    y(end-(i-1):end) = cv(end);
    y(i+1:end-i) = cv;
    y = downsample(y,w);
```

*Published with MATLAB® R2014b*

# Bibliography


[1] C. D. Chin, V. Linder, and S. K. Sia. "Commercialization of microfluidic point-of-care diagnostic devices." *Lab on a Chip* 12 (2012), pp. 2118–2134.

[2] M. Schöning et al. "Amperometric PDMS/glass capillary electrophoresis-based biosensor microchip for catechol and dopamine detection." *Sensors and Actuators B: Chemical* 108 (2005), pp. 688–694.

[3] M. Yamaguchi et al. "Flow-injection-type biosensor system for salivary amylase activity." *Biosensors and Bioelectronics* 18 (2003), pp. 835–840.

[4] J. H. Kim, D. Diamond, and K.-T. Lau. "Development of non-invasive biochemical device for monitoring the lithium level from saliva for bipolar disorder patients." In: *Technical Digest, IEEE Sensors*. Limerick, Ireland, 2011, pp. 1744–1747.

[5] World Health Organization. *The global burden of disease: 2004 update*. 2008.

[6] M. Cloutier et al. "The Economic Burden of Schizophrenia in the United States in 2013." *The Journal of Clinical Psychiatry* 77 (2016), pp. 764–771.

[7] R. W. Buchanan et al. "The 2009 Schizophrenia PORT Psychopharmacological Treatment Recommendations and Summary Statements." *Schizophrenia Bulletin* 36 (2010), pp. 71–93.

[8] R. A. Carlstedt. *Handbook of Integrative Clinical Psychology, Psychiatry, and Behavioral Medicine: Perspectives, Practices, and Research*. New York: Springer Publishing Company, 2010.

[9] R. R. Conley et al. "Treatment-resistant schizophrenic patients respond to clozapine after olanzapine non-response." *Biological Psychiatry* 46 (1999), pp. 73–77.

[10] R. R. Conley et al. "Comparison of Clozapine Use in Maryland and in Victoria, Australia." *Psychiatric Services* 56 (2005), pp. 320–323.

[11] D. L. Kelly et al. "Blood Draw Barriers for Treatment with Clozapine and Development of Point-of-Care Monitoring Device." *Clinical Schizophrenia & Related Psychoses* (2015), in press.

[12] Novartis. *CLOZARIL Prescribing Information.* 2015.

[13] A. Stark and J. Scott. "A review of the use of clozapine levels to guide treatment and determine cause of death." *Australian and New Zealand Journal of Psychiatry* 46 (2012), pp. 816–825.

[14] C. Hiemke et al. "AGNP consensus guidelines for therapeutic drug monitoring in psychiatry: update 2011." *Pharmacopsychiatry* 44 (2011), pp. 195–235.

[15] S. X. Sun et al. "Review and analysis of hospitalization costs associated with antipsychotic nonadherence in the treatment of schizophrenia in the United States." *Current Medical Research and Opinion* 23 (2007), pp. 2305–2312.

[16] E. Spina and J. De Leon. "Metabolic Drug Interactions with Newer Antipsychotics: A Comparative Review." *Basic & Clinical Pharmacology & Toxicology* 100 (2007), pp. 4–22.

[17] E. Olsson et al. "Genetic and Clinical Factors Affecting Plasma Clozapine Concentration." *The Primary Care Companion for CNS Disorders* 17 (2015).

[18] R. Flanagan, B. Yusufi, and T. Barnes. "Comparability of whole-blood and plasma clozapine and norclozapine concentrations." *British Journal of Clinical Pharmacology* 56 (2003), pp. 135–138.

[19] D. Zhou and F. Li. "Protein binding study of clozapine by capillary electrophoresis in the frontal analysis mode." *Journal of Pharmaceutical and Biomedical Analysis* 35 (2004), pp. 879–885.

[20] B. L. Roth. *Psychoactive Drug Screening Program Ki database.*

[21] S. Miyamoto et al. “Treatments for schizophrenia: a critical review of pharmacology and mechanisms of action of antipsychotic drugs.” *Molecular Psychiatry* 10 (2004), pp. 79–104.

[22] M. Pirmohamed and K. Park. “Mechanism of clozapine-induced agranulocytosis : current status of research and implications for drug development.” *CNS drugs* 7 (1997), pp. 139–158.

[23] R. Uřinovská et al. “Liquid chromatography–tandem mass spectrometry method for determination of five antidepressants and four atypical antipsychotics and their main metabolites in human serum.” *Journal of Chromatography B* 907 (2012), pp. 101–107.

[24] G. Schaber et al. “Pharmacokinetics of clozapine and its metabolites in psychiatric patients: plasma protein binding and renal clearance.” *British Journal of Clinical Pharmacology* 46 (1998), pp. 453–459.

[25] H. Yin et al. “Microfluidic Chip for Peptide Analysis with an Integrated HPLC Column, Sample Enrichment Column, and Nanoelectrospray Tip.” *Analytical Chemistry* 77 (2005), pp. 527–533.

[26] F. T. G. van den Brink et al. “Mass Spectrometric Detection of Short-Lived Drug Metabolites Generated in an Electrochemical Microfluidic Chip.” *Analytical Chemistry* 87 (2014), pp. 1527–1535.

[27] C. Haring et al. “Clozapine plasma levels determined by high-performance liquid chromatography with ultraviolet detection.” *Journal of Chromatography B: Biomedical Sciences and Applications* 428 (1988), pp. 160–166.

[28] C. Humpel, C. Haring, and A. Saria. “Rapid and sensitive determination of clozapine in human plasma using high-performance liquid chromatography and amperometric detection.” *Journal of Chromatography B: Biomedical Sciences and Applications* 491 (1989), pp. 235–239.

[29] R. Waschgler et al. "Simultaneous quantification of citalopram, clozapine, fluoxetine, norfluoxetine, maprotiline, desmethylmaprotiline and trazodone in human serum by HPLC analysis." *International Journal of Clinical Pharmacology and Therapeutics* 40 (2002), pp. 554–559.

[30] J.-M. Kauffmann, G. J. Patriarche, and G. D. Christian. "Electrochemical Oxidation of Derivatives of Dibenzodiazepin. Dibenzothiazepin and Dibenzoxazepin." *Analytical Letters* 12 (1979), pp. 1217–1234.

[31] S. M. van Leeuwen et al. "Prediction of clozapine metabolism by on-line electrochemistry/liquid chromatography/mass spectrometry." *Analytical and Bioanalytical Chemistry* 382 (2005), pp. 742–750.

[32] V. Pucci, M. Raggi, and E. Kenndler. "Separation of antipsychotic drugs (clozapine, loxapine) and their metabolites by capillary zone electrophoresis." *Journal of Chromatography A* 853 (1999), pp. 461–468.

[33] S. Hillaert, L. Snoeck, and W. Van den Bossche. "Optimization and validation of a capillary zone electrophoretic method for the simultaneous analysis of four atypical antipsychotics." *Journal of Chromatography A* 1033 (2004), pp. 357–362.

[34] W. Jin, Q. Xu, and W. Li. "Determination of clozapine by capillary zone electrophoresis following end-column amperometric detection with simplified capillary/electrode alignment." *Electrophoresis* 21 (2000), pp. 1415–1420.

[35] M. A. Raggi et al. "Rapid capillary electrophoretic method for the determination of clozapine and desmethylclozapine in human plasma." *Journal of Chromatography A* 916 (2001), pp. 289–296.

[36] J. Sekula et al. "Coated Wire Potentiometric Detection for Capillary Electrophoresis Studied Using Organic Amines, Drugs, and Biogenic Amines." *Analytical Chemistry* 78 (2006), pp. 3772–3779.

[37] D. A. Flockhart. *Drug Interactions: Cytochrome P450 Drug Interaction Table*. 2007.

[38] C. Paternolli et al. “Recombinant Cytochrome P450 Immobilization for Biosensor Applications.” *Langmuir* 20 (2004), pp. 11706–11712.

[39] R. Bashir. “BioMEMS: state-of-the-art in detection, opportunities and prospects.” *Advanced Drug Delivery Reviews* 56 (2004), pp. 1565–1586.

[40] L. Hernández, E. González, and P. Hernández. “Determination of clozapine by adsorptive anodic voltammetry using glassy carbon and modified carbon paste electrodes.” *Analyst* 113 (1988), pp. 1715–1718.

[41] E. Hammam, A. Tawfik, and M. Ghoneim. “Adsorptive stripping voltammetric quantification of the antipsychotic drug clozapine in bulk form, pharmaceutical formulation and human serum at a mercury electrode.” *Journal of Pharmaceutical and Biomedical Analysis* 36 (2004), pp. 149–156.

[42] K. Farhadi and A. Karimpour. “Electrochemical Behavior and Determination of Clozapine on a Glassy Carbon Electrode Modified by Electrochemical Oxidation.” *Analytical Sciences* 23 (2007), pp. 479–483.

[43] S. Shahrokhian, Z. Kamalzadeh, and A. Hamzehloei. “Electrochemical determination of Clozapine on MWCNTs/New Coccine doped PPY modified GCE: An experimental design approach.” *Bioelectrochemistry* 90 (2013), pp. 36–43.

[44] S. Murrin. *Medicare Payments for Clinical Diagnostic Laboratory Tests in 2015: Year 2 of Baseline Data*. Tech. rep. OEI-09-16-00040. Department of Health and Human Services, 2016.

[45] K. Kottke-Marchant and B. Davis. *Laboratory Hematology Practice*. Chichester, UK: Wiley-Blackwell, 2012.

[46] B. Medical. “Blausen Medical Image Gallery.” *WikiJournal of Medicine* 1 (2014).

[47] H. Andersson and A. van den Berg. “Microfluidic devices for cellomics: a review.” *Sensors and Actuators B: Chemical* 92 (2003), pp. 315–325.

[48] H. Zhang et al. “Methods for counting particles in microfluidic applications.” *Microfluidics and Nanofluidics* 7 (2009), pp. 739–749.

[49] M. E. Piyasena and S. W. Graves. “The intersection of flow cytometry with microfluidics and microfabrication.” *Lab on a Chip* 14 (2014), pp. 1044–1059.

[50] W. Jung et al. “Point-of-care testing (POCT) diagnostic systems using microfluidic lab-on-a-chip technologies.” *Microelectronic Engineering* 132 (2015), pp. 46–57.

[51] R. W. DeBlois and C. P. Bean. “Counting and Sizing of Submicron Particles by the Resistive Pulse Technique.” *Review of Scientific Instruments* 41 (1970), pp. 909–916.

[52] D. A. Ateya et al. “The good, the bad, and the tiny: a review of microflow cytometry.” *Analytical and Bioanalytical Chemistry* 391 (2008), pp. 1485–1498.

[53] U. D. Larsen, G. Blankenstein, and J. Branebjerg. “Microchip Coulter particle counter.” In: *Technical Digest, International Conference on Miniaturized Systems for Chemistry and Life Sciences (μTAS)*. Chicago, Illinois, 1997, pp. 1319–1322.

[54] S. Gawad, L. Schild, and P. Renaud. “Micromachined impedance spectroscopy flow cytometer for cell analysis and particle sizing.” *Lab on a Chip* 1 (2001), pp. 76–82.

[55] D. Holmes et al. “Leukocyte analysis and differentiation using high speed microfluidic single cell impedance cytometry.” *Lab on a Chip* 9 (2009), pp. 2881–2889.

[56] X. Han et al. “Microfluidic Lysis of Human Blood for Leukocyte Analysis Using Single Cell Impedance Cytometry.” *Analytical Chemistry* 84 (2012), pp. 1070–1075.

[57] D. Holmes et al. “Bead-based immunoassays using a micro-chip flow cytometer.” *Lab on a Chip* 7 (2007), p. 1048.

[58] K. C. Cheung et al. “Microfluidic impedance-based flow cytometry.” *Cytometry Part A* 77A (2010), pp. 648–666.

[59] T. Sun and H. Morgan. “Single-cell microfluidic impedance cytometry: a review.” *Microfluidics and Nanofluidics* 8 (2010), pp. 423–443.

[60] Y. Xu et al. "A review of impedance measurements of whole cells." *Biosensors and Bioelectronics* 77 (2016), pp. 824–836.

[61] A. Reece et al. "Microfluidic techniques for high throughput single cell analysis." *Current Opinion in Biotechnology* 40 (2016), pp. 90–96.

[62] L. Kestens and F. Mandy. "Thirty-five years of CD4 T-Cell counting in HIV infection: From flow cytometry in the lab to point-of-care testing in the field." *Cytometry Part B: Clinical Cytometry* (2016), in press.

[63] M. A. Mansor and M. R. Ahmad. "Single Cell Electrical Characterization Techniques." *International Journal of Molecular Sciences* 16 (2015), pp. 12686–12712.

[64] J. Chen et al. "Microfluidic Impedance Flow Cytometry Enabling High-Throughput Single-Cell Electrical Property Characterization." *International Journal of Molecular Sciences* 16 (2015), pp. 9804–9830.

[65] D. Vercruysse et al. "Three-part differential of unlabeled leukocytes with a compact lens-free imaging flow cytometer." *Lab on a Chip* 15 (2015), pp. 1123–1132.

[66] M. Baday et al. "Integrating Cell Phone Imaging with Magnetic Levitation (i-LEV) for Label-Free Blood Analysis at the Point-of-Living." *Small* 12 (2016), pp. 1222–1229.

[67] Y. Zhang et al. "Trapping cells in paper for white blood cell count." *Biosensors and Bioelectronics* 69 (2015), pp. 121–127.

[68] L. Kong, J. Tang, and M. Cui. "Multicolor multiphoton in vivo imaging flow cytometry." *Optics Express* 24 (2016), pp. 6126–6135.

[69] *Chempaq XBC eXpress Blood Counter manufactured by Chempaq A/S: An instrument for B—Haemoglobin, B—Leukocytes and three-part differential count.* Tech. rep. SKUP/2006/47. SKUP—Scandinavian Evaluation of Laboratory Equipment for Primary Health Care, 2006.

[70] S. Lindberg et al. "A Novel Technology for 5-Part Differentiation of Leukocytes Point-of-Care:" *Point of Care: The Journal of Near-Patient Testing & Technology* 13 (2014), pp. 27–30.

[71] *HemoCue WBC: A system for measurement of the concentration of leukocytes in blood manufactured by HemoCue AB, Sweden.* Tech. rep. SKUP/2010/73. SKUP—Scandinavian Evaluation of Laboratory Equipment for Primary Health Care, 2010.

[72] J. Nielsen et al. "Hematological clozapine monitoring with a point-of-care device: A randomized cross-over trial." *European Neuropsychopharmacology* 22 (2012), pp. 401–405.

[73] H. N. Bui et al. "Evaluation of the performance of a point-of-care method for total and differential white blood cell count in clozapine users." *International Journal of Laboratory Hematology* 38 (2016), pp. 703–709.

[74] E. F. D. Canetti et al. "Comparison of capillary and venous blood in the analysis of concentration and function of leucocyte sub-populations." *European Journal of Applied Physiology* 116 (2016), pp. 1583–1593.

[75] C. W. Shields et al. "Translating microfluidics: Cell separation technologies and their barriers to commercialization." *Cytometry Part B: Clinical Cytometry* (2016), in press.

[76] M. Toner and D. Irimia. "Blood-on-a-Chip." *Annual Review of Biomedical Engineering* 7 (2005), pp. 77–103.

[77] C. van Berkel et al. "Integrated systems for rapid point of care (PoC) blood cell analysis." *Lab on a Chip* 11 (2011), pp. 1249–1255.

[78] M. Kersaudy-Kerhoas and E. Sollier. "Micro-scale blood plasma separation: from acoustophoresis to egg-beaters." *Lab on a Chip* 13 (2013), pp. 3323–3346.

[79] R. Fan et al. "Integrated barcode chips for rapid, multiplexed analysis of proteins in microliter quantities of blood." *Nature Biotechnology* 26 (2008), pp. 1373–1378.

[80] W. Huang et al. “Concurrent Detection of Cellular and Molecular Cancer Markers Using an Immunomagnetic Flow System.” *Analytical Chemistry* 87 (2015), pp. 10205–10212.

[81] W. Huang et al. “Separation and dual detection of prostate cancer cells and protein biomarkers using a microchip device.” *Lab on a Chip* (2016), in press.

[82] V. Patrulea et al. “Chitosan as a starting material for wound healing applications.” *European Journal of Pharmaceutics and Biopharmaceutics*. Polymers for Drug Delivery Systems 97, Part B (2015), pp. 417–426.

[83] Y. Yang et al. “Advances in self-assembled chitosan nanomaterials for drug delivery.” *Biotechnology Advances* 32 (2014), pp. 1301–1316.

[84] S. T. Koev et al. “Chitosan: an integrative biomaterial for lab-on-a-chip devices.” *Lab on a Chip* 10 (2010), pp. 3026–3042.

[85] E. Kim et al. “Fusing Sensor Paradigms to Acquire Chemical Information: An Integrative Role for Smart Biopolymeric Hydrogels.” *Advanced Healthcare Materials* 5 (2016), pp. 2595–2616.

[86] E. Kim et al. “Biomimetic Approach to Confer Redox Activity to Thin Chitosan Films.” *Advanced Functional Materials* 20 (2010), pp. 2683–2694.

[87] W. M. Clark. *Oxidation Reduction Potentials of Organic Systems*. Baltimore: Williams & Wilkins, 1960.

[88] A. J. Bard and L. R. Faulkner. *Electrochemical Methods: Fundamentals and Applications*. New York, NY, US: John Wiley & Sons, 2000.

[89] E. Kim et al. “Reverse Engineering To Suggest Biologically Relevant Redox Activities of Phenolic Materials.” *ACS Chemical Biology* 8 (2013), pp. 716–724.

[90] T. E. Winkler et al. “Electrochemical Study of the Catechol-Modified Chitosan System for Clozapine Treatment Monitoring.” *Langmuir* 30 (2014), pp. 14686–14693.

[91] H. Ben-Yoav et al. “Redox cycling-based amplifying electrochemical sensor for in situ clozapine antipsychotic treatment monitoring.” *Electrochimica Acta* 130 (2014), pp. 497–503.

[92] M. D. Borysiak, M. J. Thompson, and J. D. Posner. “Translating diagnostic assays from the laboratory to the clinic: analytical and clinical metrics for device development and evaluation.” *Lab on a Chip* 16 (2016), pp. 1293–1313.

[93] T. E. Winkler et al. “Molecular Processes in an Electrochemical Clozapine Sensor.” *Biointerphases* (2017), submitted.

[94] http://www.chemicalize.com/. *ChemAxon Chemicalize*. 2016.

[95] S. C. Petrovic and R. H. Hammericksen. “Determination of Ferrocene Solubility by Normalized Chronoamperometry: An Evaluation of Experimental Constraints.” *Electroanalysis* 14 (2002), pp. 599–604.

[96] D. Li, S. Fu, and C. A. Lucy. “Prediction of Electrophoretic Mobilities. 3. Effect of Ionic Strength in Capillary Zone Electrophoresis.” *Analytical Chemistry* 71 (1999), pp. 687–699.

[97] R. Plasson and H. Cottet. “Determination of Homopolypeptide Conformational Changes by the Modeling of Electrophoretic Mobilities.” *Analytical Chemistry* 77 (2005), pp. 6047–6054.

[98] M. H. Mashhadizadeh and E. Afshar. “Electrochemical investigation of clozapine at TiO2 nanoparticles modified carbon paste electrode and simultaneous adsorptive voltammetric determination of two antipsychotic drugs.” *Electrochimica Acta* 87 (2013), pp. 816–823.

[99] E. Kim et al. "Programmable "Semismart" Sensor: Relevance to Monitoring Antipsychotics." *Advanced Functional Materials* 25 (2015), pp. 2156–2165.

[100] S. E. Chocron et al. "Multidimensional Mapping Method Using an Arrayed Sensing System for Cross-Reactivity Screening." *PLoS ONE* 10 (2015), e0116310.

[101] M. G. Simic and S. V. Jovanovic. "Antioxidation mechanisms of uric acid." *Journal of the American Chemical Society* 111 (1989), pp. 5778–5782.

[102] G. E. Banis et al. "The Binding Effect of Proteins on Medications and Its Impact on Electrochemical Sensing: Antipsychotic Clozapine as a Case Study." *PLoS ONE* (2017), submitted.

[103] D. A. Smith, L. Di, and E. H. Kerns. "The effect of plasma protein binding on in vivo efficacy: misconceptions in drug discovery." *Nature Reviews Drug Discovery* 9 (2010), pp. 929–939.

[104] L. D. Burke and P. F. Nugent. "The electrochemistry of gold: II the electrocatalytic behaviour of the metal in aqueous media." *Gold Bulletin* 31 (1998), pp. 39–50.

[105] B. Ilic et al. "Preparation and characterization of platinum black electrodes." *Journal of Materials Science* 35 (2000), pp. 3447–3457.

[106] C. Nunes Kirchner et al. "Evaluation of Thin Film Titanium Nitride Electrodes for Electroanalytical Applications." *Electroanalysis* 19 (2007), pp. 1023–1031.

[107] A. M. Bond and F. Scholz. "A Survey of Electrodes used for Voltammetric Analysis." *Zeitschrift für Chemie* 30 (1990), pp. 117–129.

[108] A. M. Feltham and M. Spiro. "Platinized platinum electrodes." *Chemical Reviews* 71 (1971), pp. 177–193.

[109] R. Martinez-Duarte. "SU-8 Photolithography as a Toolbox for Carbon MEMS." *Micromachines* 5 (2014), pp. 766–782.

[110] T. E. Winkler et al. "The Interplay of Electrode- and Bio-Materials in a Redox Cycling-based Clozapine Sensor." *Electrochemistry Communications* (2017), submitted.

[111] W. M. Haynes. *CRC Handbook of Chemistry and Physics, 96th Edition*. Boca Raton, FL, US: CRC Press, 2015.

[112] B. Avasarala and P. Haldar. "Electrochemical oxidation behavior of titanium nitride based electrocatalysts under PEM fuel cell conditions." *Electrochimica Acta* 55 (2010), pp. 9024–9034.

[113] S. Park, H. Boo, and T. D. Chung. "Electrochemical non-enzymatic glucose sensors." *Analytica Chimica Acta*. Young Analytical Faculty in Asia 556 (2006), pp. 46–57.

[114] K. E. Toghill and R. G. Compton. "Electrochemical non-enzymatic glucose sensors: a perspective and an evaluation." *International Journal of Electrochemical Science* 5 (2010), pp. 1246–1301.

[115] N. Priyantha and S. Malavipathirana. "Effect of Chloride Ions on the Electrochemical Behaviour of Platinum Surfaces." *Journal of the National Science Council of Sri Lanka* 24 (1996), pp. 237–246.

[116] J. S. Mayell and S. H. Longer. "A Study of Surface Oxides on Platinum Electrodes." *Journal of The Electrochemical Society* 111 (1964), pp. 438–446.

[117] C. B. Jacobs, M. J. Peairs, and B. J. Venton. "Review: Carbon nanotube based electrochemical sensors for biomolecules." *Analytica Chimica Acta* 662 (2010), pp. 105–127.

[118] Y. Shao et al. "Graphene Based Electrochemical Sensors and Biosensors: A Review." *Electroanalysis* 22 (2010), pp. 1027–1036.

[119] C. Zhu et al. "Electrochemical Sensors and Biosensors Based on Nanomaterials and Nanostructures." *Analytical Chemistry* 87 (2015), pp. 230–249.

[120] M. Kang et al. "Electrodeposited Graphene-Chitosan Composite Film for Therapeutic Drug Monitoring." *Biosensors and Bioelectronics* (2017), submitted.

[121] E. Spina et al. "Relationship between plasma concentrations of clozapine and norclozapine and therapeutic response in patients with schizophrenia resistant to conventional neuroleptics." *Psychopharmacology* 148 (2000), pp. 83–89.

[122] R. Rodriguez-Trujillo et al. "Low cost micro-Coulter counter with hydrodynamic focusing." *Microfluidics and Nanofluidics* 3 (2007), pp. 171–176.

[123] C. Bernabini, D. Holmes, and H. Morgan. "Micro-impedance cytometry for detection and analysis of micron-sized particles and bacteria." *Lab on a Chip* 11 (2011), pp. 407–412.

[124] M. Evander et al. "Microfluidic impedance cytometer for platelet analysis." *Lab on a Chip* 13 (2013), pp. 722–729.

[125] J. H. Nieuwenhuis et al. "Integrated Coulter counter based on 2-dimensional liquid aperture control." *Sensors and Actuators B: Chemical* 102 (2004), pp. 44–50.

[126] J. P. Golden et al. "Hydrodynamic focusing – a versatile tool." *Analytical and Bioanalytical Chemistry* 402 (2012), pp. 325–335.

[127] R. Rodriguez-Trujillo et al. "High-speed particle detection in a micro-Coulter counter with two-dimensional adjustable aperture." *Biosensors and Bioelectronics* 24 (2008), pp. 290–296.

[128] N. Watkins et al. "A robust electrical microcytometer with 3-dimensional hydrofocusing." *Lab on a Chip* 9 (2009), pp. 3177–3184.

[129] X. Xuan, J. Zhu, and C. Church. "Particle focusing in microfluidic devices." *Microfluidics and Nanofluidics* 9 (2010), pp. 1–16.

[130] T. E. Winkler, H. Ben-Yoav, and R. Ghodssi. "Hydrodynamic focusing for microfluidic impedance cytometry: a system integration study." *Microfluidics and Nanofluidics* 20 (2016), p. 134.

[131] C. Kunstmann-Olsen, J. D. Hoyland, and H.-G. Rubahn. "Influence of geometry on hydrodynamic focusing and long-range fluid behavior in PDMS microfluidic chips." *Microfluidics and Nanofluidics* 12 (2012), pp. 795–803.

[132] M. Nasir et al. "Parameters affecting the shape of a hydrodynamically focused stream." *Microfluidics and Nanofluidics* 11 (2011), pp. 119–128.

[133] T. Sun et al. "Analytical electric field and sensitivity analysis for two microfluidic impedance cytometer designs." *IET Nanobiotechnology* 1 (2007), pp. 69–79.

[134] G.-B. Lee et al. "The hydrodynamic focusing effect inside rectangular microchannels." *Journal of Micromechanics and Microengineering* 16 (2006), pp. 1024–1032.

[135] D. R. Lide and H. V. Kehiaian. *CRC Handbook of Thermophysical and Thermochemical Data*. Boca Raton, FL, US: CRC Press, 1994.

[136] H. C. Berg. *Random Walks in Biology*. Princeton, NJ, US: Princeton University Press, 1993.

[137] S. Gawad et al. "Dielectric spectroscopy in a micromachined flow cytometer: theoretical and practical considerations." *Lab on a Chip* 4 (2004), pp. 241–251.

[138] T. Sun, C. Bernabini, and H. Morgan. "Single-Colloidal Particle Impedance Spectroscopy: Complete Equivalent Circuit Analysis of Polyelectrolyte Microcapsules." *Langmuir* 26 (2010), pp. 3821–3828.

[139] T. Sun et al. "Dielectric spectroscopy of single cells: time domain analysis using Maxwell's mixture equation." *Journal of Physics D: Applied Physics* 40 (2007), pp. 1–8.

[140] H. Morgan et al. "Single cell dielectric spectroscopy." *Journal of Physics D: Applied Physics* 40 (2007), pp. 61–70.

[141] T. Sun, N. G. Green, and H. Morgan. "Analytical and Numerical Modeling Methods for Impedance Analysis of Single Cells on-Chip." *Nano* 3 (2008), pp. 55–63.

[142] E. Pitts and B. E. Tabor. "Concentration dependence of electrolyte conductance. Part 2.—Comparison of experimental data with the Fuoss-Onsager and Pitts treatments." *Transactions of the Faraday Society* 66 (1970), pp. 693–707.

[143] A. M. Johnson et al. "Design and Testing of an Impedance-Based Sensor for Monitoring Drug Delivery." *Journal of The Electrochemical Society* 152 (2005), H6–H11.

[144] S. Bhattacharya et al. "Studies on surface wettability of poly(dimethyl) siloxane (PDMS) and glass under oxygen-plasma treatment and correlation with bond strength." *Journal of Microelectromechanical Systems* 14 (2005), pp. 590–597.

[145] M. Nasir et al. "Effect of diffusion on impedance measurements in a hydrodynamic flow focusing sensor." *Lab on a Chip* 10 (2010), pp. 2787–2795.

[146] H. M. Shapiro. *Practical Flow Cytometry*. Hoboken, NJ, US: John Wiley & Sons, 2003.

[147] H. P. Ting-Beall, D. Needham, and R. M. Hochmuth. "Volume and osmotic properties of human neutrophils." *Blood* 81 (1993), pp. 2774–2780.

[148] P. Sethu et al. "Continuous Flow Microfluidic Device for Rapid Erythrocyte Lysis." *Analytical Chemistry* 76 (2004), pp. 6247–6253.

[149] Y. Zhan et al. "Characterizing osmotic lysis kinetics under microfluidic hydrodynamic focusing for erythrocyte fragility studies." *Lab on a Chip* 12 (2012), pp. 5063–5068.

[150] P. Sethu et al. “Microfluidic Isolation of Leukocytes from Whole Blood for Phenotype and Gene Expression Analysis.” *Analytical Chemistry* 78 (2006), pp. 5453–5461.

[151] T. E. Winkler et al. “Osmotic Erythrocyte Lysis for Chemical- and Label-free Impedance Cytometry.” In: *Technical Digest, International Conference on Solid-State Sensors, Actuators and Microsystems (Transducers)*. Anchorage, Alaska, 2015, pp. 351–354.

[152] J. H. Barbee and G. R. Cokelet. “The Fahraeus effect.” *Microvascular Research* 3 (1971), pp. 6–16.

[153] D. A. Fedosov and G. Gompper. “White blood cell margination in microcirculation.” *Soft Matter* 10 (2014), pp. 2961–2970.

[154] S. S. Shevkoplyas et al. “Biomimetic Autoseparation of Leukocytes from Whole Blood in a Microfluidic Device.” *Analytical Chemistry* 77 (2005), pp. 933–937.

[155] S. Yang, A. Ündar, and J. D. Zahn. “A microfluidic device for continuous, real time blood plasma separation.” *Lab on a Chip* 6 (2006), pp. 871–880.

[156] F. Zang. “Integration of Virus-like Particle Macromolecular Bioreceptors in Electrochemical Biosensors.” PhD thesis. University of Maryland, College Park, 2016.

[157] J. N. Culver et al. “Plant virus directed fabrication of nanoscale materials and devices.” *Virology*. 60th Anniversary Issue 479–480 (2015), pp. 200–212.

[158] F. Zang et al. “Real-time monitoring of macromolecular biosensing probe self-assembly and on-chip ELISA using impedimetric microsensors.” *Biosensors and Bioelectronics* 81 (2016), pp. 401–407.

[159] T. E. Winkler et al. “Portable Immunoassay for Label-Free Antibody Detection in Whole Blood.” In: *Technical Digest, International Conference on Miniaturized Systems for Chemistry and Life Sciences (μTAS)*. Dublin, Ireland, 2016, pp. 661–662.

[160] Analog Devices. *AD5933 Impedance Converter Network Analyzer*. 2005.

[161] E. W. Salzman et al. "Effect of Heparin and Heparin Fractions on Platelet Aggregation." *The Journal of Clinical Investigation* 65 (1980), pp. 64–73.

[162] A. D. Michelson. "Antiplatelet therapies for the treatment of cardiovascular disease." *Nature Reviews Drug Discovery* 9 (2010), pp. 154–169.

[163] D. Bodas and C. Khan-Malek. "Hydrophilization and hydrophobic recovery of PDMS by oxygen plasma and chemical treatment—An SEM investigation." *Sensors and Actuators B: Chemical* 123 (2007), pp. 368–373.

[164] K. Boxshall et al. "Simple surface treatments to modify protein adsorption and cell attachment properties within a poly(dimethylsiloxane) micro-bioreactor." *Surface and Interface Analysis* 38 (2006), pp. 198–201.

[165] F. Caselli and P. Bisegna. "A Simple and Robust Event-Detection Algorithm for Single-Cell Impedance Cytometry." *IEEE Transactions on Biomedical Engineering* 63 (2016), pp. 415–422.

[166] A. Rottigni. "Electronical instrumentation for impedance measurement on biosamples." PhD thesis. Politecnico di Milano, 2012.

[167] J.-C. Chien et al. "A 6.5/17.5-GHz dual-channel interferometer-based capacitive Sensor in 65-nm CMOS for high-speed flow cytometry." In: *Proceedings of the IEEE MTT-S International Microwave Symposium (IMS)*. Tampa, Florida, 2014.

[168] A. Rottigni et al. "Handheld 2-channel impedimetric cell counting system with embedded real-time processing." In: *Proceedings of SPIE Microtechnologies*. Vol. 8068. Prague, Czech Republic, 2011.

[169] N. Talukder et al. "High sensitivity handheld analog readout circuit for microfluidic based electrical impedance sensing." In: *Proceedings of the IEEE Signal Processing in Medicine and Biology Symposium (SPMB)*. Philadelphia, Pennsylvania, 2015, pp. 1–6.

[170] Analog Devices. *ADuCM350 Impedance Converter and Potentiostat*. 2014.

[171] Z. Zhang et al. "Polybetaine modification of PDMS microfluidic devices to resist thrombus formation in whole blood." *Lab on a Chip* 13 (2013), pp. 1963–1968.

[172] S. Thorslund et al. "Functionality and stability of heparin immobilized onto poly(dimethylsiloxane)." *Colloids and Surfaces B: Biointerfaces* 45 (2005), pp. 76–81.

[173] M. Boyd-Moss et al. "Self-contained microfluidic systems: a review." *Lab on a Chip* 16 (2016), pp. 3177–3192.

[174] D. J. Laser and J. G. Santiago. "A review of micropumps." *Journal of Micromechanics and Microengineering* 14 (2004), R35–R64.

[175] C. K. Fredrickson and Z. H. Fan. "Macro-to-micro interfaces for microfluidic devices." *Lab on a Chip* 4 (2004), pp. 526–533.